A COMPUTATIONAL EVALUATION OF FLOW THROUGH POROUS MEDIA

Dimpho Millicent Molale

Thesis presented in partial fulfilment of the requirements for the
degree of Master of Science in Applied Mathematics at the
University of Stellenbosch.

Supervisor: Dr. GJF Smit

December 2007

Declaration

I, the undersigned, hereby declare that the work contained in this thesis is my own original work and that I have not previously in its entirety or in part submitted it at any university for a degree.

Signature: _____   Date: _____

Abstract

The understanding and quantitative description of fluid flow through porous media, is a science which has been going on for many years and investigated in a variety of disciplines. Studies in this field have primarily been based on models, which can either be described as empirical or theoretical. Part of the current study is to understand fluid flow in porous media through studying three recent theoretical pore-scale models based on the concept of a Representative Unit Cell (RUC), to represent a porous medium. Amongst other assumptions, these models assumed plane Poiseuille flow throughout each pore section of a rectangular RUC. The main objective of this study is to numerically verify this assumption using Computational Fluid Dynamics (CFD) software, FLUENT version 6.2.16.

Attention is also paid to comparison between these models with the experimental data, obtained during the model tests of airflow through a timber stack end, undertaken in a wind tunnel. The laminar and intermediate airflow through a timber stack end is simulated using the commercial software FLUENT, and the results are validated against the theoretical pore-scale models and experimental data. Two turbulence models which are, the Standard $k - \epsilon$ and Reynolds-Stress models are used in these computations, the aim being to determine how well they are able to reproduce the experimental data. The numerical results are in good agreement with one of the theoretical models presented and the experimental data.

Abstract

Die verstaan en kwantitiewe beskrywing van die vloei van vloeistowwe deur poreuse media, asook die oplossing en daarstel van die modelle wat die vloei beskryf is al vir verskeie jare aan die gang en word in verskeie disiplines ondersoek. Studies in hierdie veld word hoofsaaklik gebaseer op modelle wat as empiries of teoreties beskryf kan word. Hierdie studie poog ten dele om die vloei van vloeistowwe deur poreuse media deur middel van drie onlangse skaalmodelle, wat gebaseer is op die Verteenwoordigende Eenheid Sel (RUC), te verstaan. Onder andere word daar in hierdie modelle die aanname gemaak dat die Poiesuille vloei deur elke gedeelte van die reghoekige RUC beweeg. Die hoofoogmerk van hierdie studie is om hierdie aanname numeries te verifeer deur van Numeriese Vloeidinamika sagteware, FLUENT 6.2.16 gebruik.

Aandag word ook geskenk aan die vergelyking van hierdie modelle met eksperimentele data, wat tydens die toetsing van die lugvloei deur hout in 'n lugtonnel verkry is. Die laminre- en oorgangslugvloei deur die hout word met gebruik van die kommersile sagteware FLUENT gesimuleer en die resultate word geverifeer deur om dit te vergelyk met die teoreiese skaalmodelle en eksperimentele data. Twee turbulensiemodelle, die Standard $k - \epsilon$ en die Reynolds-Spanningsmodelle, word in hierdie simulasies gebruik. Die doel is om vas te stel hoe goed die modelle die eksperimentele data kan reproduseer. Die numeriese resultate stem goed ooreen met die teoretiese modelle en met die eksperimentele dat.

Acknowledgements

Dedication

To my late mother, Matshidiso, and to my lovely daughter Thuto who is very special to me.

Contents

List of Figures

List of Tables

List of Symbols

Roman symbol	Dimensions	Definition
$A_\parallel$, $A_\perp$	[m^2]	Stream-wise and transverse cross sectional pore area
C_D	[-]	Two-dimensional drag coefficient
C_f	[-]	Skin friction coefficient
D_H	[m]	Channel hydraulic diameter
d	[m]	Microscopic characteristic length
d_c	[m]	Pore width
d_s	[m]	Solid width
dp/dx	[Pa/m]	Stream-wise gradient of fluid pressure
F	[m^{-2}]	Friction factor for porous media
f	[-]	Fanning friction factor
f_{app}	[-]	Apparent friction factor
$\underline{g}$	[m/s^2]	Gravitational acceleration
H, a, b	[m]	Distance between parallel plates
H_s	[mm]	Stack height
K	[-]	Dimensionless hydrodynamic permeability coefficient
$K_d(x)$	[-]	Momentum flux correction factor
$K_e(x)$	[-]	Kinetic energy correction factor
$K(\infty)$	[-]	Incremental pressure drop number in the fully developed region
k	[m^2]	Hydrodynamic permeability coefficient
L	[m]	Length
L_{hy}, L_e	[m]	Hydrodynamical Entrance Length
L_{hy}^+, L_c^+	[-]	Dimensionless Hydrodynamical Entrance Length
$\dot{m}$	[kg/s]	Mass flow rate
$\underline{n}$	[-]	Normal surface vector pointing into solid
$\underline{\hat{n}}$	[-]	Unit vector in stream-wise direction
Q	[m^3/s]	Volume flow
$\underline{q}$	[m/s]	Stream-wise superficial velocity
$\underline{p}$	[Pa]	Pressure
Δp_{stack}	[Pa]	Pressure drop over stack

p_f	[Pa]	$\langle p \rangle_f$
Re	[-]	Reynolds number
Re_c	[-]	Interstitial Reynolds number
$Re_{qd_{s_\perp}}$	[-]	RRUC Reynolds number
S	[m^2]	Surface area
S_{ff}	[m^2]	Fluid-fluid interface part of ∂U_o or ∂U_f
S_{fs}	[m^2]	Fluid-solid interface
$S_{\parallel}$	[m^2]	Fluid-solid surface of stream-wise channel
$S_{\perp}$	[m^2]	Fluid-solid surface of transverse channel
t	[s]	Time
$\underline{u}$	[m/s]	Intrinsic phase average fluid velocity
u_m	[m/s]	Mean velocity
u_{max}	[m/s]	Maximum velocity
U_f	[m^3]	Fluid filled 'void' volume within an REV
U_s	[m^3]	Solid volume within an REV
U_o	[m^3]	Total volume of an REV
U_t	[m^3]	Transfer volume
$U_{\parallel}$	[m^3]	Stream-wise volume
$U_{\perp}$	[m^3]	Transverse volume
$\underline{v}$	[m/s]	Fluid velocity field within U_f
$W_s,$	[mm]	Stack width
$\underline{w}_{\parallel}, \underline{w}_{\perp}$	[m/s]	Cross sectional mean velocity in stream-wise and transverse direction
x, y	[m]	Distance, Cartesian coordinates
z	[m]	Linear RUC dimension

Greek symbols	**Dimensions**	**Definition**
α	[-]	Scalar constant defined in U_f
α^*	[-]	Aspect Ratio
β	[-]	Transverse to stream-wise proportionality coefficient
β^*	[-]	Empirical inertia parameter
Δ	[-]	Finite difference operator, change in stream-wise volume
ϵ	[-]	Porosity, (fluid volume/total volume)
μ	[N·s/m^2]	Absolute viscosity
ρ	[kg/m^3]	Fluid density
τ	[N/m^2]	Local shear stress
χ	[-]	Tortuosity
ψ, λ	[-]	Scalar quantities in U_f
ξ	[-]	Relates cross stream staggeredness

Acronyms

CFD	Computational Fluid Dynamics
DNS	Direct Numerical Simulations
GAMBIT	Geometry and Mesh Building Intelligent Toolkit
GUI	Graphical User Interface
LES	Large Eddy Simulation
O-U	Order-Upwind
P-V-C	Pressure-Velocity Coupling
RANS	Reynolds-Averaged Navier-Stokes Equations
RSM	Reynolds-Stress Model
RUC	Representative Unit Cell
RRUC	Rectangular Representative Unit Cell
SIMPLE	Semi-Implicit-Method for Pressure Linked Equations

Miscellaneous

$\langle \ \rangle$	Phase average operator U_f
$\langle \ \rangle_f$	Intrinsic phase average operator
∇	Del operator Deviation operator
∂	Partial derivative
$\{\}$	Deviation operator
$-$	Vector (underline)
$=$	Diadic (double underlined)
$\cdot$	Tensor unit product

Subscripts

exp	experimental
$\parallel$	Parallel to stream-wise direction
$\perp$	Perpendicular to stream-wise direction
f	Fluid, non-stationary matter
ff	Fluid-fluid interface
fs	Fluid-solid interface
max	Maximum
num	numerical
p	pore
s	Solid, stationary matter

Chapter 1

Introduction

A large number of scientists in a variety of disciplines are currently engaged in research that continuously contributes to the understanding and quantitative description of transport phenomena in porous media and to the solutions of models that describes them, [Bear & Buchlin (1991)]. The understanding of these phenomena in the present study is of importance, since one focus of this work is to evaluate fluid flow through porous structures. Bear & Bachmat (1991) defined a porous medium as a domain that is occupied by both the persistent solid phase, called solid matrix and the space within the domain that is not part of the solid matrix, referred to as the void space.

The traversing fluid through the void space of the porous domain consists of a two-phase fluid or single-phase fluid. The latter has received considerable attention in many applications, for example, movement of ground water through an aquifer and oil and gas through the oil reservoirs. The numerical analysis of this study will also be based on the traversing fluids through two-dimensional porous media that consist of a single-phase fluid, which may be water or air.

In addition, many other industrial processes such as in fuel cells, food production, airflow through tube banks in heat exchangers and drying process in industry, to name but a few, involve flows through porous media. Other examples of such problems and various disciplines where transport in porous media is encountered can be found in Bear & Buchlin (1991) and Kaviany (1995).

Literature reveals that Darcy[1] (1856) was amongst the first researchers who addressed the problem of flow through porous media. The results obtained by Darcy[1] (1856) were based on experimental measurements, which relate the overall discharge through a porous medium, q, linearly to the fluid pressure gradient through the hydrodynamic permeability, k, of the porous medium such that

$$q = -\frac{k}{\mu}\frac{dp}{dx}. \tag{1.1}$$

Although Darcy's law is useful and has been applied to various problems in many disciplines such as chemical, civil and mechanical engineering, the deviation from this law has been experimentally observed at high velocities, [Kaviany (1995)]. Thus it has been experimentally proven that Darcy's law is valid only at low Reynolds numbers. The flow is said to be in the Darcian regime at low Reynolds numbers ($Re < 1$).

The Reynolds number is a non-dimensional parameter formulated by Reynolds[2] (1883), and it was named after him. The Reynolds number is frequently used in fluid dynamics to determine various flow regimes (laminar or turbulent). It is defined as the ratio of inertial forces to viscous forces and is generally expressed in a dimensionless form as follows:

$$Re \equiv \frac{U\rho L}{\mu}, \tag{1.2}$$

where U is a representative mean velocity, L is a characteristic length and μ and ρ are the viscosity and density of the fluid respectively. The choice of linear dimensions and velocity appearing in the Reynolds number will affect the numerical value of the Reynolds number. Therefore, when comparing different flow results it is important that corresponding lengths and velocities are used. At low Reynolds numbers the viscous forces are dominant over the inertial forces whilst the latter is dominant at high Reynolds numbers.

A modified equation of Darcy's equation has been proposed by Forchheimer[3] (1937), to account for the deviation experienced from Darcy's law. Forchheimer[3] (1937) introduced an extra term to the Darcy equation which is quadratic in overall discharge q, and an empirical inertia parameter β^*,

$$-\frac{dp}{dx} = \frac{\mu q}{k} + \beta^* \rho q^2. \tag{1.3}$$

---

[1]Reference not read, referred to by Kaviany (1995)
[2]Reference not read, referred to by Ward-Smith (1980)
[3]Reference not read, referred to by Bear & Bachmat (1991)

The inadequacies regarding the above equation are, lack of macroscopic convective terms which relates to an ability to capture macroscopic phenomena such as boundary conditions and the fact that it is empirically based, [Du Plessis & der Westhuizen (1993)]. Many phenomenological models as described by Dullien (1975), have been published to model flow phenomena in porous media. Although Dullien (1975) reported that these models gave fairly useful results, the approach was still based on the conduction of sets of experiments. Therefore, more attention has to be paid to the development of more theoretical based models, which will reduce the need for continuous measurements.

The flow in porous media at microscopic level is governed by the Navier-Stokes transport equations. It is worth mentioning that due to the complexity of the porous media geometry, it is an arduous task to observe and measure transport quantities at this level. Therefore, to overcome these difficulties the microscopic transport equations need to be transformed to macroscopic equations. Besides these difficulties, most industrial applications only require measurable fluid properties.

The process of transforming the interstitial Navier-Stokes transport equations to measurable parameters requires amongst others, the use of the local volume averaging theories. The equations resulting from this process contain some terms that are not macroscopically measurable, due to certain information lost in the process of volume averaging of the microscopic transport equations. Therefore, a complete closure of these open terms, as referred to in literature, necessitate a conceptual model required to bring closure to the volume averaged transport equations.

Part of this thesis will present three conceptual pore-scale models that use the concept of a Representative Unit Cell (RUC) originally developed by Du Plessis & Masliyah (1988), to solve the microscopic variables present in the volume averaged transport equation. These models are referred to as the Rectangular Representative Unit Cell (RRUC) model, which represents a simplified two-dimensional configuration of the real porous structure and the transport phenomena that occur in it. Inclusion of these models in this work will provide an understanding of the mathematical basis from which an estimate of these terms and their gradients can be obtained.

As indicated earlier, many models for flow through porous media are still empirically based. Although these models gave good results as reported by Dullien (1975), it is usually considered expensive and time consuming to only depend on experimental methods. An alternative that is cost-effective for predicting flow through porous media will be analytical models.

However, due to the technological advances of modern computers, application of Computational Fluid Dynamics (CFD) modeling is considered to be more cost-effective and is commonly used. CFD employs numerical methods to solve the fundamental fluid transport equations that are derived from the laws of conservation of mass, momentum and energy.

In carrying out a CFD calculation it is necessary to follow a number of steps. These include, firstly, determining the important features of the flow to be modeled, creating the model geometry and its finite-volume mesh of grid cells. The fluid properties and the boundary conditions require specification before the set of equations may be solved, as would be the case for any calculation. The simulations in this work will be carried out using the commercial CFD software, FLUENT, which uses the finite volume approach combined with the SIMPLE algorithm developed by Patankar (1980), to solve the governing equations.

A classical parallel fluid flow driven by pressure gradients through a channel formed by two parallel plates, forms part of this study. The flow between parallel plates is called "plane Poiseuille flow" or "channel flow". Shah & London (1978) critically reviewed previous research studies on flow between parallel plates. Some of the flow characteristics presented in their review are the velocity distribution at any section, the pressure difference between any two sections and the hydrodynamic entrance length (L_{hy}).

The concept of the entrance length is often to determine if the flow has reached its steady state behaviour, as assumed in the pore-scale models. The numerical hydrodynamic entrance length obtained using the criteria based on the position where the maximum velocity is equal $0.99\,u_{max}$, $0.9977\,u_{max}$ and $0.9999\,u_{max}$ will be compared to the existing data presented in the review of Shah & London (1978). Various authors have experimentally and theoretically investigated the concept of the entrance length and various forms of approximations led to different results.

One area of industrial application of fluid flow through porous structures that is adopted in this study is an airflow through a timber stack end in a timber drying kiln. As it was mentioned earlier, this is one practical example of flow transport through two-dimensional porous media, in particular prismatic porous structures. The numerical results in this case will be tested against the three revised RRUC models and the experimental data obtained from Du Plessis (2002). The simulation for the airflow through a timber stack end was conducted using the Laminar viscous model with the aid of the two turbulence models, namely: Standard $k - \epsilon$ and Reynolds-Stress models, in the intermediate Reynolds number regime and higher.

1.1 Objectives Of This Study

The purpose of this study is twofold, with the main emphasis on numerical simulations and the secondary objective is based on the study of theoretical models, associated with equations required for the analysis of transport in porous media.

The theoretical study include the following: Three pore-scale models based on an RRUC, for both Darcian and Forchheimer regime are discussed, striving for better understanding of these models. The study of analytical plane Poiseuille flow is also necessary for this study. The purpose of the study of plane Poiseuille flow is threefold:

- The analytical solutions will assist in evaluating the accuracy of the CFD results,

- Secondly it will provide a better understanding of the definition of "fully developed" flow,

- Lastly, the results obtained here, will be useful when evaluating the assumption made with respect to fully developed flow and constant wall shear stresses in the porous media represented by a conceptual RRUC model.

The numerical part of the study include the following:

- Investigating two-dimensional laminar flow through parallel plates

- Investigating fluid flow through two-dimensional staggered porous structures.

The numerical solutions are then used to:

- Verify the fully developed flow assumption made in the derivation of the mathematical expression through the RRUC model, which forms the main part of this study.

- The results will also be validated against the existing experimental data and the analytical predicted solutions by the RRUC models.

1.2   Layout Of The Thesis

The contents of the remaining chapters are as follows:
In Chapter 2, the derivations of the macroscopic continuity and momentum equations using the the volume averaging method are recalled. In this chapter the concept of the pore-scale model employed by the RRUC models proposed by Diedericks (1999), Lloyd et al. (2004) and Cloete & Du Plessis (2006) is analyzed.

A major part of this study contains application of CFD. Thus this necessitates a brief discussion of the basic concepts of CFD and the commercial software, FLU-ENT, used to conduct the simulations, which will be discussed in Chapter 3. A classical fluid dynamic problem, with well known exact analytical solutions is presented in Chapter 4. Numerical simulation of this flow is also presented in this chapter and the numerical results will be validated against the exact analytical solution.

In Chapter 5 flow inside a two-dimensional staggered RRUC is simulated. The main aim of the simulation is to observe the flow characteristics such as velocity profile and wall shear stresses in the stream-wise and transverse channels. The exact solution in Chapter 4 is also used in this case to validate the predicted results and mostly verify the assumption made when developing models in Chapter 2. Attention is also focused on the change of flow behaviour as the porosity and Reynolds number increase and an overall discussion of the results is presented.

Practical aspects of airflow through a timber stack in a timber drying kiln are reviewed in Chapter 6. Flow characteristics for flow through a staggered section of a timber stack, modeled experimentally by Du Plessis (2002), will be modeled numerically in this section. These results are compared to the experimental data and the RRUC model results, followed by a discussion. Chapter 7 gives main conclusions and a short summary.

Chapter 2

Closure Model

2.1 Macroscopic Governing Equations

2.1.1 Volume Averaging Method

At microscopic level the flow in the porous media is governed respectively, by the continuity and Navier-Stokes equations, that is,

$$\frac{\partial \rho}{\partial t} + \nabla \cdot (\rho \underline{v}) = 0 \,, \tag{2.1}$$

$$\rho \frac{\partial \underline{v}}{\partial t} + \nabla \cdot (\rho \underline{v}\underline{v}) - \rho \underline{g} + \nabla p - \nabla \cdot \underline{\underline{\tau}} = 0 \,. \tag{2.2}$$

In equation (2.1) and (2.2), $\underline{v}$ is the interstitial velocity, ρ is the fluid density, μ is the viscosity, p is the microscopic pressure, $\underline{g}$ is the gravitational force per unit mass acting on the fluid, $\underline{\underline{\tau}}$ is the local shear stress tensor and ∇ is the del operator. For an incompressible fluid and steady flow the continuity equation (2.1) takes the form,

$$\nabla \cdot \underline{v} = 0 \,. \tag{2.3}$$

Application of these differential equations to a particular flow problem requires a mathematical description of the boundary conditions. For flow through porous media, it has been reported in the literature that due to the complexity of the pores and the matrix structures it is difficult to describe boundary conditions at the microscopic level. This lead to the study of flow through porous media in terms of the mathematical description of the macroscopic equations.

The latter is possible through the volume averaging method obtained through the application of the averaging theorem developed by Slattery[4] (1967), which expresses the volumetric average of a spatial derivative of a specific phase quantity. A detailed analysis of the theory is found in literature, presented by Bear & Bachmat (1991) and Kaviany (1995) amongst other authors.

The volume averaging theory facilitates a method of transforming the transport equations at microscopic level to the macroscopic level by volumetrically averaging over a Representation Elementary Volume (REV). Bear & Bachmat (1991) defined a Representation Elementary Volume (REV) as a volume U_0, consisting of both fluid and solid parts, which are statistically representative of the properties of the porous medium. A two-dimensional representation of an REV is shown in Figure 2.1. The volume of the fluid and solid parts within an REV are denoted by U_f and U_s respectively as illustrated in Figure 2.1.
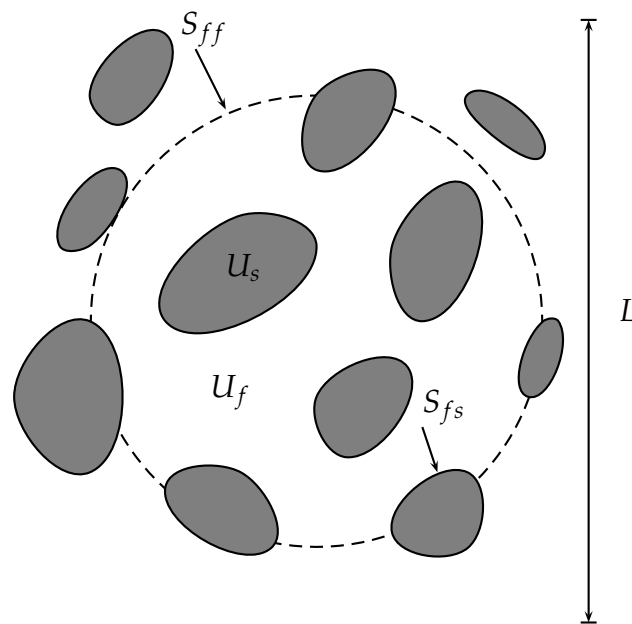
Figure 2.1: Representative Elementary Volume (REV).

---

[4]Reference not read, referred to by Bear & Bachmat (1991) and Kaviany (1995)

The porous media considered in this work consists of stationary solid matrixes and void spaces which are filled with a single-phase fluid. The porosity of the porous medium is defined by the following volume ratio of an REV as

$$\epsilon \equiv \frac{U_f}{U_0}, \tag{2.4}$$

where U_0 is the total volume and U_f is the total fluid volume. The averaging operators form a relationship between the averaged quantities and the microscopic quantities. Bear & Bachmat (1991) defined the phase average $\langle \psi \rangle$ as

$$\langle \psi \rangle \equiv \frac{1}{U_0} \iiint_{U_f} \psi \, dU, \tag{2.5}$$

and the intrinsic phase average $\langle \psi \rangle_f$ as

$$\langle \psi \rangle_f \equiv \frac{1}{U_f} \iiint_{U_f} \psi \, dU, \tag{2.6}$$

where ψ is a fluid phase tensor within an REV.

The relationship between the phase average and the intrinsic phase average follows from equations (2.4), (2.5) and (2.6) as,

$$\langle \psi \rangle = \epsilon \langle \psi \rangle_f. \tag{2.7}$$

The deviation of any fluid phase quantity $\{\psi\}$ at some point in U_f is defined as,

$$\{\psi\} \equiv \psi - \langle \psi \rangle_f. \tag{2.8}$$

If ψ is a scalar or tensorial fluid quantity, equations (2.5) up to (2.8) may be used to formulate averaging identities that aid in the volumetric phase averaging process. These identities are presented in Appendix A together with a set of averaging rules derived from the Slattery's theorem. A thorough presentation of these rules and identities can also be found in literature, [Bear & Bachmat (1991) and Kaviany (1995)].

2.1.2 Macroscopic Continuity And Momentum Equations

As mentioned previously, it seems not feasible to solve the transport equations at microscopic level, due to lack of information pertaining to the microscopic configuration of the interphase boundaries. Thus with the aid of the volumetric averaging theory outlined in Section 2.1.1, the microscopic transport quantities and equations (2.1) and (2.2) may now be integrated over an REV, to obtain macroscopic quantities. The superficial velocity $\underline{q}$ is defined as the phase average of the interstitial velocity over an REV and can be expressed as,

$$\underline{q} = \langle \underline{v} \rangle \equiv \frac{1}{U_0} \iiint_{U_f} \underline{v} \, dU \,. \tag{2.9}$$

The direction of $\underline{q}$ is referred to as the stream-wise direction and may be denoted by the stream-wise unit vector $\hat{\underline{n}}$. The drift velocity $\underline{u}$ presents the average velocity of any particle in the stream-wise direction, and is defined as the intrinsic phase average of the interstitial velocity, which yields the following equation:

$$\underline{u} \equiv \langle \underline{v} \rangle_f \equiv \frac{1}{U_f} \iiint_{U_f} \underline{v} \, dU \,. \tag{2.10}$$

The superficial and drift velocities yield a relationship known as the Dupuit-Fochheimer and is expressed as follows,

$$\underline{q} = \epsilon \underline{u} \,. \tag{2.11}$$

The volumetric averaging rules and identities mentioned in Section 2.1.1 are used to finally transform the microscopic transport equations (2.1) and (2.2) to macroscopic variables. A step by step procedure for averaging the transport equations is also presented in Appendix A. From equation (2.3) the phase averaged continuity equation yields,

$$\nabla \cdot \underline{q} = 0 \,. \tag{2.12}$$

It is further assumed that a no-slip condition applies to all fluid-solid surfaces and that the flow is free of body forces except for gavity, hence the phase average of the momentum transport equation (2.2) can be expressed as follows,

$$
\rho \frac{\partial \underline{q}}{\partial t} + \rho \nabla \cdot (\underline{q}\underline{q}/\,\epsilon) - \epsilon \rho \underline{g} + \epsilon \nabla p_f - \nabla \cdot \langle \underline{\underline{\tau}} \rangle
$$
$$
+ \rho \nabla \cdot \langle \{\underline{v}\}\{\underline{v}\} \rangle + \frac{1}{U_0} \iint_{S_{fs}} \left(\underline{n}\{p\} - \underline{n} \cdot \underline{\underline{\tau}} \right) dS = 0 \,. \tag{2.13}
$$

It is assumed that the superficial velocity field is uniform, time independent and that the gravitational force is included in the pressure term as a pressure head. Thus equation (2.13) simplifies to

$$
-\epsilon \nabla p_f = \frac{1}{U_0} \iint_{S_{fs}} \left(\underline{n}\{p\} - \underline{n} \cdot \underline{\underline{\tau}} \right) dS \,. \tag{2.14}
$$

The fluid-solid surface integral terms in equation (2.13) emerged due to loss of some information concerning the microscopic configuration of interphase boundaries, during the volume averaging process. For equation (2.14) to be of practical use the surface integral terms need to be quantified in terms of measurable variables. The process of writing equation (2.14) in terms of macroscopic variables is called closure. The closure of equation (2.14) in this study is realized through the modeling of the surface integral in terms of measurable parameters, using a conceptual model presented in the subsequent section.

2.2   A RRUC For Anisotropic Prismatic Bundles

This section does not aim to present any new models. Various existing pore-scale models will be presented, which will later be used for comparison with experimental and numerical results of flow through porous media.

A mathematical model predicting pressure gradient through isotropic and consolidated porous media was proposed by Du Plessis & Masliyah (1988). They introduced a concept of a Representative Unit Cell (RUC) to represent the geometry of the porous structure and assumed the developing flow from uniform inlet velocity through the pore sections of an RUC. Du Plessis & Masliyah (1991) extended this model to evaluate the surface integral in equation (2.14) for an isotropic unconsolidated porous medium using the same concept of an RUC and also assuming a hydrodynamically developing flow through the pore sections of an RUC.

Fully developed laminar flow was assumed to prevail throughout the entire pore sections of an RUC in the model proposed by Du Plessis (1994). This model for isotropic granular porous media also adopted the concept of a representative unit cell. All these models were compared with the empirical equations (based on the experimental observation) and they gave good correlations.

In order to analyze the interactions on the fluid-solid surfaces two sets of information are required, namely: it is necessary that the configuration of the interstitial fluid-solid surface be adequately modeled and the flow pattern within the porous medium configuration should also be addressed, [Diedericks (1999)]. These factors will be addressed by a pore-scale model referred to as an RRUC (Rectangular Representative Unit Cell), proposed by Diedericks (1999) for anisotropic porous media. A closed form of equation (2.14) is determined through this model.

The RRUC is a schematic representation of a hypothetical control volume containing a single pore, which captures the locally averaged essence of the microstructural parameters in a physical plausible manner, [Du Plessis & der Westhuizen (1993)]. The RRUC model has been successfully used to evaluate equation (2.14), for both Newtonian and Non-Newtonian fluid through isotropic porous media. Due to the success of this model, in predicting pressure drop from equation (2.14), Diedericks (1999) also extended the model introduced by Du Plessis & Masliyah (1988) and improved by Du Plessis (1994), which gave attention to isotropic porous media only.

Diedericks (1999) used the concept of an RUC to predict pressure gradients during flow through anisotropic porous structures. Diedericks (1999) applied the RRUC model to various types of anisotropic porous media, namely, two types of foamlike material, granular media and prismatic microstructure. The model of a two-dimensional anisotropic prismatic microstructure will be adopted in this study, since the industrial application of a porous medium considered in this work is an example of this type of porous domain.

Cloete & Du Plessis (2006) and Lloyd et al. (2004) adopted the existing RRUC model and made some corrections in the Darcy regime. Their corrections analyzed the assumption made by the existing model on the pressure term in the fluid-solid surface integral equation. These two models will also be presented, the aim being to test them against the experimental measurements and numerical solutions later.

The speciality of the RRUC model in general is that it was developed from basic geometry of the porous material and its results are not dependent on experimental or numerical results. It is worth mentioning that all the revised RRUC models that will be discussed in the subsequent section are based amongst others, on the plane Poiseuille assumption made by Du Plessis (1994) on his model.

In all subsequent sections in this chapter Diedericks (1999), Lloyd et al. (2004) and Cloete & Du Plessis (2006)'s RRUC models will be referred to as Model 1, Model 2 and Model 3 respectively.

2.2.1 Closure

Diedericks (1999) approximates a two-dimensional prismatic porous domain by a rectangular prismatic RRUC of linear dimensions $d_{\parallel}$ and $d_{\perp}$ in the stream-wise and transverse directions respectively, shown in Figure 2.2 (a). It is also assumed that the solid structure is represented by a rectangular prism of solid material within an RRUC and, the remaining part of the RRUC is occupied by fluid and is referred to as the void part. The solid part is represented by a rectangle of lengths $d_{s_{\parallel}}$ and $d_{s_{\perp}}$, also shown in Figure 2.2 (a).

The width of the channel where the flow passes in the stream-wise direction is denoted by $d_{c_{\perp}}$ and $d_{c_{\parallel}}$ is the width of the transverse channel. The neighbouring staggered solid rectangular blocks of an RRUC form parallel surfaces where the flow is taking place through all the duct sections. Using the geometry of a two-dimensional anisotropic RRUC, we obtain the following expressions for volumetric characteristics of the structure

$$U_0 = d_{\parallel}d_{\perp} \ ; \ U_f = \epsilon U_0 = \epsilon d_{\parallel}d_{\perp} \ ; \ U_s = d_{s_{\parallel}}d_{s_{\perp}} = (1-\epsilon)U_0 \,, \qquad (2.15)$$

and from the expression of the solid volume the porosity ϵ yields,

$$\epsilon = 1 - \frac{d_{s_{\parallel}}d_{s_{\perp}}}{d_{\parallel}d_{\perp}} \,. \qquad (2.16)$$

The effective stream-wise and transverse flow areas are defined respectively as follows,

$$A_{\perp} \equiv d_{c_{\perp}} \quad \text{and} \quad A_{\parallel} \equiv d_{c_{\parallel}} \,. \qquad (2.17)$$

The interstitial flow velocity is estimated by the following equation:

$$\underline{w}_{\parallel} = \frac{U_0}{U_{\parallel}} \, \underline{q} = \frac{\chi}{\epsilon} \, \underline{q} \,. \qquad (2.18)$$

The relationship between the stream-wise and transverse channel speeds yields the following equation:

$$w_\perp = \beta w_\parallel ,\qquad(2.19)$$

where β is the channel anisotropic factor, defined as

$$\beta = \frac{d_{c_\perp}}{d_{c_\parallel}} .\qquad(2.20)$$
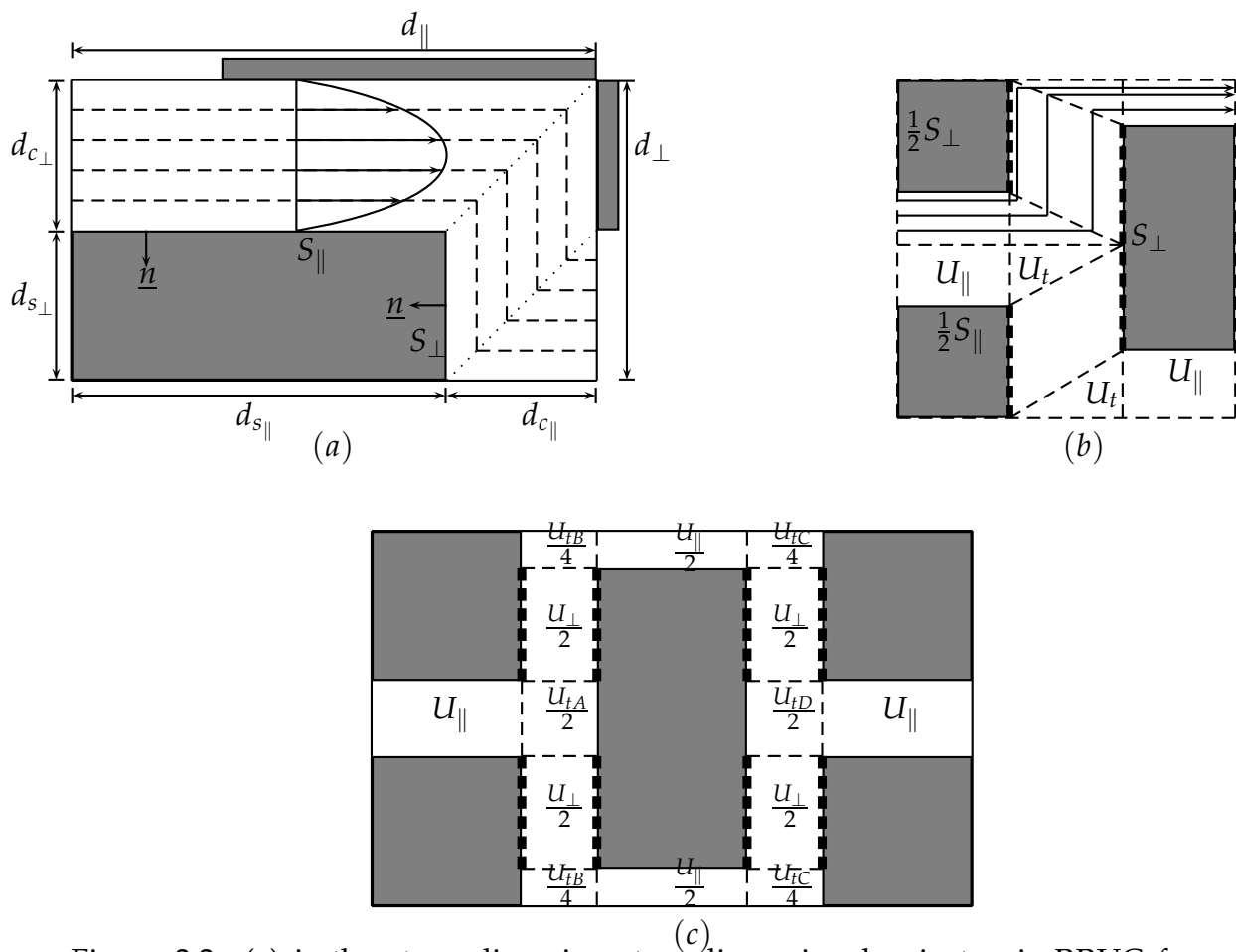
Figure 2.2: (*a*) is the streamlines in a two-dimensional anisotropic RRUC for Model 1; (*b*) is the streamlines and volume partitioning of a unit cell of Model 2 and (*c*) the volume partitioning for fully staggered configuration of Model 3.

 Cloete & Du Plessis (2006) followed an assumption made by Firdaouss & Du Plessis (2004) that the porous structure is represented by a solid phase and the unit cell represented by rectangles of the same aspect ratio and, they extended this assumption by incorporating the width of the transverse and stream-wise channel ratio. The aspect ratio is thus defined as follows,

$$\alpha^* \equiv \frac{d_\perp}{d_\parallel} = \frac{d_{s_\perp}}{d_{s_\parallel}} = \frac{d_{c_\perp}}{d_{c_\parallel}} \, .$$
(2.21)

The porosity for this type of porous structure is given by the following expression:

$$\epsilon = 1 - \left(\frac{d_{s_\perp}}{d_\perp} \right)^2 \, ,$$
(2.22)

and this equation yields the following expression:

$$\frac{d_{s_\perp}}{d_\perp} = \sqrt{1 - \epsilon} \, .$$
(2.23)

In the RRUC's models of Cloete & Du Plessis (2006) and Lloyd et al. (2004) for a staggered configuration, the fluid volume U_f is subdivided into three sub-volumes namely the stream-wise volume $U_\parallel$, the transverse volume $U_\perp$ and the transfer volume U_t. The volume, U_t, is considered simply as a transfer volume for the fluid between two adjacent shear-inducing pairs of parallel plates. The fluid volume partitions for each of the two models, [Lloyd et al. (2004), Cloete & Du Plessis (2006)], are indicated in Figure 2.2 (b) and (c) respectively.

The configuration of the transfer volumes, U_t, in the two revised RRUC models (Model 2 and Model 3) is different, resulting in one of the major differences between the two models, which is the existence of the wall shear stresses on the transverse walls. The transfer volume in Model 2 has no fluid-solid interface while part of the fluid-solid interface on the transverse walls in Model 3 form part of the transfer volume, U_t, as indicated in Figures 2.2 (b) and (c) respectively.

Model 2 assumes that the wall shear stress τ_w, exists on the entire transverse walls indicated by bold dashed lines in Figure 2.2 (b). The wall shear stresses in Model 3, acting on the fluid-solid interfaces in the transfer volume, U_t, are neglected, thus in this case the wall shear stress τ_w exists only on the remaining parts of the transverse walls as illustrated by bold dashed lines in Figure 2.2 (c). Part of this study will investigate the different approaches stated above numerically.

2.2.2 Darcy Flow Regime

The difference in these three models as mentioned previously is brought about in the analysis of the integral of the pressure term in the fluid-solid surface integral equation, which is given below for easy reference,

$$-\epsilon \nabla p_f = \frac{1}{U_0} \iint_{S_{fs}} \left(\underline{n}\{p\} - \underline{n} \cdot \underline{\underline{\tau}} \right) dS. \tag{2.24}$$

As mentioned in Chapter 1, at low Reynolds numbers $(Re \longrightarrow 0)$ the flow is dominated by viscous forces and the inertial effects are negligible. Model 1, [Diedericks (1999)], assumes that the shear stresses in the transverse channel of the RRUC do not contribute to the surface integral in equation (2.24). However, the pressure drops occurring in the transverse channels will be incorporated in the pressure deviation term. Thus the pressure deviation term contributes to the surface integral by integrating the wall shear stress over the entire fluid-solid interface $(S_{fs} = S_{\parallel} + S_{\perp})$, since the pressure drop in the transverse channels is assumed to be equal to the wall shear stresses on the sides of the channels. Model 1's [Diedericks (1999)], assumptions simplify equation (2.24) to

$$-\epsilon \nabla p_f = \frac{1}{U_0} \iint_{S_{\parallel}} (-\underline{n} \cdot \underline{\underline{\tau}}) dS + \hat{n} \frac{1}{U_0} \iint_{S_{\perp}} |\underline{n} \cdot \underline{\underline{\tau}}| dS. \tag{2.25}$$
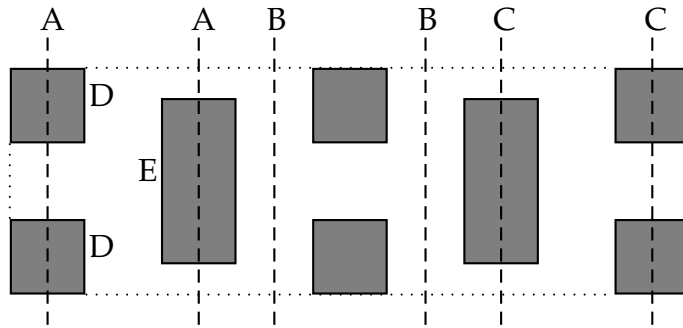
Figure 2.3: The shifting method of the RRUC.

Lloyd (2003) tested the RRUC model proposed by Du Plessis & Masliyah (1988), which have the same assumption on the pressure deviation term as Model 1, [Diedericks (1999)], against the numerical results obtained from the CFX-5 model for various porosities. The dimensionless permeability obtained from the RRUC equation gave inaccurate results when compared with the numerical values, hence, the revised RRUC model.

Lloyd (2003) evaluated each term of the pressure averaging equation for two cases [Lloyd (2003), equation (6.1)] . The first case considered a unit cell, with the boundaries in the perpendicular direction of the unit cell going through the solid region and the second case the unit cell is shifted in the stream-wise direction in such a way that the boundaries do not pass through the solid region, as depicted in Figure 2.3 by boundaries AA and BB respectively. It is reported in Lloyd (2003) that the RRUC model proposed by Du Plessis & Masliyah (1988) gave inaccurate results because it only considered the first case. The surface integral of pressure evaluated using the staggered configuration shown in Figure 2.3 is given by

$$
\begin{aligned}
\frac{1}{U_0} \iint_{S_{fs}} \underline{n}\{p\} \, dS &= \left(\frac{U_{\parallel} + U_t}{U_f} - 1 \right) \cdot \nabla \langle p \rangle \\
&= \left(\frac{1}{\chi} - 1 \right) . \nabla \langle p \rangle \,,
\end{aligned}
\tag{2.26}
$$

where $\chi = \frac{U_f}{U_{\parallel} + U_t}$ is the tortuosity for the staggered RRUC configuration. For detailed analysis and step by step calculations the reader is referred to Lloyd (2003).

The surface integral for the pressure deviation term can be written as follows using equation (2.8)

$$
\frac{1}{U_0} \iint_{S_{fs}} \underline{n}\{p\} \, dS = \frac{1}{U_0} \iint_{S_{fs}} \underline{n} p \, dS - \frac{1}{U_0} \iint_{S_{fs}} \underline{n} \langle p \rangle_f \, dS \,,
\tag{2.27}
$$

and $\langle p \rangle_f$ is assumed to be constant over the RRUC, Lloyd (2003), yielding the last term in equation (2.27) to be zero. Thus, equation (2.24) simplifies to

$$
-\epsilon \nabla p_f = \frac{1}{U_0} \iint_{S_{fs}} \left(\underline{n} p - \underline{n} \cdot \underline{\underline{\tau}} \right) \, dS \,.
\tag{2.28}
$$

Model 2, [Lloyd et al. (2004)], and Model 3, [Cloete & Du Plessis (2006)], start off with this simplified volume averaged Navier-Stokes equation to evaluate the surface integral in terms of measurable variables. The surface integral (equation (2.28)) is split into the surfaces adjacent to the stream-wise and transverse volumes, [Lloyd et al. (2004)], yielding

$$-\epsilon \nabla p_f = \frac{1}{U_0} \underline{\iint_{S_\parallel} \underline{n}\, p\, dS} + \frac{1}{U_0} \iint_{S_\perp} \underline{n}\, p\, dS$$
$$-\frac{1}{U_0} \iint_{S_\parallel} \underline{n} \cdot \underline{\underline{\tau}}\, dS - \frac{1}{U_0} \underline{\iint_{S_\perp} \underline{n} \cdot \underline{\underline{\tau}}\, dS}. \tag{2.29}$$

The underlined integrals are assumed to be zero, since equal pressures at the parallel channels will cancel out vectorially, similarly the shear stresses along the transverse channels will also cancel out vectorially, [Lloyd et al. (2004)]. The remaining pressure integral is split into a channel wall average pressure, $\overline{p_w}$, and a wall pressure deviation, $\widetilde{p_w}$ where the wall average pressure is integrated over all the RRUC possible transverse channels as shown in Figure 2.3 and we obtain the following equation:

$$-\epsilon \nabla p_f = \frac{d_s}{d} \cdot \frac{1}{U_0} \underline{\iint_{S_{\perp_{AA}}} \underline{n}\, \overline{p_w}\, dS} + \frac{d - d_s}{d} \cdot \frac{1}{U_0} \iint_{S_{\perp_{BB}}} \underline{n}\, \overline{p_w}\, dS$$
$$+ \frac{1}{U_0} \iint_{S_\perp} \underline{n}\widetilde{p_w}\, dS - \frac{1}{U_0} \iint_{S_\parallel} \underline{n} \cdot \underline{\underline{\tau}}\, dS, \tag{2.30}$$

where both $S_{\perp_{AA}}$ and $S_{\perp_{BB}}$ denote the fluid-solid interface in $U_\perp$ of a unit cell where the walls cut through solid parts and where cell walls do not cut through solid part as shown by dashed lines A and B in Figure 2.3 respectively. The wall average pressure $\overline{p_w}$ is assumed to be the same on walls D and E, leading to the underlined integral in equation (2.30) being zero. Model 2 follows the same assumption made in Model 1 by incorporating the pressure deviation term through integration of the wall shear stress over the total solid-fluid interface S_{fs}, instead of only over the stream-wise surface $S_\parallel$. The remaining surface pressure integral in equation (2.30) is substituted with the pressure integral obtained by Lloyd (2003) also given above in equation (2.26), thus, equation (2.30) yields:

$$-\epsilon \nabla p_f = \frac{1}{U_0} \iint_{S_\parallel} (-\underline{n} \cdot \underline{\underline{\tau}})\, dS + \hat{n}\frac{1}{U_0} \iint_{S_\perp} |(\underline{n} \cdot \underline{\underline{\tau}})|\, dS$$
$$+ \left(\frac{U_\parallel + U_t}{U_f} - 1 \right) \nabla \langle p \rangle. \tag{2.31}$$

Adding the pressure gradient terms equation (2.31) yields:

$$-\epsilon \nabla p_f = \frac{U_f}{U_\| + U_t} \cdot \left(\frac{1}{U_0} \iint_{S_\|} (-\underline{n} \cdot \underline{\underline{\tau}}) \, dS + \hat{\underline{n}} \frac{1}{U_0} \iint_{S_\perp} |(\underline{n} \cdot \underline{\underline{\tau}})| \, dS \right). \quad (2.32)$$

Cloete & Du Plessis (2006)'s RRUC model referred to as Model 3 also split the surface integrals in equation (2.24) into the stream-wise and transverse solid-fluid surfaces and the pressure integral is also split into the average wall channel pressure and the wall pressure deviation, then the surface integral yields,

$$
\begin{aligned}
-\nabla \langle p \rangle_f \;=\; & \frac{1}{U_f} \iint_{S_{fs_\|}} \underline{n} \overline{p_w} \, dS + \frac{d_{s_\|}}{2 d_\| U_f} \iint_{S_{fs_{\perp AA}}} \underline{n} \overline{p_w} \, dS + \frac{d_{c_\|}}{d_\| U_f} \iint_{S_{fs_{\perp BB}}} \underline{n} \overline{p_w} \, dS \\
+\; & \frac{d_{s_\|}}{2 d_\| U_f} \iint_{S_{fs_{\perp CC}}} \underline{n} \overline{p_w} \, dS + \frac{1}{U_f} \iint_{S_{fs}} \underline{n} \widetilde{p_w} \, dS - \frac{d_{s_\|}}{2 d_\| U_f} \iint_{S_{fs_{\perp AA}}} \underline{n} \cdot \underline{\underline{\tau}} \, dS \\
-\; & \frac{d_{c_\|}}{d_\| U_f} \iint_{S_{fs_{\perp BB}}} \underline{n} \cdot \underline{\underline{\tau}} \, dS - \frac{d_{s_\|}}{2 d_\| U_f} \iint_{S_{fs_{\perp CC}}} \underline{n} \cdot \underline{\underline{\tau}} \, dS \\
-\; & \frac{1}{U_f} \iint_{S_{fs_\|}} \underline{n} \cdot \underline{\underline{\tau}} \, dS, \qquad\qquad\qquad\qquad\qquad\qquad\qquad\qquad (2.33)
\end{aligned}
$$

where the $S_{fs_{\perp BB}}$ term corresponds to the instances when the boundaries of the RRUC are situated in the transverse fluid channels while the $S_{fs_{\perp AA}}$ term and $S_{fs_{\perp CC}}$ term correspond to the instance when the transverse boundaries of the RRUC intersect the second half of the solid phase and the first half of the solid phase respectively as shown in Figure 2.3.

Model 3 also assumes that the integral of the average wall channel over $S_{fs_\|}$ and the integral of the shear stress over the transverse channels are zero based on the same reasons as Model 2. However, one of the differences between Model 2 and 3 is the assumption made on the pressure deviation: Model 3 assumes that the pressure deviation is zero based on the definition of deviation, that is, the positive and the negative parts of the deviation will cancel out on each fluid-solid interface. Thus equation (2.33) reduces to

$$
\begin{aligned}
-\nabla \langle p \rangle_f \;=\; & \frac{d_{s_\|}}{2 d_\| U_f} \iint_{S_{fs_{\perp AA}}} \underline{n} \overline{p_w} \, dS + \frac{d_{c_\|}}{d_\| U_f} \iint_{S_{fs_{\perp BB}}} \underline{n} \overline{p_w} \, dS \\
+\; & \frac{d_{s_\|}}{2 d_\| U_f} \iint_{S_{fs_{\perp CC}}} \underline{n} \overline{p_w} \, dS - \frac{1}{U_f} \iint_{S_{fs_\|}} \underline{n} \cdot \underline{\underline{\tau}} \, dS. \qquad (2.34)
\end{aligned}
$$

With relevant substitutions according to the geometric assumptions of each model this equation yields the following expression

$$
\begin{aligned}
-\nabla \langle p \rangle_f \;=\;& \xi \delta p_\perp \left[\frac{d_{c_\parallel} d_\perp + d_{s_\parallel} d_{c_\perp}}{d_\parallel U_f} \right] + \delta p_\parallel \left[\frac{d_{s_\perp} d_{c_\parallel}}{d_\parallel U_f} \right] \\
& - \frac{1}{U_f} \iint_{S_{fs_\parallel}} \underline{n} \cdot \underline{\tau} \, dS,
\end{aligned}
\tag{2.35}
$$

where ξ is a parameter which relates to the cross-stream staggeredness of the solid material and $\delta p_\parallel$ is the pressure drop in the parallel channels.

The three different models, summarized above, all assume existence of the fully developed laminar flow throughout the void sections present in the RRUC. This assumption will later be investigated using numerical simulations. However based on the assumption that the flow between the parallel surfaces of the RRUC is fully developed, the wall shear stress τ_w is assumed to be constant at all channels surfaces of the RRUC and is given by $\tau_w = \frac{6\mu\hat{w}}{d_c}$. Thus equations (2.25), (2.33) and (2.35) may be written as follows

Model 1:

$$
\begin{aligned}
-\epsilon \nabla p_f \;=\;& \hat{\underline{n}} \frac{1}{U_0} \iint_{S_{fs}} \tau_w \, dS \\
=\;& \frac{\tau_{w_\parallel} S_\parallel + \tau_{w_\perp} S_\perp}{U_0} \hat{\underline{n}} \\
=\;& 6\mu\hat{w} \left(\frac{S_\parallel + S_\perp}{U_0} \right) \hat{\underline{n}};
\end{aligned}
\tag{2.36}
$$

Model 2:

$$
\begin{aligned}
-\epsilon \nabla \langle p \rangle_f \;=\;& \frac{U_f}{U_\parallel + U_t} \cdot \frac{\tau_{w_\parallel} S_\parallel + \xi \tau_{w_\perp} S_\perp}{U_0} \hat{\underline{n}} \\
=\;& \frac{S_\parallel + \xi S_\perp}{U_0} \cdot \left(\frac{U_f}{U_\parallel + U_t} \right) \cdot \frac{6\mu\hat{w}}{d - d_s} \hat{\underline{n}} \\
=\;& \frac{S_\parallel + \beta \xi S_\perp}{U_0} \cdot \left(\frac{U_f}{U_\parallel + U_t} \right)^2 \cdot \frac{6\mu \underline{q}}{\epsilon (d - d_s)} \hat{\underline{n}};
\end{aligned}
\tag{2.37}
$$

Model 3:

$$
\begin{aligned}
-\nabla \langle p \rangle_f \;=\;& \frac{1}{d_\parallel d_{c_\perp}} \left[\tau_{w_\parallel} S_\parallel + \alpha^* \xi \tau_{w_\perp} S_\perp \right] \\
=\;& \frac{1}{d_\parallel d_{c_\perp}} \left(\frac{6\mu w_\parallel}{d_{c_\perp}} (2 d_{s_\parallel}) + \alpha^* \xi \frac{6\mu w_\perp}{d_{c_\parallel}} (4 d_{s_\perp} - 2 d_\perp) \right);
\end{aligned}
\tag{2.38}
$$

where $\tau_{w_\parallel}$ and $\tau_{w_\perp}$ are the wall shear stress in the stream-wise and transverse channels respectively, α^* is the aspect ratio of the RRUC and ζ is defined as a parameter which relates to the cross-stream staggeredness of the solid material, $\zeta = \frac{1}{2}$ for fully staggered array and $\zeta = 0$ for regular array. With further substitutions relevant to each model the three final equations of the pressure gradient yield:

Model 1:

$$-\nabla p_f = \frac{12\mu\chi q}{\epsilon^2 d_\parallel d_\perp} \left(\frac{d_{s_\parallel}}{d_{c_\perp}} + \beta \frac{d_{s_\perp}}{d_{c_\parallel}} \right) \hat{\underline{n}} ; \tag{2.39}$$

Model 2:

$$-\nabla p_f = \frac{S_\parallel + \beta\xi S_\perp}{U_0} \cdot \left(\frac{U_f}{U_\parallel + U_t} \right)^2 \cdot \frac{6\mu q}{\epsilon^2(d - d_s)} \hat{\underline{n}} ; \tag{2.40}$$

Model 3:

$$-\nabla \langle p \rangle_f = \frac{12\mu q d_\perp}{d_{c_\perp}^3 d_\parallel} \left[d_{s_\parallel} + \alpha^{*4}\xi^2(2d_{s_\parallel} - d_\parallel) \right] \hat{\underline{n}} . \tag{2.41}$$

Permeability

Various flow regimes, in particular the Darcy and Forchheimer regimes may be identified in flow through porous media. However, the proportionality coefficient k, appearing in the Darcy equation (1.1) is applicable at flows with low Reynolds numbers (Darcy regime). This term is named after Darcy and is referred to as the Darcy permeability or hydrodynamic permeability. The permeability is generally determined using equation (1.1), which is empirically based, and is expressed as follows:

$$k \equiv -\frac{\mu q}{dp/dx} . \tag{2.42}$$

Much effort have been applied to model flow through porous media with no empiricism involved. The three pore-scale models discussed above successfully quantified the surface integral in the volume averaged transport equation. These results were used to determine the hydrodynamic permeability, the results from Models 2 and 3 yield the corrected expressions. When equations (2.39), (2.40) and (2.41) are applied to equation (2.42), the following dimensionless expressions predicting the hydrodynamic permeability were obtained by Diedericks (1999), Lloyd et al. (2004) and Cloete & Du Plessis (2006), respectively

Model 1:

$$K = \frac{\epsilon \left(1 - \sqrt{1 - \epsilon}\right)^2}{12(1 + \beta)\sqrt{1 - \epsilon}} ; \tag{2.43}$$

Model 2:

$$K = \frac{\left(1 - \sqrt{1 - \epsilon}\right)^3}{12\sqrt{1 - \epsilon}(1 + \beta\xi)} ; \tag{2.44}$$

Model 3:

$$K = \frac{\alpha^*(1 - \sqrt{1 - \epsilon})^3}{12[\sqrt{1 - \epsilon} + \xi^2\alpha^{*4}(2\sqrt{1 - \epsilon} - 1)]} . \tag{2.45}$$

2.2.3   Intermediate Reynolds Number Flow
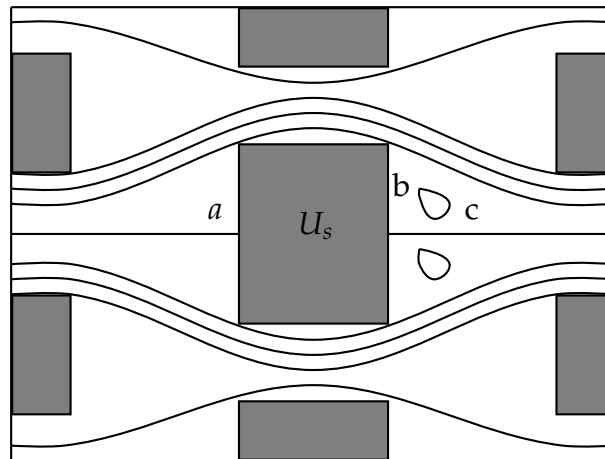
Figure 2.4: A two-dimensional representation of interstitial flow recirculation.

To account for the Forchheimer regime in the flow, Diedericks (1999)'s RRUC model for modeling the form drag of a solid obstacle is considered. Forchheimer regime in the flow occurs due to the gradual increase of the Reynolds number from low ($Re \longrightarrow 0$) to intermediate Reynolds numbers ($Re \longrightarrow 2000$). In this region the flow is still considered laminar and it is assumed that the inertia forces dominate the viscous shear stresses. Based on the latter assumption, the shear stresses are considered insignificant and therefore the contribution of the shear stress in equation (2.24) is ignored.

The predominance of the inertial forces causes recirculation downstream of the prismatic solid material as illustrated in Figure 2.4. The above assumptions simplify equation (2.24) to

$$-\epsilon \nabla p_f = \frac{1}{U_0} \iint_{S_{fs}} \underline{n}\{p\} \, dS \, .$$

(2.46)

The above equation was modeled by Diedericks (1999) at intermediate Reynolds numbers and the following three equation were obtained

$$-\nabla p_f = \frac{\rho \chi^2 \beta^2 d_{s_\perp} q^2}{2\epsilon^3 d_\parallel d_\perp} \hat{\underline{n}} \, ;$$

(2.47)

$$-\nabla p_f = \frac{\rho \chi^2 C_D d_{s_\perp} q^2}{2\epsilon^3 d_\parallel d_\perp} \hat{\underline{n}} \, ;$$

(2.48)

$$-\nabla p_f = \frac{\rho \chi^2 \beta^2 C_D d_{s_\perp} q^2}{2\epsilon^3 d_\parallel d_\perp} \hat{\underline{n}} \, ;$$

(2.49)

where C_D and β are the drag coefficient and channel anisotropic factor for models 1, 2, and 3 respectively. The difference in these equations is the appearance of C_D and β, resulted in how the speed at the inflection point is interpreted. The Darcy regime equations for each model presented above will now be asymptotically matched with each of the Forchheimer regime equations. These equations will be tested against the experimental data by Du Plessis (2002) and a suitable method will thereafter be chosen to be evaluated against the numerical solutions.

2.2.4 Asymptote Matching

Combining the results obtained for the Darcy and Forchheimer regimes by using the asymptote matching technique described by Churchill & Usagi (1972) we obtain general expressions for predicting the pressure gradient of viscous flow through an anisotropic porous medium. The next three equations follow respectively from the Darcy regime RRUC models, which are Model 1 [equation (2.39)], Model 2 [equation (2.40)] and Model 3 [equation (2.41)] added to Forchheimer regime equations, that is equation (2.47), (2.48) and (2.49) respectively

Model 1:

$$-\nabla p_f = \frac{12\chi}{\epsilon^2 U_o/z} \left(\frac{d_{s_\parallel}}{d_{c_\perp}} + \beta \frac{d_{s_\perp}}{d_{c_\parallel}} \right) \mu q\,\hat{\underline{n}} + \frac{\chi^2 \beta^2 d_{s_\perp}}{2\epsilon^2 U_0/z} \rho q^2 \hat{\underline{n}}; \tag{2.50}$$

$$-\nabla p_f = \frac{12\chi}{\epsilon^2 U_o/z} \left(\frac{d_{s_\parallel}}{d_{c_\perp}} + \beta \frac{d_{s_\perp}}{d_{c_\parallel}} \right) \mu q\,\hat{\underline{n}} + \frac{\chi^2 C_D d_{s_\perp}}{2\epsilon^2 U_0/z} \rho q^2 \hat{\underline{n}}; \tag{2.51}$$

$$-\nabla p_f = \frac{12\chi}{\epsilon^2 U_o/z} \left(\frac{d_{s_\parallel}}{d_{c_\perp}} + \beta \frac{d_{s_\perp}}{d_{c_\parallel}} \right) \mu q\,\hat{\underline{n}} + \frac{\chi^2 \beta^2 C_D d_{s_\perp}}{2\epsilon^2 U_0/z} \rho q^2 \hat{\underline{n}}. \tag{2.52}$$

Model 2:

$$-\nabla p_f = \frac{12\chi(1+\xi\beta)}{U_0/z} \left(\frac{\sqrt{1-\epsilon}}{\epsilon(1-\sqrt{1-\epsilon})^2} \right) \mu q\,\hat{\underline{n}} + \frac{\chi^2 \beta^2 d_{s_\perp}}{2\epsilon^2 U_0/z} \rho q^2 \hat{\underline{n}}; \tag{2.53}$$

$$-\nabla p_f = \frac{12\chi(1+\xi\beta)}{U_0/z} \left(\frac{\sqrt{1-\epsilon}}{\epsilon(1-\sqrt{1-\epsilon})^2} \right) \mu q\,\hat{\underline{n}} + \frac{\chi^2 C_D d_{s_\perp}}{2\epsilon^2 U_0/z} \rho q^2 \hat{\underline{n}}; \tag{2.54}$$

$$-\nabla p_f = \frac{12\chi(1+\xi\beta)}{U_0/z} \left(\frac{\sqrt{1-\epsilon}}{\epsilon(1-\sqrt{1-\epsilon})^2} \right) \mu q\,\hat{\underline{n}} + \frac{\chi^2 \beta^2 C_D d_{s_\perp}}{2\epsilon^2 U_0/z} \rho q^2 \hat{\underline{n}}. \tag{2.55}$$

Model 3:

$$-\nabla p_f = \frac{12 d_\perp}{d_{c_\perp}^3 d_\parallel} \left[d_{s_\parallel} + \alpha^{*4}\xi^2(2 d_{s_\parallel} - d_\parallel) \right] \mu q\,\hat{\underline{n}} + \frac{\chi^2 \beta^2 d_{s_\perp}}{2\epsilon^2 U_0/z} \rho q^2 \hat{\underline{n}}; \tag{2.56}$$

$$-\nabla p_f = \frac{12 d_\perp}{d_{c_\perp}^3 d_\parallel} \left[d_{s_\parallel} + \alpha^{*4}\xi^2(2 d_{s_\parallel} - d_\parallel) \right] \mu q\,\hat{\underline{n}} + \frac{\chi^2 C_D d_{s_\perp}}{2\epsilon^2 U_0/z} \rho q^2 \hat{\underline{n}}; \tag{2.57}$$

$$-\nabla p_f = \frac{12 d_\perp}{d_{c_\perp}^3 d_\parallel} \left[d_{s_\parallel} + \alpha^{*4}\xi^2(2 d_{s_\parallel} - d_\parallel) \right] \mu q\,\hat{\underline{n}} + \frac{\chi^2 \beta^2 C_D d_{s_\perp}}{2\epsilon^2 U_0/z} \rho q^2 \hat{\underline{n}}. \tag{2.58}$$

The pressure loss across the porous medium needs to be related with the flow rate, by determining a meaningful friction factor. The frictional effects introduced by the presence of the solid surfaces are governed by the following frictional coefficient for porous media

$$
\begin{aligned}
F &= \frac{\epsilon}{k} \\
&= -\frac{\epsilon}{\mu q}\frac{dp}{dx}.
\end{aligned} \tag{2.59}
$$

When evaluating theoretical solutions against experimental data, it is always suitable to do it with dimensionless parameters. Thus dimensionless F is obtained by multiplying equation (2.59) by $d_{s_\perp}^2$ and it yields

$$
Fd_{s_\perp}^2 = -\frac{\epsilon d_{s_\perp}^2}{\mu q}\frac{dp}{dx}. \tag{2.60}
$$

Equations (2.50) to (2.58) can now be expressed as the dimensionless friction factor in the same order as presented above:
Model 1:

$$
Fd_{s_\perp}^2 = \frac{12\chi}{\epsilon U_o/z}\left(\frac{d_{s_\parallel}}{d_{c_\perp}} + \beta\frac{d_{s_\perp}}{d_{c_\parallel}}\right) + \frac{\chi^2\beta^2 d_{s_\perp}^2}{2\epsilon^2 U_0/z}Re_{qd_{s_\perp}}; \tag{2.61}
$$

$$
Fd_{s_\perp}^2 = \frac{12\chi}{\epsilon U_o/z}\left(\frac{d_{s_\parallel}}{d_{c_\perp}} + \beta\frac{d_{s_\perp}}{d_{c_\parallel}}\right) + \frac{\chi^2 C_D d_{s_\perp}^2}{2\epsilon^2 U_0/z}Re_{qd_{s_\perp}}; \tag{2.62}
$$

$$
Fd_{s_\perp}^2 = \frac{12\chi}{\epsilon U_o/z}\left(\frac{d_{s_\parallel}}{d_{c_\perp}} + \beta\frac{d_{s_\perp}}{d_{c_\parallel}}\right) + \frac{\chi^2\beta^2 C_D d_{s_\perp}^2}{2\epsilon^2 U_0/z}Re_{qd_{s_\perp}}. \tag{2.63}
$$

Model 2:

$$
Fd_{s_\perp}^2 = \frac{12\chi(1+\xi\beta)}{U_0/z}\left(\frac{\sqrt{1-\epsilon}}{\epsilon(1-\sqrt{1-\epsilon})^2}\right) + \frac{\chi^2\beta^2 d_{s_\perp}^2}{2\epsilon^2 U_0/z}Re_{qd_{s_\perp}}; \tag{2.64}
$$

$$
Fd_{s_\perp}^2 = \frac{12\chi(1+\xi\beta)}{U_0/z}\left(\frac{\sqrt{1-\epsilon}}{\epsilon(1-\sqrt{1-\epsilon})^2}\right) + \frac{\chi^2 C_D d_{s_\perp}^2}{2\epsilon^2 U_0/z}Re_{qd_{s_\perp}}; \tag{2.65}
$$

$$
Fd_{s_\perp}^2 = \frac{12\chi(1+\xi\beta)}{U_0/z}\left(\frac{\sqrt{1-\epsilon}}{\epsilon(1-\sqrt{1-\epsilon})^2}\right) + \frac{\chi^2\beta^2 C_D d_{s_\perp}^2}{2\epsilon^2 U_0/z}Re_{qd_{s_\perp}}. \tag{2.66}
$$

Model 3:

$$Fd_{s_\perp}^2 = \frac{12\epsilon d_\perp}{d_{c_\perp}^3 d_\parallel} \left[d_{s_\parallel} + \alpha^{*4}\xi^2(2d_{s_\parallel} - d_\parallel) \right] + \frac{\chi^2\beta^2 d_{s_\perp}^2}{2\epsilon^2 U_0/z} Re_{qd_{s_\perp}} ; \tag{2.67}$$

$$Fd_{s_\perp}^2 = \frac{12\epsilon d_\perp}{d_{c_\perp}^3 d_\parallel} \left[d_{s_\parallel} + \alpha^{*4}\xi^2(2d_{s_\parallel} - d_\parallel) \right] + \frac{\chi^2 C_D d_{s_\perp}^2}{2\epsilon^2 U_0/z} Re_{qd_{s_\perp}} ; \tag{2.68}$$

$$Fd_{s_\perp}^2 = \frac{12\epsilon d_\perp}{d_{c_\perp}^3 d_\parallel} \left[d_{s_\parallel} + \alpha^{*4}\xi^2(2d_{s_\parallel} - d_\parallel) \right] + \frac{\chi^2\beta^2 C_D d_{s_\perp}^2}{2\epsilon^2 U_0/z} Re_{qd_{s_\perp}} . \tag{2.69}$$

$Re_{qd_{s_\perp}}$ is the Reynolds number based on the superficial velocity through porous media and the transverse channel width, and is defined as follows

$$Re_{qd_{s_\perp}} = \frac{\rho q d_{s_\perp}}{\mu} . \tag{2.70}$$

Chapter 3

Computational Fluid Dynamics

In this study we will go through the process of using a Computational Fluid Dynamics (CFD) program to describe fluid flow through channels and various porous media geometries, that will be discussed in the subsequent chapters. Thus, this necessitates a brief background information pertaining to CFD. The physical features of any fluid flow are governed by the fundamental principles of mass, momentum and energy conservation. These principles can be expressed in terms of non-linear partial differential equations.

CFD is an essential tool in fluid mechanics that approximates and numerically solves the fluid flow equations by descritizing them over the domain of interest. Many industrial applications such as petroleum reservoirs and heat exchangers involve fluid flow through channels and ducts with obstacles which resemble porous media. For this reason we need CFD programs to model fluid flow through the channels and porous media to obtain an overall understanding of the behaviour of flow through these domains.

Also in the process of designing systems such as air conditioning units, automobiles and airplanes to name a few, various tests with different parameters are required to obtain a general trend for the response of the system. It is obviously very costly and time consuming to build these models and facilities to test them.

Advances of computer power have provided an effective means of evaluating these models and obtaining solutions to the problems at hand using the CFD. Computer simulation give a general idea of the response of a system being designed and reduces the number of experimental tests that are required for design purposes. Today, the use of CFD software occurs in modeling fluid dynamics problems due to its effectiveness and economical viability.

Most fluid flows encountered in the industrial applications are turbulent, thus some kind of approximate and statical turbulence methods are needed. There are three main approaches to turbulent flow simulations namely: (i) Direct Numerical Simulation (DNS), (ii) Large Eddy Simulation (LES) and (iii) Reynolds-Averaged Navier-Stokes (RANS) [3.2].

Theoretically, turbulent flows can be simulated by numerically solving the full Navier-Stokes equations, using the DNS model, however this exercise poses difficulties since it is not practical for industrial flows and it is also expensive, [Fluent Inc. (2005)]. CFD techniques predict solutions to both laminar and turbulent flows by solving appropriate partial differential equations numerically.

Although CFD programs are convenient to use, it is crucial to understand and use the correct models and solution algorithms in the programs to obtain accurate results without excess computational time. The simulations for this study will be run using a CFD based software package, FLUENT version 6.2.16. The FLUENT software package is categorized into two sections namely: A grid generator known as Geometry and Mesh Building Intelligent Toolkit "GAMBIT" and the solver package "FLUENT".

3.1   GAMBIT

A key step in all CFD simulations is the construction of the geometric model. The computational domains in this study will be created using GAMBIT. GAMBIT is designed for constructing the geometry and creating a variety of structured and unstructured grids to be used by the solver. GAMBIT provides a graphical user interface (GUI) to receive inputs from the user.

The Gambit GUI uses basic steps for creating the two - and three - dimensional geometries, meshing and assigning zone types to a geometry. Various volumes such as cubes, cylinders, cones and pyramids are also available. The complex three-dimensional models are created using these volumes. The adjacent volumes and faces can be united, subtracted and intersected with each other. For an in depth discussion regarding the usage of each specific command in GAMBIT, the reader is referred to Fluent Inc. (2005).

Another crucial aspect in numerical computations is the generation of a mesh or grid once a geometry has been created. The grid has an impact on, amongst other things, the rate of convergence and solution accuracy. A poor constructed grid on any given geometry may result in slow convergence and inaccurate solutions. In general, a fine grid will reduce numerical errors, which will improve the accuracy of the solution. However, too fine grids will lead to huge memory requirements and if there is limited computer power available it becomes difficult to run the

simulations. A balance therefore between a fine enough grid for acceptable accuracy and computing time is sought.

For any given domain, GAMBIT recognizes the outer sides of the geometry as walls and the space between these sides as interior which can either be a fluid or solid. So it is important that after geometry and mesh generation, the boundary conditions should be specified according to the model specifications. The zones should also be set as either a fluid or solid. After the above summarized steps are completed, from the file menu in GAMBIT the mesh file is exported to FLUENT.

3.2   FLUENT Solver

After the mesh file has been exported to FLUENT, several user controlled options must be specified in the solver. The FLUENT solver supplies various options, of which only few relevant to this work will be mentioned. Once the mesh file is opened in FLUENT, it checks the grids and if there are no errors occur, then the parameters can be set to solve a particular problem.

The FLUENT solver uses a finite-volume procedure, which converts the governing differential equations presented in Section 4.1.1 into algebraic form, together with the SIMPLE (Semi-Implicit-Method for Pressure Linked Equations) algorithm to solve these equations numerically, [Fluent Inc. (2005)]. For the discretization of equations the second-order upwind scheme was selected for all the laminar flow simulations carried out. Details about the numerical methods in general and other discretization schemes can be found in literature, [Patankar (1980)].

Results are obtained by specifying certain parameters and the FLUENT solver offers default parameters which were used in our simulations. FLUENT also provides two types of solvers: coupled and segregated and the latter will be used in all the simulations conducted in this work. The default solution methods defined in FLUENT are, 2D space, segregated solver, implicit formulation, steady flow and absolute velocity formulation. The segregated approach solves the governing equations sequentially using the iterative method while, with the coupled solver, the equations are solved simultaneously.

Definition of the physical properties of the fluid and boundary conditions, as specified in GAMBIT, is also a requirement for setting up the numerical model. For fluid materials, the values of the following parameters are required: density, viscosity, thermal conductivity and specific heat capacity. The mass flow rate or pressure gradient should be specified in the case of the periodic boundary condition.

The velocity boundary condition is used to define the flow velocity at the flow inlets and the pressure outlet boundary condition requires the specification of gauge pressure at the outlet. In case of a symmetric physical geometry, a symmetric boundary condition is used which sets the normal velocity gradients to zero. The outer boundaries defined as walls, mean that the flow does not exist at these boundaries, and the boundary condition at these walls is represented by a no-slip condition.

Selection of proper numerical control, for updating the computed variables after each iteration, and modeling techniques is of importance to speed up convergence and stability of the calculations. The default under-relaxation factors shown in Table 3.1 were used to perform the laminar flows calculations. Since numerical computations can only give approximated values, a check for the convergence of the equations is made. Convergence in FLUENT is obtained by monitoring the scaled residuals and flow parameters at critical points as well as successively reducing the value of the criterion.

Table 3.1: *Solution Controls for FLUENT*

Under Relaxation		Discretization		Convergence Criteria	
Pressure	0.3	Pressure	Standard	Momentum	0.001
Density	1.0	P-V-C	SIMPLE	X-Velocity	0.001
Body Forces	1.0	Momentum (Laminar)	2nd- O-U	Y-Velocity	0.001
Momentum	0.7	Momentum ($k - \epsilon$)	1st- O-U		
		Momentum (RSM)	1st- O-U		
		T-k-E ($k - \epsilon$ & RSM)	1st- O-U		
		T-D-R ($k - \epsilon$ & RSM)	1st- O-U		

FLUENT also provides a variety of turbulence scales and prediction methods. As mentioned previously, the two approaches for the turbulence modeling that FLUENT offers are RANS and LES. In this study two RANS equations models, namely: the Standard $k - \epsilon$ model and the Reynolds-Stress model will be used to model the fluid flow through the timber stack ends at high Reynolds numbers. Various RANS equations models are tabulated in Table 3.2 and various techniques are generally described in Fluent Inc. (2005).

Table 3.2: *Turbulence Models in FLUENT*

Model	Description
Spalart Allmaras	One-Equation RANS based model
Standard $k - \epsilon$	Two-Equation RANS based model
RNG $k - \epsilon$	Two-Equation RANS based model
Realizable $k - \epsilon$	Two-Equation RANS based model
Standard $k - \omega$	Two-Equation RANS based model
Shear-stress transport (SST) $k - \omega$	Two-Equation RANS based model
Reynolds-Stress model (RSM)	Two-Equation RANS based model
Large eddy simulation	LES model

A significant factor in acquiring accuracy of the converged solution in the numerical computations as mentioned earlier, is the good quality of the grid distribution. FLUENT offers a function for post processing and analysis of the results. If satisfactory results are not obtained, the grids on the geometry have to be adapted with subsequent repeat of the numerical simulation. If the solution does not change, grid independence results are obtained otherwise, the process of refining the grids continues.

Chapter 4

Poiseuille Flow

In this chapter we shall devote our attention to a discussion of fully developed laminar flow through a channel, formed by two parallel plates. The derivation of the fully developed flow equation relies on conditions that must be approximately satisfied to produce acceptable predictions. The analytical background and numerical simulations of fluid flow through a channel will be presented, to provide a better understanding of the flow physics in channels and provide a complete picture of the hydrodynamic variations in the flow within the entire channel. An understanding of this type of flow is fundamental to our study, since one objective of this work is to verify the assumption made with respect to fully developed flow in porous structures mentioned in Chapter 2.

Fluid flow between parallel plates is widely used as a test problem for assessing the accuracy of numerical methods because of the availability of the exact solutions for this type of flow. In this study the results of the fully developed flow between parallel plates will not only aid in verifying the assumption of the RRUC model, they will also be used to determine the accuracy and application of numerical modeling simulations by comparing the predicted velocity profiles with the exact solution of the Navier-Stokes equations. The exact solution of the Navier-Stokes equation for fully developed flow between parallel plates, gives a velocity profile that helps in calculating other parameters such as shear stress, pressure drop and flow rate.

4.1   Analytical Background Of Flow Between Parallel Plates
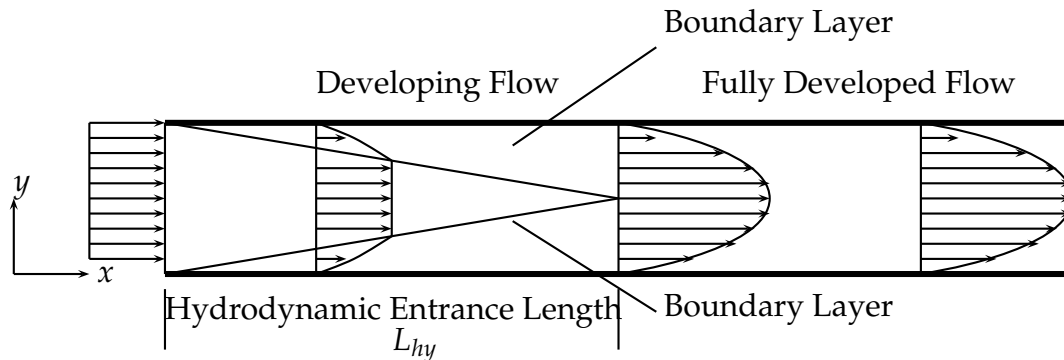
Figure 4.1: Developing and developed laminar flow.

In a case of the flow between two parallel plates separated by a distance H, the fluid enters the plates with nearly uniform velocity profile then, a thin layer referred to as a boundary layer near the wall surface develops [Figure 4.1]. The boundary layer created by viscous effects increases in size with downstream axial distance. As the boundary layer's thickness increases the velocity profile between the plates also varies with the downstream distance. At some point along the axial direction the boundary layers merge on the centerline of the plates as shown in Figure 4.1 and the velocity profile also cease varying in the axial direction.

When the velocity profile no longer changes, the flow is said to be fully developed and is referred to as Hagen-Poiseuille flow or simply plane Poiseuille flow, after the first two investigators of this type of flow. At this point where the velocity profile developed into a parabolic profile, the pressure gradient and the wall shear stress reach the state of equilibrium. The distance from the entrance of the parallel plates to the position where the fully developed flow is observed is called the entrance length. A detailed discussion of the hydrodynamic entrance length is given in subsection 4.1.2.

A brief discussion of the mathematical equations and the general underlying assumptions that are generally used to describe the basics of fluid flow between parallel plates is presented in the subsequent section, followed by a review of the entrance length of the fully developed flow. A numerical simulation of fluid flow through channels will also be presented using FLUENT.

4.1.1 Mathematical Model

In this work, an incompressible Newtonian fluid flow is considered. Based on this assumption, the continuity and the momentum equations are presented in Cartesian two-dimensional domain as follows,

Continuity:

$$\frac{\partial \rho}{\partial t} + \rho \left[\frac{\partial u}{\partial x} + \frac{\partial v}{\partial y} \right] = 0; \tag{4.1}$$

x-momentum:

$$\rho \left[\frac{\partial u}{\partial t} + u\frac{\partial u}{\partial x} + v\frac{\partial u}{\partial y} \right] = -\frac{\partial p}{\partial x} + \rho f_x + \mu \left[\frac{\partial^2 u}{\partial x^2} + \frac{\partial^2 u}{\partial y^2} \right]; \tag{4.2}$$

y-momentum:

$$\rho \left[\frac{\partial v}{\partial t} + u\frac{\partial v}{\partial x} + v\frac{\partial v}{\partial y} \right] = -\frac{\partial p}{\partial y} + \rho f_y + \mu \left[\frac{\partial^2 v}{\partial x^2} + \frac{\partial^2 v}{\partial y^2} \right]; \tag{4.3}$$

where u and v are the velocity components in the x and y directions respectively, ρ is the fluid density and μ is the coefficient of dynamic viscosity. To solve these equations relevant boundary conditions are required. The boundary conditions for the analytical solution are presented below.

Further assumptions for fluid flowing between two parallel plates are such that, the flow is in a steady state and laminar, and the gravitational force is also neglected. Let x be the axial distance along the plates and let y be the normal distance measured upward from the lower wall as shown in Figure 4.1. The flow is driven by a pressure gradient in the direction of the flow, and is slowed down by viscous forces along both plates. If we let the flow be directed along the axial direction, it implies that the velocity component v in the y-direction goes to zero and is constant in the fully developed region.

Using the assumptions made above and the fact that $v = 0$ and constant in the continuity equation (4.1), it yields that $\frac{\partial u}{\partial x} = 0$. This means that the velocity component in the x-direction depends on y only. Inserting a constant $v = 0$ into the y-momentum equation, it simplifies to $\frac{\partial p}{\partial y} = 0$, thus the pressure is a function of x only. Therefore, under fully developed conditions, the flow can be described by the Navier-Stokes equation as

$$\mu \frac{d^2 u}{dy^2} = \frac{dp}{dx}, \tag{4.4}$$

where $\frac{dp}{dx}$ is the pressure gradient in the axial direction. Equation (4.4) shows that at every point in the fully developed flow region, the total pressure force is in equilibrium with the total shear stress.

The imposed boundary conditions for this problem are:

(i) Wall boundary:

$$u = 0 \quad \text{and} \quad v = 0 \quad \text{at} \quad 0 \le y \le H; \quad 0 \le x \le L. \tag{4.5}$$

(ii) Centerline boundary:
The flow must be symmetrical about the centerline of the plates,

$$\frac{\partial u}{\partial y} = 0 \quad \text{and} \quad v = 0 \quad \text{at} \quad y = \frac{H}{2}; \quad 0 \le x \le L. \tag{4.6}$$

Integrating equation (4.4) twice and implementing above boundary conditions, yields,

$$u(y) = -\frac{dp}{dx}\frac{1}{2\mu}(yH - y^2). \tag{4.7}$$

Equation (4.7) gives a unique velocity profile and it is referred to as the plane Poiseuille flow equation. The velocity profile is the key result in fluid flow analysis because many other fluid properties are found from it, by simple relation. The maximum velocity u_{max}, is obtained from equation (4.7) by evaluating it at the centerline of the plates $\left(y = \frac{H}{2}\right)$

$$u_{\text{max}} = -\frac{dp}{dx}\frac{H^2}{8\mu}. \tag{4.8}$$

From equation (4.7) the mean velocity is obtained as follows,

$$
\begin{aligned}
u_{\text{m}} &= \frac{1}{H}\int_0^H u(y)dy \\
&= -\frac{dp}{dx}\frac{H^2}{12\mu}.
\end{aligned}
\tag{4.9}
$$

From equation (4.8) and (4.9) it follows that,

$$u_{\max} = \frac{3}{2}u_m.$$ (4.10)

The shear stress on the upper wall of the plate $(y = H)$ can be related to the velocity gradient as follows:

$$\tau_w = -\mu\frac{du}{dy}\Big|_{y=H} = \frac{6\mu u_m}{H}.$$ (4.11)

The Fanning friction factor is defined as the ratio of the wall shear stress to the flow kinetic energy per unit volume and is expressed mathematically as follows:

$$f = \frac{\tau_w}{\frac{1}{2}\rho u_m^2},$$ (4.12)

where f is the Fanning friction factor, τ_w is the wall shear stress, ρ is the fluid density and u_m is the average velocity. Pressure drop is one of the key variables when dealing with internal flows. It is needed in industrial applications such as heat sinks to determine the pumping or fan power required to maintain the flow. The expression of the friction factor in terms of the pressure drop yields:

$$f = -\frac{dp}{dx}\left(\frac{D_H}{\frac{1}{2}\rho u_m^2}\right).$$ (4.13)

The relation between the friction factor and Reynolds number for fully developed laminar flow between parallel plates, defined by Poiseuille, is derived in Appendix B and gave the following expression:

$$f\,Re = 24.$$ (4.14)

The Reynolds number Re, is based on the uniform mean velocity u_m between parallel plates and the hydraulic diameter D_H, and is expressed as follows:

$$Re = \frac{\rho u_m D_H}{\mu}.$$ (4.15)

Du Plessis & Collins (1992) in their analysis of the hydrodynamic entrance length in straight ducts, obtained the following expression for the apparent friction factor,

$$f_{\text{app}}Re = 24[1 + (0.0205/x^+)^{1.19}]^{0.42}. \tag{4.16}$$

The apparent friction factor f_{app}, is the friction factor due to the transition of fluid flow from developing flow to fully developed flow and x^+ is the dimensionless axial distance. This equation will be used later in the analysis of the wall shear stress at the fully developed flow in the porous structures.

4.1.2   Hydrodynamic Entrance Length

The hydrodynamic entrance length for channels has been investigated by various authors. For instance Shah & London (1978) presented correlations of entrance lengths obtained by various authors. In this section, a definition of the entrance length presented by Shah & London (1978) is given and the equations defining the entrance length given by McComas[5] (1967), Atkinson[6] et al. (1969) and Chen[7] (1973), will also be presented. The above models are well described in the review by Shah & London (1978). The hydrodynamic entrance length defined by Du Plessis & Collins (1992) will also be presented in this section. The aim here is to later, compare these definitions with the numerically predicted entrance length and give a general conclusion to which definition is more useful for practical applications.

The hydrodynamic entrance region in a plane Poiseuille flow may be defined as a region where the flow profiles (*i.e.* velocity profile, wall shear stress and pressure gradient) are still developing from a uniform profile to a fully developed flow profile. The hydrodynamic entrance length is in general a function of the cross-sectional geometry, the inlet profile and lastly the measure being used to assess the degree of fully developed flow, where the latter differs between author variability.

---

[5]Reference not read, referred to in Shah & London (1978)
[6]Reference not read, referred to in Shah & London (1978)
[7]Reference not read, referred to in Shah & London (1978)

Schlichting (1968) proposed an analytical expression for the entrance length for two-dimensional flow between parallel plates, with uniform inlet velocity. He obtained the following expression based on the boundary layer theory,

$$L_e = 0.04(2a)Re, \tag{4.17}$$

where $2a$ is the width channel and Re denotes the Reynolds number referred to the width of the channel, [Schlichting (1968)]. It is worth mentioning that most textbooks provide the entrance length for both parallel plates and ducts with circular cross section. However, the criterion defining these entrance lengths is not unique. For example, an often used approach to defining the entrance length, is that length at which the velocity profile becomes approximately parabolic, whilst the other criterion uses the axial location where the developing flow changes to be fully developed.

Shah & London (1978) defined the hydrodynamic entrance length, L_{hy}, as the duct length required to achieve a duct section maximum velocity of 99% of the corresponding fully developed magnitude when the entering flow is uniform. This definition together with other criteria will be used to attain the entrance length from the numerical predicted fully developed velocity profile. The entrance length is expressed non-dimensionally as follows:

$$L_{hy}^+ = \frac{L_{hy}}{D_H Re} \ , \tag{4.18}$$

where D_H is the hydraulic diameter and Re is the Reynolds number, definitions of these parameters are presented in Appendix B. McComas[5] (1967) determined an approximation of the entrance length that does not depend on a certain percentage of the fully developed velocity profile, and is expressed as follows

$$L_{hy}^+ = \frac{L_{hy}}{D_H Re} = \frac{(u_{max}/u_m)^2 - 1 - K(\infty)}{4 f Re}. \tag{4.19}$$

In the case of a fully developed flow between parallel plates with a uniform inlet velocity profile, u_{max} in equation (4.19) is the centerline velocity, u_m is the inlet velocity and $K(\infty)$ is the incremental pressure drop at the fully developed region. The value of the $K(\infty)$ is calculated in Appendix B [equation B.22] and, it corresponds to the one given by Lundgren[8] et al. (1964) listed in (Ward-Smith, 1980, Table D7, pg 236) with other values of $K(\infty)$ defined by various authors. Ward-Smith (1980) gives the following expression of the entrance length obtained by McComas[5] (1967),

$$L_{hy} \quad = \quad \frac{0.094Ub^2\rho}{\mu},\tag{4.20}$$

$$\frac{L_{hy}}{D_H} \quad = \quad 0.00588\,Re,\tag{4.21}$$

where $2b$ is the distance between the parallel plates and the hydraulic diameter is twice this distance, $D_H = 4b$. Using equation (4.15) with equation (4.20) leads to equation (4.21). The method used by McComas[5] (1967) to obtain the entrance length is reported in literature to have neglected the effect of viscous dissipation throughout the developing flow. According to Shah & London (1978), McComas[5] (1967)'s assumption yield values of the entrance length that are too low compared to values from other analysis and experiments. Ward-Smith (1980) suggests that the entrance length determined by McComas[5] (1967) should be doubled to give more realistic approximation.

For a laminar flow between parallel plates, Atkinson[6] et al. (1969) and Chen[7] (1973) proposed the following two approximations of the dimensionless entrance length which are related to the Reynolds number, respectively,

$$\frac{L_{hy}}{D_H} \quad = \quad 0.3125 + 0.011Re,\tag{4.22}$$

$$\frac{L_{hy}}{D_H} \quad = \quad \frac{0.315}{0.0175Re + 1} + 0.011Re.\tag{4.23}$$

Du Plessis & Collins (1992) obtained an analytical solution for the entrance length based on the method of asymptote matching presented by Churchill & Usagi (1972). Du Plessis & Collins (1992) deviated from the commonly used definition of the entrance length defined by Shah & London (1978) and used the method that combines the asymptotic functions for the friction factor-Reynolds number product in the upstream (developing section) and downstream (fully developed section).

The entrance length of straight ducts obtained by Du Plessis & Collins (1992) is defined as the distance between the inlet and the critical point x_c^+, where the two asymptotic functions mentioned above intersect. The advantage of this definition is that the fully developed velocity profile does not have to be known before hand, [Du Plessis & Collins (1992)]. The entrance length by Du Plessis & Collins (1992) is expressed mathematically by the following non-dimensional expression,

---

[8]Reference not read, referred to in Ward-Smith (1980)

$$L_c^+ = x_c^+ = \left[\frac{3.44}{f\,Re}\right]^2.$$ (4.24)

4.2 Numerical Flow Simulations

4.2.1 Problem formulation for parallel plate model

In this section simulations are conducted to examine the motion of an incompressible viscous fluid contained between two parallel plates. The geometric configuration for two-dimensional parallel plates and coordinate system with a uniform velocity U at the entrance, are illustrated in Figure 4.2. The channel length, L, is set to 0.2 m and the plates are separated by distance $H = 0.01$ m. The computational domain for the present problem was kept simple, thus, a structured two-dimensional and uniform grid spacing in both x and y were used.
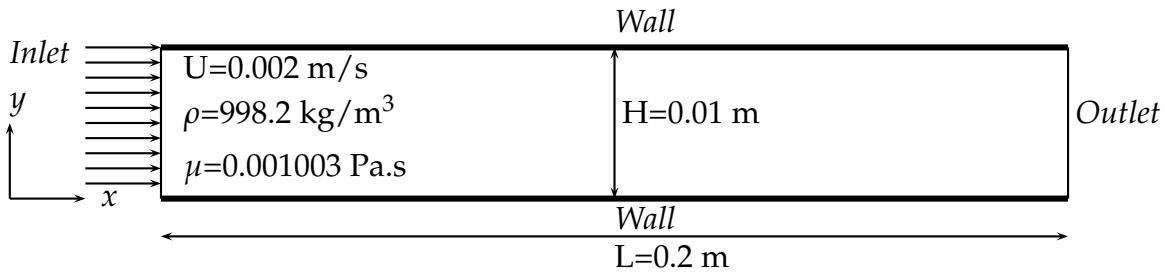
Figure 4.2: Computational Domain.

For this and all subsequent simulations in this chapter water is considered as an operating fluid with constant properties. The governing equations presented in Section 4.1.1 were solved numerically for the computational domain shown in Figure 4.2 subject to the following boundary equations:

(i) The velocity-inlet boundary condition is applied to the left edge of the domain (inlet).

(ii) The right edge (outlet) is set as the pressure outlet boundary condition.

(iii) The top and bottom edges are set as a wall boundary, where a no-slip condition is assumed.

The boundary conditions given above for the computational domain were defined in GAMBIT. The uniform velocity was assumed at the inlet. The gauge pressure needs to be specified at the outlet for the pressure outlet boundary condition. In this case the default value of 101,325 [Pa] was used. As with the analytical model a no-slip boundary condition was imposed at the top and bottom walls.

The accuracy of the converged solution is dependent amongst other things upon the grid resolution. Before proceeding further, it is necessary to determine the reliability and accuracy of the present simulations. Hence, the grid independence test on the results and validation will be investigated in the next subsection.

4.2.2 Grid Independence Test And Validation

The grid independence tests were conducted by performing computations on several grids of different resolutions. The main objective of grid independency test is to observe the solution sensitivity from the grid changes and finally the mesh that yield the grid independent results will be selected for the problem calculations. A uniform mesh in both x and y was used in all the grids tested.

The grids were refined with subsequent repeat of the numerical computations until further refinement showed less than 1% difference in the results. Different grid sizes used in this problem are tabulated in Tables 4.1 to 4.3, the first and second set of grid sizes tested the effect of the radial and axial nodes on the results. For grid independency test and code validation computations, the inlet velocity at the channel entrance was fixed yielding Reynolds number, $Re = 20$ that was used throughout this test.

The results obtained from the grid independency investigation of different meshes and also for the validation of the code were compared with the exact two-dimensional Navier-Stokes equation for fully developed flow between parallel plates, given in Section 4.1. The results are given in Tables 4.1 to 4.3. Figure 4.3 (a) and (b) show that, lower radial nodes yield a slightly different solution whereas if we keep the radial node constant and vary the axial nodes, all the results coincide with the analytical solution (Figure 4.4).

Table 4.1: *First set of grid points tested*

Grid Points	Maximum Velocity (ms^{-1})	♯ iterations
50x5	0.00145	24
60x10	0.00147	23
70x15	0.00149	26
80x20	0.00149	37
90x30	0.0015	69

Table 4.2: *Second set of grid points tested*

Grid Points	Maximum Velocity (ms^{-1})	$\sharp$ iterations
50x5	0.00145	24
50x10	0.00147	23
50x15	0.0015	28
50x20	0.0015	36
50x30	0.0015	61

Table 4.3: *Third set of grid points tested*

Grid Points	Maximum Velocity (ms^{-1})	$\sharp$ iterations
50x30	0.0015	61
60x30	0.0015	66
70x30	0.0015	72
80x30	0.0015	69
90x30	0.0015	69
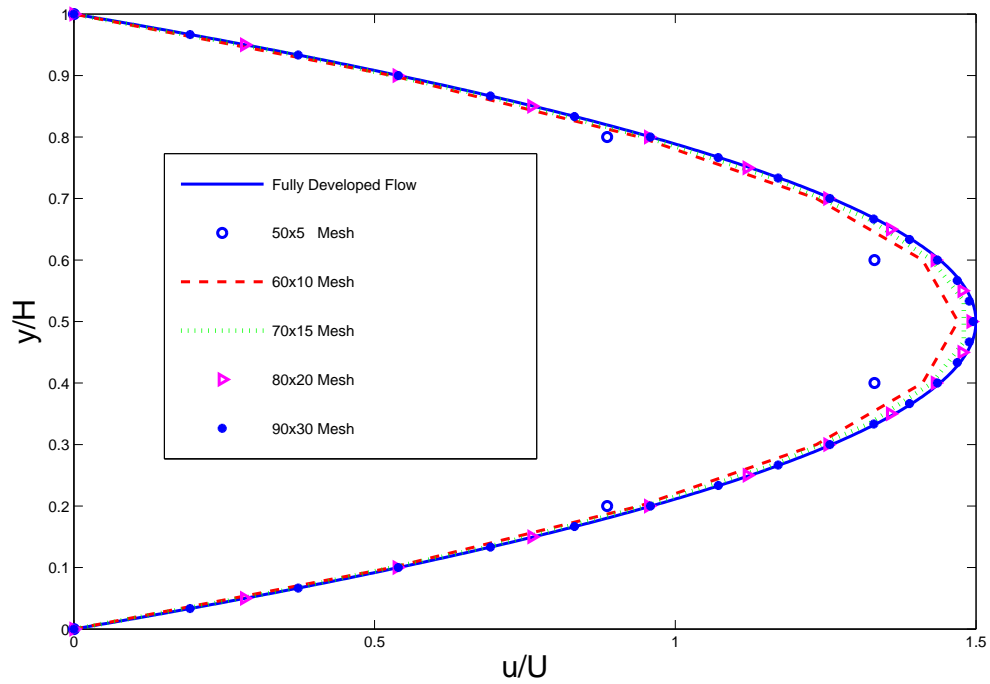
(a) Velocity profile when varying both the axial and radial nodes at $Re = 20$
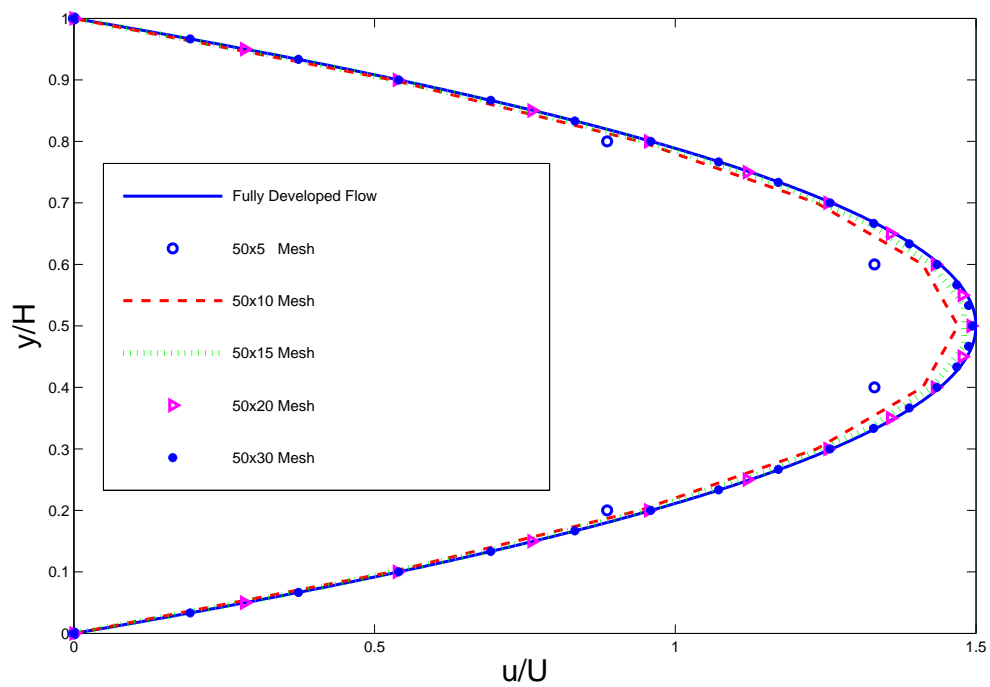
(b) Velocity profile keeping the axial nodes fixed and varying the radial nodes at $Re = 20$

Figure 4.3: Computed axial fully developed velocity profiles.
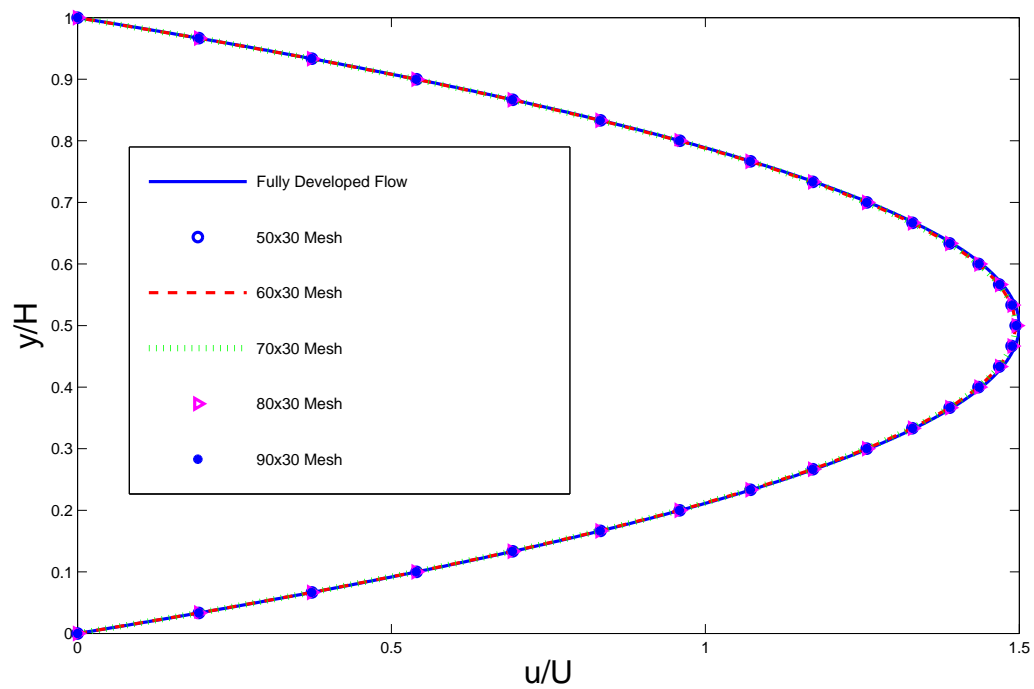
Figure 4.4: Computed axial fully developed velocity profiles when varying the axial nodes and keeping the radial nodes fixed at $Re = 20$.

Under conditions assumed when modeling the flow between the planes, according to the Poiseuille flow theory the flow is expected to attain a parabolic velocity profile. The predicted velocity vectors depicted in Figure 4.5 illustrate the flow behaviour also confirming the assumption mentioned above, and it can also be seen that the flow developed rapidly to a fully developed flow (Figure 4.5). The graphs plotted in Figure 4.4 also confirms the expected velocity profile obtained numerically.
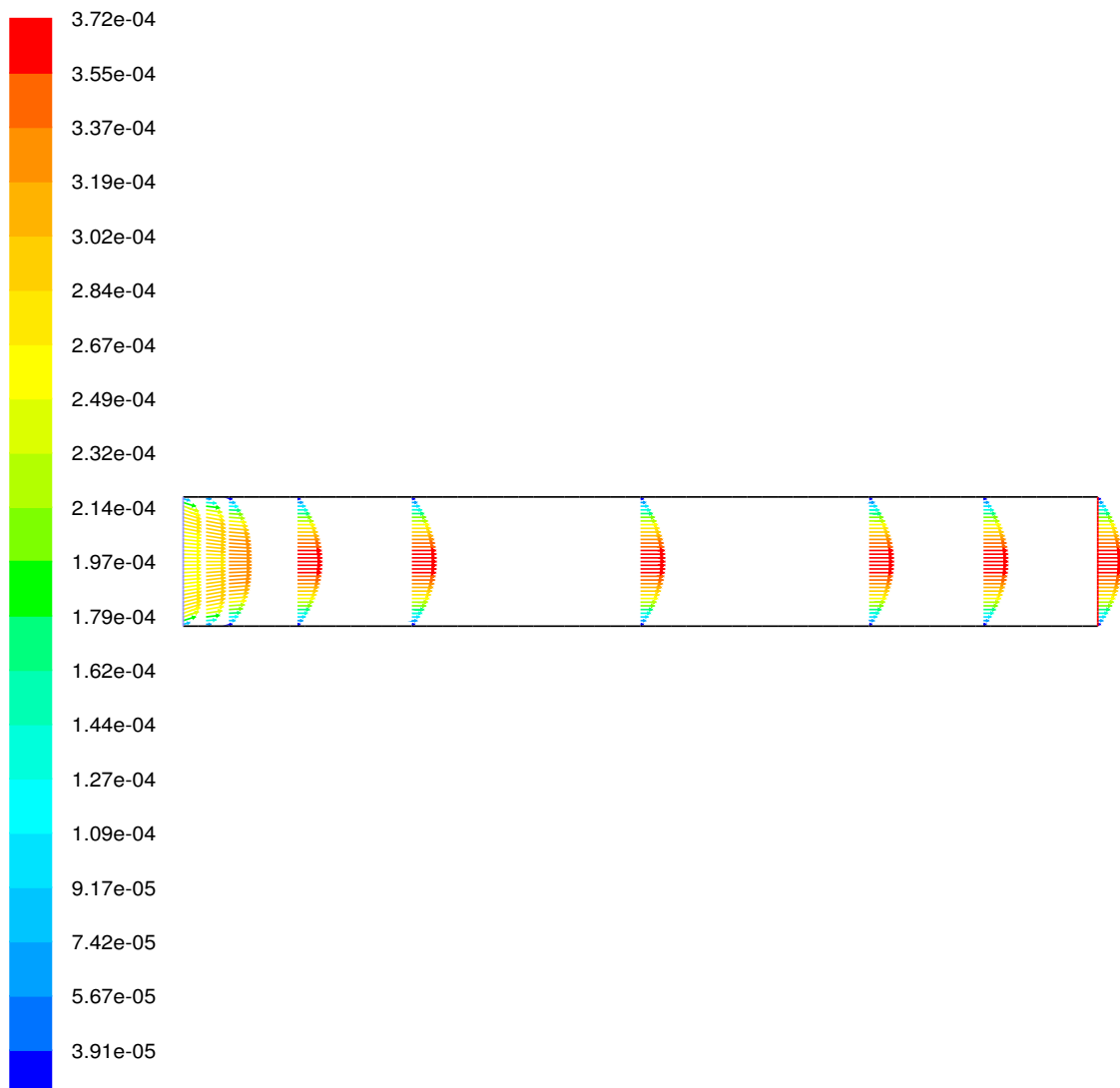
Figure 4.5: Velocity development vectors

Thus it can be concluded that the numerical simulations conducted using FLU-ENT yield good predicted values. Table 4.4 shows a short profile of the analytical and numerical results for the 50x30 mesh. The 50x30 grid size is adopted for the remaining computations and its mesh consisting of 1500 rectangular elements is shown Figure 4.6.

Table 4.4: *Analytical and FLUENT results for Validation Test*

	Numerical solution	Analytical solution
Mean u (m/s)	0.001	0.001
Mean v (m/s)	0	0
Max u (m/s)	0.0015	0.0015
Reynolds number	20	20
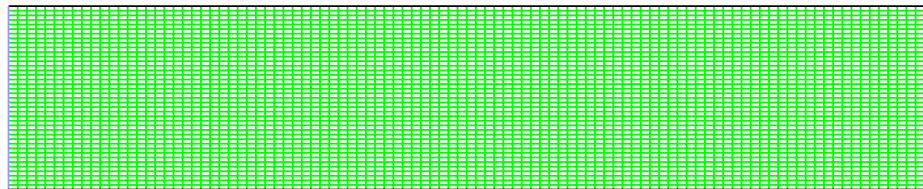
Figure 4.6: Computational domain mesh generated in GAMBIT

4.3   Numerical Solution

Computations were carried out to simulate flow between two parallel plates assuming a uniform velocity profile, U, at the channel inlet. The length of the computational domain was set to $L = 0.2$ m and the distance between the plates was set to $H = 0.01$ m.

Numerical simulations were aimed at analysis of the velocity profile through straight channels, the hydrodynamic entrance length for a range of various Reynolds numbers and the wall shear stress. The predicted hydrodynamic entrance length will be compared with the results obtained by researchers mentioned earlier and other parameters will be complimented by the analytical solutions. The computational analysis was performed using the commercial software package FLUENT, version 6.2.16.

In order to confirm the validity of the present numerical results, the predicted velocity profile for $Re = 20$ was compared with the theoretical plane Poiseuille velocity profile. The predicted results show a fairly good agreement with the theoretical solution at the grid size of 50x30 mesh. Hence, the computations henceforth were done using the 50x30 mesh. The effect of the Reynolds number on the friction factor will also be discussed, and the results will thereof be used to analyze the entrance length proposed by Du Plessis & Collins (1992).

4.3.1 Effect Of The Reynolds Number On The Hydrodynamic Entrance Length

Simulations were carried out to determine the entrance length, and it was defined as corresponding to a location where the numerical centerline velocity reaches, (I) 99 %, (II) 99.77 % and (III) 99.9 %, of its asymptotic value, respectively. As mentioned previously, the existing theoretical analysis often uses the first criterion, (I). We introduced the other two criteria, (II) and (III), to give more insight into the physical properties of the flow.

The Reynolds numbers used ranged from 1 to 200 and were obtained by varying the inlet velocity U. The dimensionless entrance length is computed using different formulas, L_{hy}/D_H and $L_{hy}/(ReD_H)$, for comparison with data from literature. In Figures 4.7 (a) and 4.7 (b), the dependence of numerical L_{hy}/D_H on Reynolds number is considered. Figure 4.7 (a) serves to demonstrate the variations of the entrance length evaluated on the basis of the above criteria, at very low Reynolds numbers that are not plotted in Figure 4.7 (b).

Figure 4.7 (a) shows that the numerical L_{hy}/D_H is not sensitive to variations of the Reynolds number at low values $Re < 60$, and increases asymptotically with increasing Reynolds number as illustrated in Figure 4.7 (b). One observable feature on the entrance length as depicted in Figure 4.7 (a), is that sets of constant values change with the Reynolds number.

Included in Figure 4.7 (b) are approximations from Atkinson[6] et al. (1969), Chen[7] (1973) and McComas[5] (1967). It is can be seen from Figure 4.7 (b) that the numerical values obtained using criterion (I), closely approximated estimations proposed by Chen[7] (1973), while values predicted by criterion (II), are closer to the estimations by Atkinson et al. (1969).

Values obtained from criterion (III) yield better approximation at $Re = 80$ & 100, and it gives an upper bound as the Reynolds number increases. It is illustrated in Figure 4.7 (b) that the entrance length increases with increasing Reynolds number, as expected. Figure 4.7 (b) confirms the criticism made by Shah & London (1978) and Ward-Smith (1980), that McComas[5] (1967)'s assumptions lead to substantially shorter entrance lengths than those from other analyses.
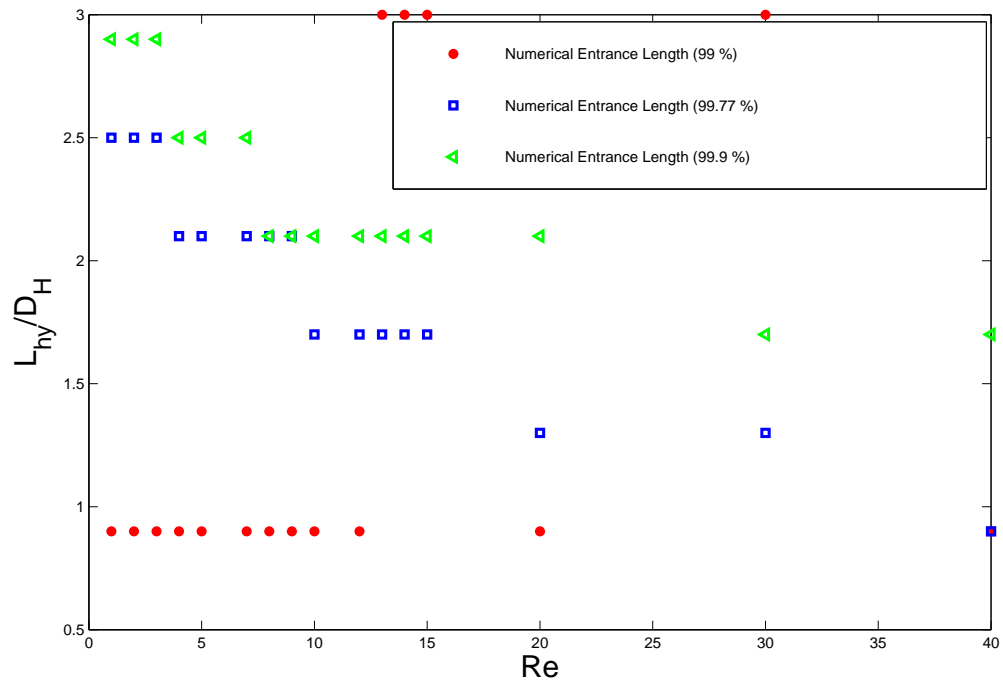
(a) $Re = 1$ up to $Re = 40$
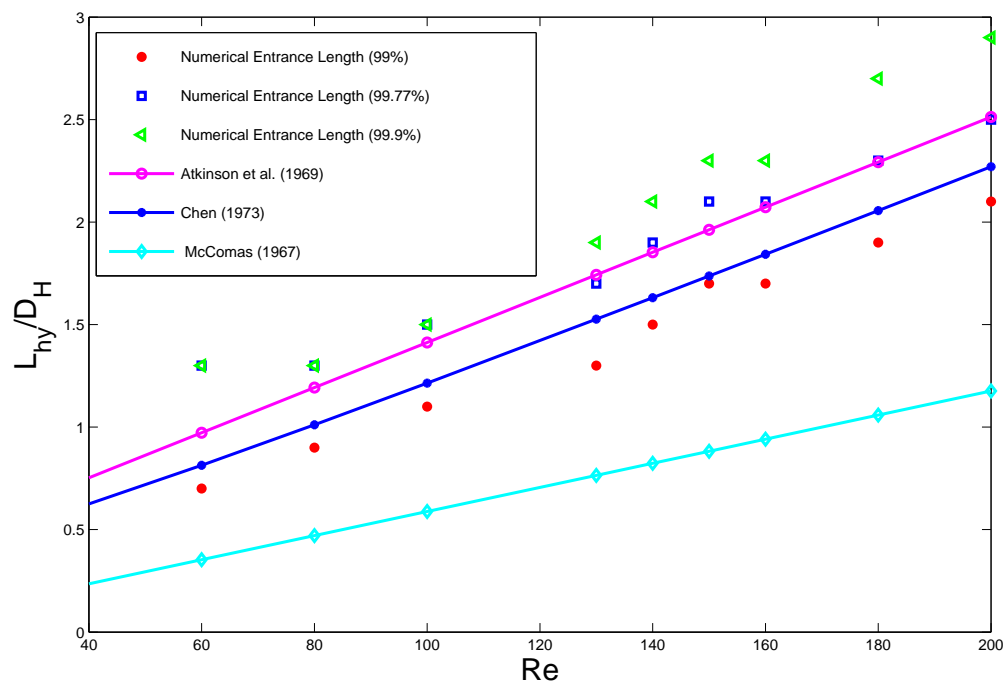
(b) $Re = 40$ up to $Re = 200$

Figure 4.7: Dimensionless Hydrodynamic Entrance Lengths L_{hy}/D_H versus the Reynolds number

The dimensionless hydrodynamic entrance lengths, $L_{hy}/(ReD_H)$, obtained numerically, together with values obtained from literature as discussed in Section 4.1.2 are listed in Tables 4.5, 4.6 and 4.7. The lengths in Table 4.5 are presented, respectively, as follows in dimensionless form

  (i) $L_{hy}^+(1)$ is obtained using equation (4.21) [McComas[5] (1967)]

 (ii) $L_{hy}^+(2)$ is obtained using equation (4.22) [Atkinson[6] et al. (1969)]

(iii) $L_{hy}^+(3)$ is obtained using equation (4.23) [Chen[7] (1973)]

(iv) L_c^+ is obtained using equation (4.24) [Du Plessis & Collins (1992)]

 (v) $L_{hy}^+(4)$ represents the values obtained numerically.

Table 4.5: Dimensionless Hydrodynamic Entrance Length (L_{hy}^+)

Re	$L_{hy}^+(1)$	$L_{hy}^+(2)$	$L_{hy}^+(3)$	L_c^+	$L_{hy}^+(4)$	
1	0.00588	0.3235	0.3206	0.0205	99 %	0.9000
					99.77 %	2.5000
					99.9 %	2.9000
2	0.00588	0.1673	0.1632	0.0205	99 %	0.4500
					99.77 %	1.2500
					99.9 %	1.4500
3	0.00588	0.1152	0.1108	0.0205	99 %	0.3000
					99.77 %	0.8333
					99.9 %	0.9667
4	0.00588	0.0891	0.0846	0.0205	99 %	0.2250
					99.77 %	0.5250
					99.9 %	0.6250
5	0.00588	0.0735	0.0689	0.0205	99 %	0.1800
					99.77 %	0.4200
					99.9 %	0.5000
7	0.00588	0.0556	0.0511	0.0205	99 %	0.1286
					99.77 %	0.3000
					99.9 %	0.3571
8	0.00588	0.0501	0.0455	0.0205	99 %	0.1125
					99.77 %	0.2625
					99.9 %	0.2625
9	0.00588	0.0457	0.0412	0.0205	99 %	0.1000
					99.77 %	0.2333
					99.9 %	0.2333
10	0.00588	0.0422	0.0378	0.0205	99 %	0.0900
					99.77 %	0.1700
					99.9 %	0.2100

Table 4.6: Dimensionless Hydrodynamic Entrance Length (L_{hy}^+)

Re	$L_{hy}^+(1)$	$L_{hy}^+(2)$	$L_{hy}^+(3)$	L_c^+	$L_{hy}^+(4)$	
12	0.00588	0.0370	0.0327	0.0205	99 %	0.0750
					99.77 %	0.1417
					99.9 %	0.1750
13	0.00588	0.0350	0.0307	0.0205	99 %	0.2308
					99.77 %	0.1308
					99.9 %	0.1615
14	0.00588	0.0333	0.0291	0.0205	99 %	0.2143
					99.77 %	0.1214
					99.9 %	0.1500
15	0.00588	0.0318	0.0276	0.0205	99 %	0.2000
					99.77 %	0.1133
					99.9 %	0.1400
20	0.00588	0.0266	0.0227	0.0205	99 %	0.0450
					99.77 %	0.0650
					99.9 %	0.1050
30	0.00588	0.0214	0.0179	0.0205	99 %	0.1000
					99.77 %	0.0433
					99.9 %	0.0567
40	0.00588	0.0188	0.0156	0.0205	99 %	0.0225
					99.77 %	0.0225
					99.9 %	0.0425

Table 4.7: Dimensionless Hydrodynamic Entrance Length (L_{hy}^+)

Re	$L_{hy}^+(1)$	$L_{hy}^+(2)$	$L_{hy}^+(3)$	L_c^+	$L_{hy}^+(4)$	
60	0.00588	0.0162	0.0136	0.0205	99 %	0.0117
					99.77 %	0.0217
					99.9 %	0.0217
80	0.00588	0.0149	0.0126	0.0205	99 %	0.0113
					99.77 %	0.0163
					99.9 %	0.0163
100	0.00588	0.0141	0.0128	0.0205	99 %	0.0110
					99.77 %	0.0150
					99.9 %	0.0150
130	0.00588	0.0134	0.0117	0.0205	99 %	0.0100
					99.77 %	0.0131
					99.9 %	0.0146
140	0.00588	0.0132	0.0117	0.0205	99 %	0.0107
					99.77 %	0.0136
					99.9 %	0.0150
150	0.00588	0.0131	0.0116	0.0205	99 %	0.0113
					99.77 %	0.0140
					99.9 %	0.0153
160	0.00588	0.030	0.0115	0.0205	99 %	0.0106
					99.77 %	0.0131
					99.9 %	0.0144
180	0.00588	0.0127	0.0114	0.0205	99 %	0.0106
					99.77 %	0.0128
					99.9 %	0.0150
200	0.00588	0.0126	0.0114	0.0205	99 %	0.0105
					99.77 %	0.0125
					99.9 %	0.0145

The solid blue line in Figure 4.8 serves to demonstrate that the entrance length predicted by McComas[5] (1967) yield a better estimate when compared with corresponding entrance of other definitions cited above, after being doubled, as suggested by Ward-Smith (1980) and Shah & London (1978). The variations of the dimensionless entrance length listed in Tables 4.5 through 4.7 are shown in Figure 4.8. It is observed that all the estimations of the entrance length considered here, decay to an approximately constant values ranging between 0.01 and 0.015 for each criteria. The 99.9 % still show an upper bound compared to other estimations. The estimated value of the dimensionless entrance length L_{hy}^{+} (not plotted), obtained from the boundary layer theory, [Schlichting (1968)], gives a constant value of 0.02, when the Reynolds number in equation (4.17) is referred to a hydraulic diameter, which is slightly higher compared to the ones shown on the graphs.

Du Plessis & Collins (1992) also investigated the flow between parallel plates numerically for Reynolds number of 200. They obtained $L_{hy}^{+} = 0.012$, based on the 99 % of the fully developed velocity profile, which is not far from the value we obtained in the present simulation as listed in Table 4.7. The entrance length proposed by Du Plessis & Collins (1992) will be discussed in the following section. Du Plessis & Collins (1992) used a different criterion from the above mentioned definitions to define the entrance length as mentioned previously.
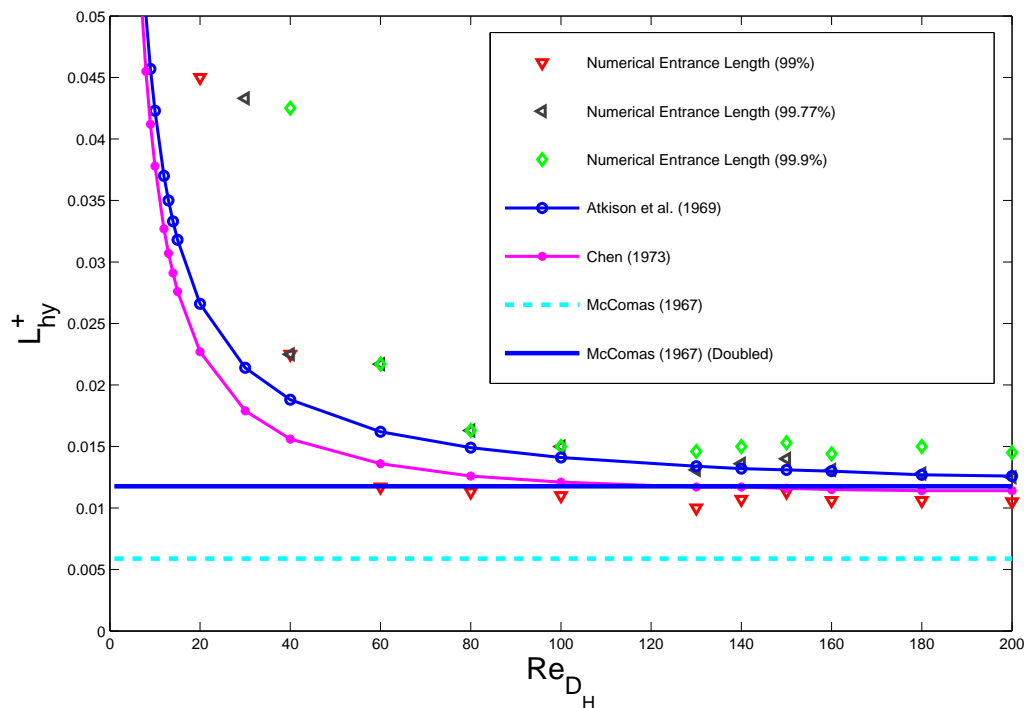

Figure 4.8: Dimensionless Hydrodynamic Entrance Lengths $L_{hy}/(ReD_{H})$.

4.3.2   Assessment Of The Predicted Fanning Friction Factor f.

Part of the numerical simulation of the flow between parallel plates was aimed at the analysis of the entrance effect resulting from the increased flow resistance due to developing boundary layers downstream of the channel inlet. The Skin Friction Factor, $C_f = \frac{\tau_w}{\frac{1}{2}\rho_{ref}v_{ref}^2}$, defined in FLUENT is consistent with the definition of the Fanning friction factor (see Appendix A). Therefore, throughout this section the skin friction factor, C_f will be referred to as the predicted Fanning friction factor.

The effects of the entrance region on the flow frictional losses are illustrated in Figures 4.9 through 4.10, where the results of the Fanning friction factor Reynolds number product are graphed as function of the dimensionless axial distance, x^+. Also plotted in these graphs is the theoretical predicted friction factor ($fRe = 24$) which corresponds to the fully developed laminar flow. The predicted Fanning friction factors from the numerical simulations show similar trends graphically at low Reynolds numbers, hence, only a few Reynolds numbers were selected for discussion.

 Du Plessis & Collins (1992) suggested that there exists a transition point at the intersection of two asymptotes which correspond respectively with the friction factor in the developing flow section and the fully developed flow section. This critical point, as referred to in Du Plessis & Collins (1992), has a value of $x^+ = 0.0205$ which represent the new proposed hydrodynamic entrance length for fluid flow between parallel plates, [Du Plessis & Collins (1992)]. The graphs in Figures 4.9 and 4.10 will be useful in the analysis of the hydrodynamic entrance length, $L_c^+ = 0.0205$, proposed by Du Plessis & Collins (1992). A straight vertical line indicating the position where $x^+ = 0.0205$ is also plotted in the same axis with the fRe graphs.

It can be observed from Figures 4.9 to 4.10 that the product fRe decreases asymptotically from the maximum value at the inlet of the channel and attains a value independent of the axial position downstream of the channel. The higher values of fRe in the entrance region of the parallel plates are due to higher velocity gradients experienced by the fluid in this region. Furthermore, it can be seen from the graphs that the numerical fRe tends to a constant value of 24, which is consistent with the plane Poiseuille flow friction factor, $(fRe)_{theory} = 24$.

The variations of fRe values as the Reynolds number is increased, are also evident in all the four figures. For $Re_{D_H} \geq 100$, the Fanning friction factor is slightly higher at the entrance region compared to lower Reynolds numbers $Re < 100$ (Figures 4.9 and 4.10). Figures 4.10 (a) and (b) clearly show that for higher Reynolds numbers the fRe product takes longer to settle at the fully developed flow region. It is seen in Figure 4.9 (a) and (b) that the numerical fRe diminishes to the fully developed flow region at approximately the same axial position pro-

posed by Du Plessis & Collins (1992) ($x^+ = 0.0205$). However, Figure 4.10 (a) and (b) illustrate that as the Reynolds number increases, the distance for fRe to approach the fully developed flow region extends to $x^+ \approx 0.05$, which is almost twice the entrance length defined by Du Plessis & Collins (1992). This behaviour is expected since the hydrodynamic entrance length for the developing flow in a channel increases linearly with the Reynolds numbers.
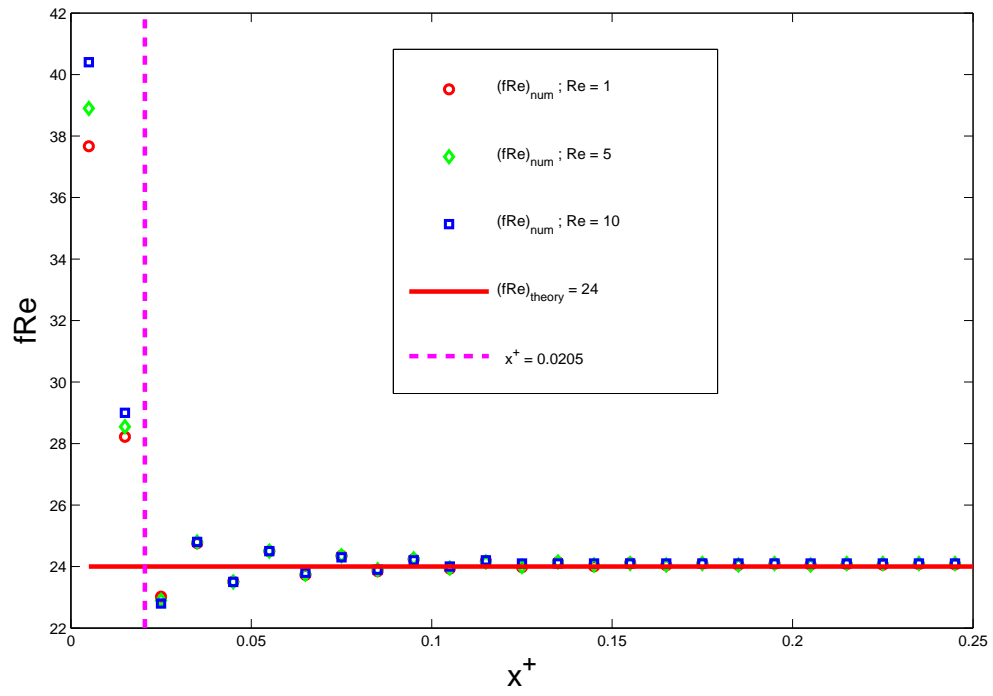
(a)
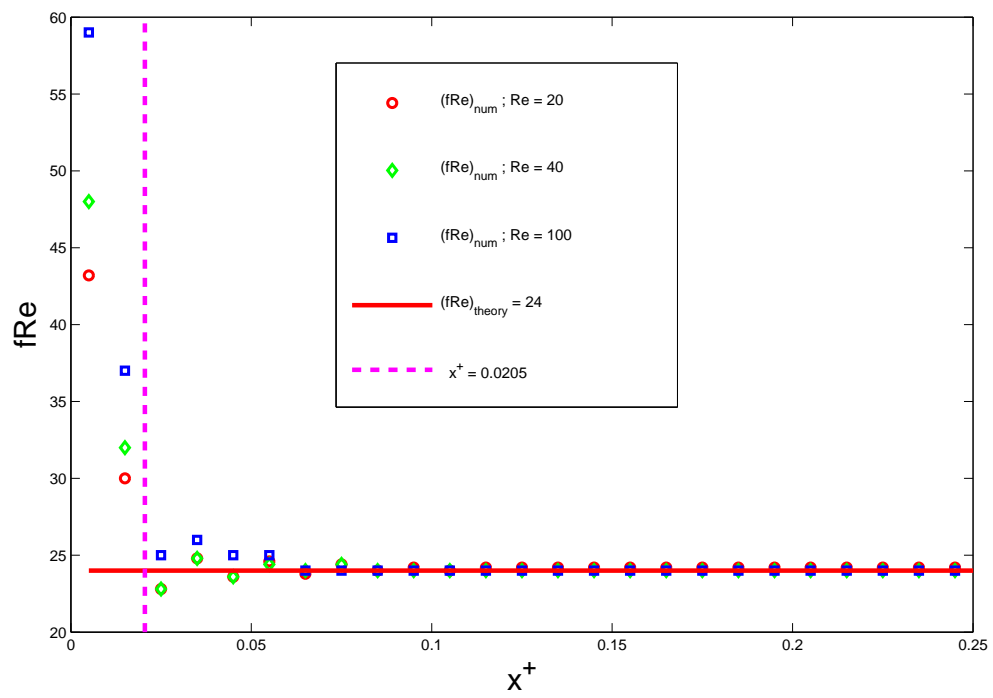
(b)

Figure 4.9: $f_{\mathrm{app}}Re$ for predicted developing laminar flow.
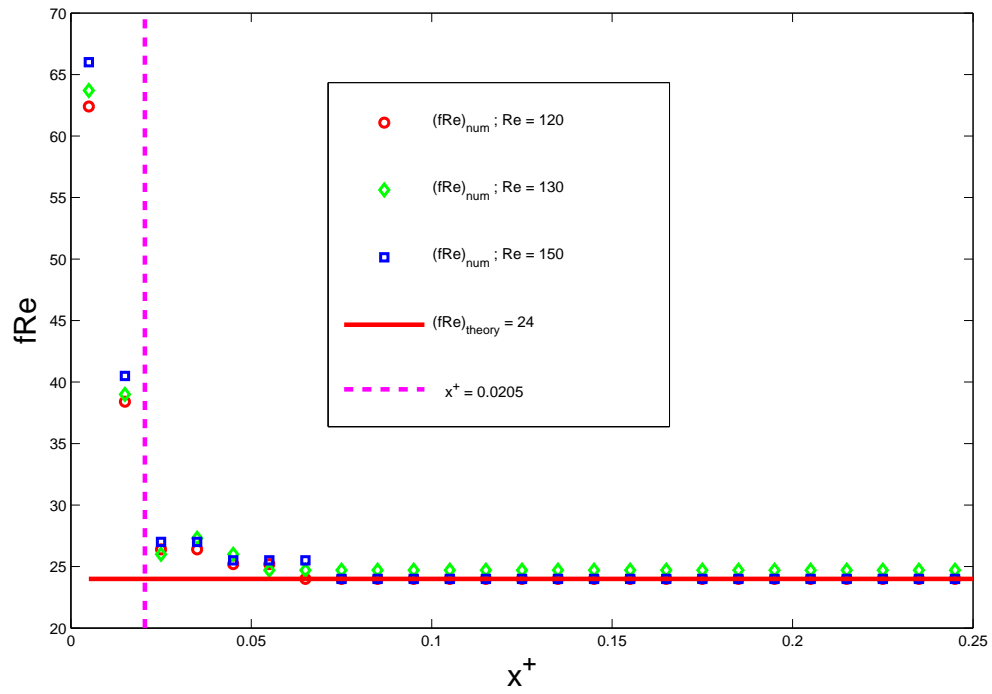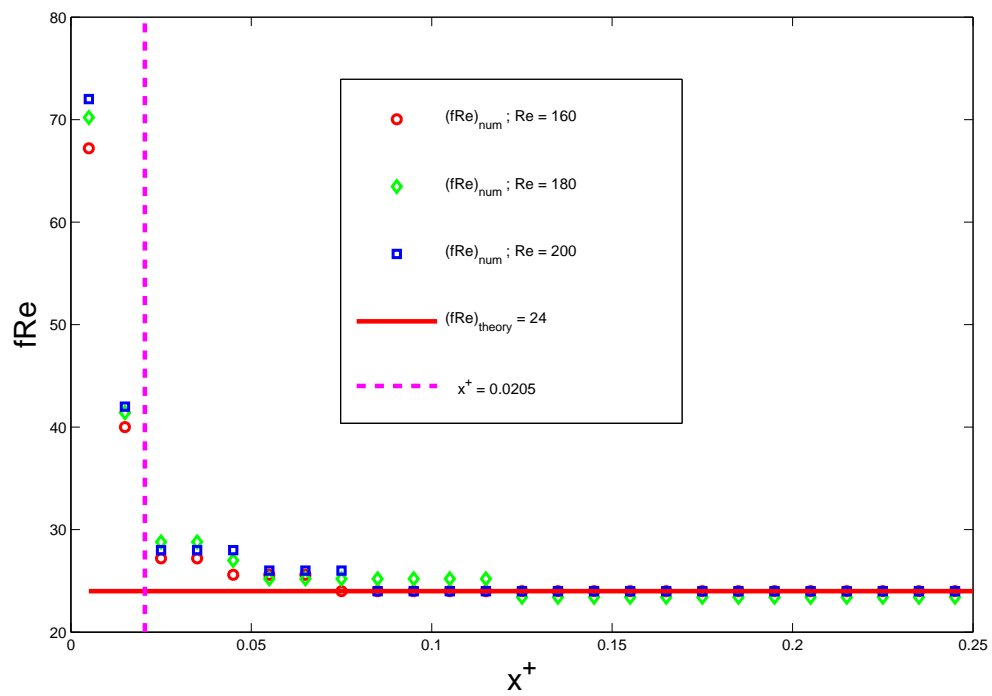
Figure 4.10: $f_{\mathrm{app}}Re$ for predicted developing laminar flow.

4.4   Discussion

To evaluate the accuracy of the calculations, the calculated velocity distribution, entrance length, and pressure drop were compared with those obtained by previous researchers and analytically. The numerical velocity profile predicted the plane Poiseuille flow velocity profile accurately, after some grid refinements as presented in subsection 4.2.2.

All criteria used to obtained the entrance length exhibit good sensitivity. However they all lead to different values of L_{hy} with criterion (III) giving the upper bound for L_{hy}. The difficulty with criteria using the percentage approximations is that they require knowledge of the centerline velocity to obtain L_{hy}. Whereby the computational flow field might not be accurately computed, due to the uncertainties of the CFD techniques. This will definitely lead to the incorrect estimations of the entrance length. There is no theoretical evidence which awards, any of the criteria used to define the entrance length in this study, to be better than any other. Thus, the advantage of one criterion above the other will be suitable through different applications.

However, based on numerical observations the entrance length proposed by Du Plessis & Collins (1992) seem to be the best criteria to determine the entrance length since it does not depend on any computed parameters. As mentioned earlier the expression for the entrance length proposed by Du Plessis & Collins (1992), is a function of the apparent friction factor and can be useful in the developing flow regions and fully developed flow regions. The entrance length, $L_c^+ = 0.0205$, estimates the boundary layer theory, entrance length $L_e = 0.02$ proposed by Schlichting (1968) fairly well. This also confirms that the entrance length proposed by Du Plessis & Collins (1992) may be sufficient to predict the hydrodynamic entrance length between parallel plates.

Chapter 5

Flow Through Porous Domain

The derivation of the RRUC model relies on various assumptions to predict the pressure gradient through porous media. These assumptions are such that the model should be as simple as possible, but still give accurate results. A fully developed laminar flow is assumed to prevail throughout the stream-wise and transverse channels of the RRUC geometry. However, due to the positioning of neighbouring RRUC's the fluid will take a tortuous path when moving through the RRUC geometry, thus, deviations from the parallel plate model may be expected. This is our goal in this chapter, to simulate fluid flow through the porous structures with an emphasis on verifying an assumption made with respect to the plane Poiseuille flow between the adjacent surfaces of solid rectangles within the RRUC.

In case of plane Poiseuille flow a constant wall shear stress is therefore assumed to exist throughout the fluid-solid interface in both the stream-wise and transverse channels. The numerical wall shear stress in the porous structures will also be analyzed. In addition, the surface areas on which the wall shear stress acts according to Model 2 and Model 3 mentioned in Chapter 2 will also be investigated numerically. The results obtained from these simulations will be compared with the analytical solutions and the numerical results of the fully developed flow between uninterrupted parallel plates discussed in the previous chapter.

5.1 Flow Simulation

Eight different cases, each representing a different geometry in terms of variation of porosity, similar to the geometry shown in Figure 5.1 were constructed and meshed using GAMBIT. The objective of the present numerical simulation is to assess the variation of the flow profile (velocity profile and wall shear stress) within the channels of these geometries. For simplification a configuration of square cells staggered in a rectangular array (SCSRA) similar to the one studied by Firdaouss & Du Plessis (2004), was adopted. The dashed lines on Figure 5.1 represent what is referred to as a unit cell in the RRUC model and the unit cell together with extended solid lines square show a computational model. The computational domain was translated during the construction of the geometry to obtain more realistic results, as schematically shown in Figure 5.2.

The different geometries, each representing a specific porosity ϵ, will be referred to as Cases 1 through 8 throughout this chapter. In order to obtain the wide range of porosities the width $(2d_{\parallel})$ and the length $(d_{\perp})$ of the rectangle were kept constant at 0.2 m and 0.1 m respectively, and we varied the size of the square embedded within the rectangle from 0.09 m to 0.01 m. The porosities for each case and mesh elements are listed in Table 5.1. A range of eleven Reynolds numbers were used in the computations of each case. The stream-wise average channel velocity $w_{\parallel}$, was altered with other fluid parameters fixed to vary the interstitial Reynolds number.

The interstitial Reynolds number is derived from the Reynolds number for channel flow at some mean velocity, defined in Chapter 4 by equation (4.15). Thus an interstitial Reynolds number for the stream-wise flow between the parallel sections of an RRUC, a distance d_c apart, is expressed as follows:

$$Re_c = \frac{\rho w 2 d_c}{\mu}, \tag{5.1}$$

where w is the average channel velocity, ρ is the fluid density, μ is the dynamic viscosity and $2d_c$ is derived from the hydraulic diameter D_H, which is defined as four times the cross sectional flow area divided by the wetted perimeter.

The Quadrilateral-Pave scheme, [Fluent Inc. (2005)], was used in meshing all geometries considered and the resulting grid distribution for one of the computational domain is shown in Figure 5.3. Suitable number of elements were used to obtain convergent results. When adjacent RRUC's are tightly fitted in a rectangular array, they can therefore be characterized by a geometry periodically repeating in the flow direction. Hence, we chose a periodic boundary at the inlet and outlet of the computational domain.

Symmetry boundary condition was imposed on four horizontal dashed line surfaces shown on Figure 5.2. All solid lines in Figure 5.2 were specified as walls and a no-slip boundary condition was applied to all these walls. For all cases considered in these simulations the numerical iteration criterion for x and y velocity and the continuity equations was set to less than 10^{-5}. The Fluent post processor was used to analyze the results.
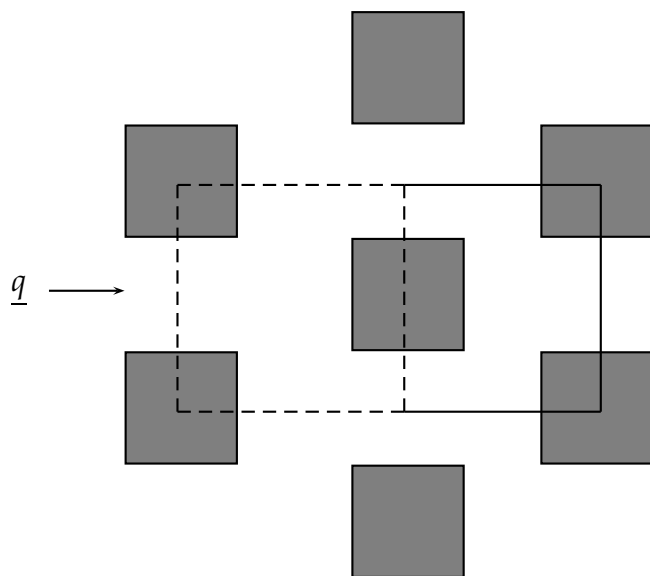
Figure 5.1: Staggered arrays of squares with a unit cell.
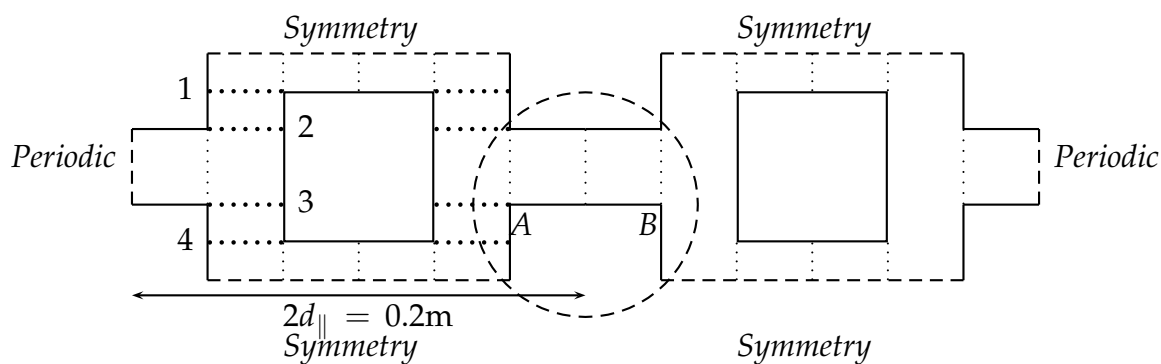
Figure 5.2: Computational Domain

Table 5.1: *Parameters and Conditions for Validation Test*

Case	Mesh Elements	$2 \times d_{\parallel}$ (m)	$d_{\perp}$ (m)	$d_{s_{\parallel}} = d_{s_{\perp}}$ (m)	$\epsilon = 1 - \left(\frac{d_{s_{\perp}}}{d_{\perp}}\right)^2$
1	7600	0.2	0.1	0.09	0.19
2	14400	0.2	0.1	0.08	0.36
3	20400	0.2	0.1	0.07	0.51
4	6400	0.2	0.1	0.06	0.64
5	7675	0.2	0.1	0.05	0.75
6	8400	0.2	0.1	0.04	0.84
7	23296	0.2	0.1	0.03	0.91
8	9600	0.2	0.1	0.02	0.96

Figure 5.3: Computational Grid

5.2   Numerical Results

In an attempt to evaluate the assumption of constant wall shear stresses and fully developed flow made in the RRUC model, we considered plane parallel flow through a two-dimensional porous geometry. Table 5.1 gives the dimensions of the eight geometries considered for this simulation and each case was studied for different combination of Reynolds numbers. The length of the parallel surfaces under investigation denoted by $d_{s_\parallel}$ of different porosities are also listed in Table 5.1. The Reynolds number used in all the computations of this particular problem is given by the following formulas for the stream-wise and transverse directions, respectively:

$$Re_{c_\parallel} = \frac{2d_{c_\perp}\rho w_\parallel}{\mu} \tag{5.2}$$

$$Re_{c_\perp} = \frac{2d_{c_\parallel}\rho w_\perp}{\mu} \tag{5.3}$$

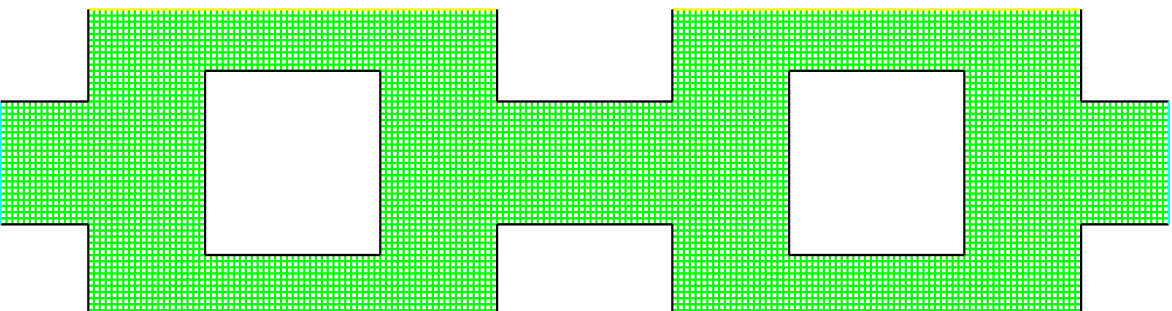where $d_{c_\perp}$ and $d_{c_\parallel}$ are the widths of the channels in the stream-wise and transverse directions, and $w_\parallel$ and $w_\perp$ are the stream-wise and transverse average channel velocities. The presentation of the computational results in this section will be divided into two parts. The first part will present the numerical velocity profiles at the stream-wise and transverse parallel surfaces and the second part will discuss the wall shear stresses also at the stream-wise and transverse parallel surfaces.

The analysis of the predicted velocity profiles and the wall shear stresses will be made from the stream-wise parallel surfaces indicated by a dashed line circle illustrated in Figure 5.2 and at the planes created in the transverse channels at positions 1, 2, 3 and 4 as indicated in Figure 5.2, since the main aim is to investigate the fully developed flow assumption and the wall shear stress, that takes place between these parallel plates.

Simulations were conducted over a range of Reynolds numbers given in Table 5.2, for each computational geometry listed in Table 5.1. It should be noted that care must be taken when calculating the Reynolds number corresponding to a desired velocity profile and wall shear stress. There are four transverse channels in the computational domains and the velocity profiles are the same at various locations for the respective porosities. Although eleven different Reynolds numbers were used for the computations of each geometry, only few results will be presented since their trends are similar.

Table 5.2: Different Reynolds numbers for the RRUC model

$Re_{c_\parallel} = \frac{2d_{c_\perp}\rho w_\parallel}{\mu}$
0.1
0.3
0.5
1
2
5
10
15
20
30
40

5.2.1 Velocity Distribution

The velocity distribution at the inlet of the porous geometry (Case 1 to 8) yields a parabolic profile, as demonstrated in Figure 5.4 by velocity vectors, this was achieved by applying the periodic boundary conditions at the inlet and outlet cross-sections. There were no specifications made about the flow-field and the flow through the computation geometry was driven by the specified mass flow rate. Due to the geometry effect the axial velocity profile will experience changes from the initial value to the final value after flowing over a distance from the inlet.

The results of the simulation will be presented graphically for selected Reynolds numbers and porosities and they will all be compared with the theoretical fully developed laminar flow between parallel plates (plane Poiseuille flow). The velocity distribution in the stream-wise and transverse channels at each position was normalized by the value of the uniform inlet average velocity $w_\parallel$ and $w_\perp$ respectively, while the position was normalized with the channel height $d_{c_\perp} = d_{c_\parallel}$ for all the configurations.

In order to follow the development of the velocity profile along the stream-wise channel, the results were obtained at different axial locations starting at the leading edge up to the middle of the parallel plates indicated by a dashed line circle in Figure 5.2 for all the porosities considered. To study more closely the velocity development between the leading edge and 0.1 m downstream (middle line), measurement positions of 0.0025 m increment were selected. The leading edge will be referred to as edge A.

Figures 5.5 (a) and (b) show the velocity profiles from the leading edge up to 0.1 m downstream (middle line) for $Re_{c_{\parallel}} = 5$ and 30, respectively. The two plots in Figure 5.5 (a) and (b) are nearly identical indicating that for this particular geometry the Reynolds number does not have an effect on the development of the flow. The velocity profile from the leading edge A of the parallel surface under investigation up to 0.0575 m downstream deviates from the Poiseuille velocity profile as depicted in Figure 5.5 (a) and (b). It is also seen that for both Reynolds numbers, $Re_{c_{\parallel}} = 5$ and 30, the velocity profile cease to change at approximately $x = 0.06$ m downstream.

For the same Reynolds numbers as in Figure 5.5 (a) and (b), but different porosity of $\epsilon = 0.36$, the flow is already fully developed at $x = 0.065$ m and the numerical velocity profile shows very close agreement with the theoretical fully developed flow. Figures 5.7 and 5.8 show that there is an increment of 0.0025 m downstream for the velocity profile to reach the fully developed profile when compared to the graphs shown in Figure 5.5 and 5.6. This small change might be due to the change in porosity. However, the flow profile still show the same pattern as those discussed above.

The velocity gradient at the leading edge A of the cases discussed above, is due to the change of flow direction from the transverse channel to the stream-wise channel and the sudden increase of the cross-sectional area. However, based on the numerical results given in the figures below it is observed that the developing flow at the leading edge approaches a parabolic profile, that is in agreement with the plane Poiseuille velocity profile, within a fairly short entrance length.

Furthermore it is observed that an increase in the Reynolds number does not bring any major changes to the velocity profile. This observation may be due to the parabolic inlet flow assumed at the inlet of the computational domain. The stream-wise and transverse velocity vectors of porosity $\epsilon = 0.36$ are shown in Figure 5.4. The stream-wise velocity vectors also confirm the stream-wise velocity profile presented graphically, that the flow is developing at the beginning of the channel and finally attains the fully developed flow condition downstream.
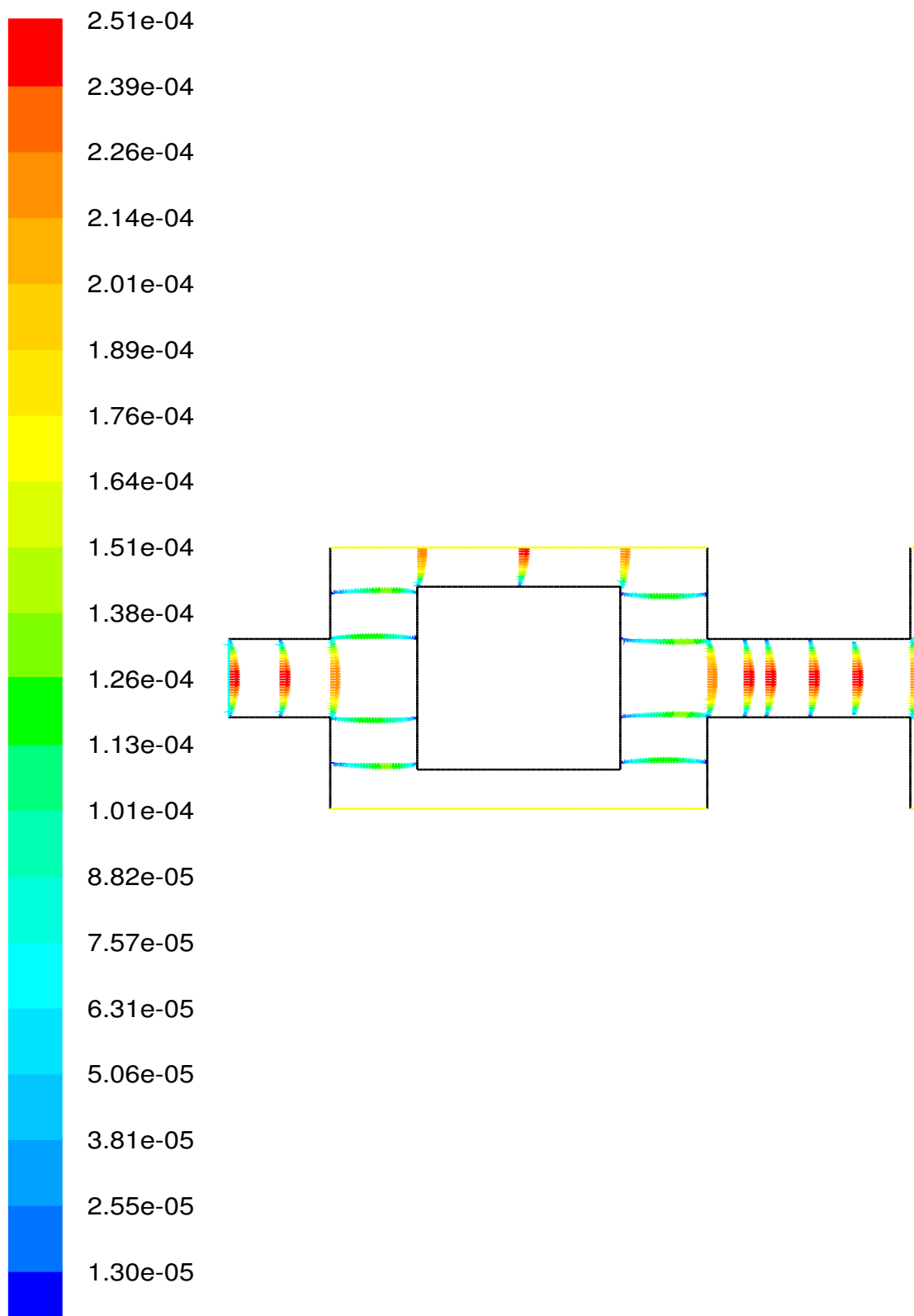
Figure 5.4: Predicted velocity vectors along the stream-wise and transverse channels of an RRUC.
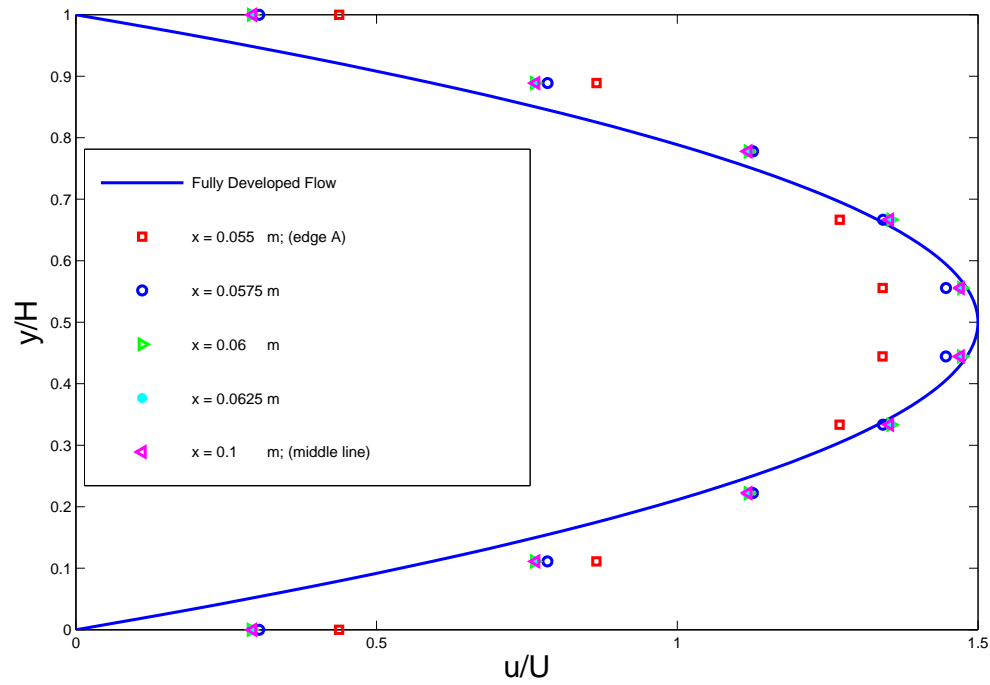
(a) $Re_{c_{\parallel}} = 5; \epsilon = 0.19$
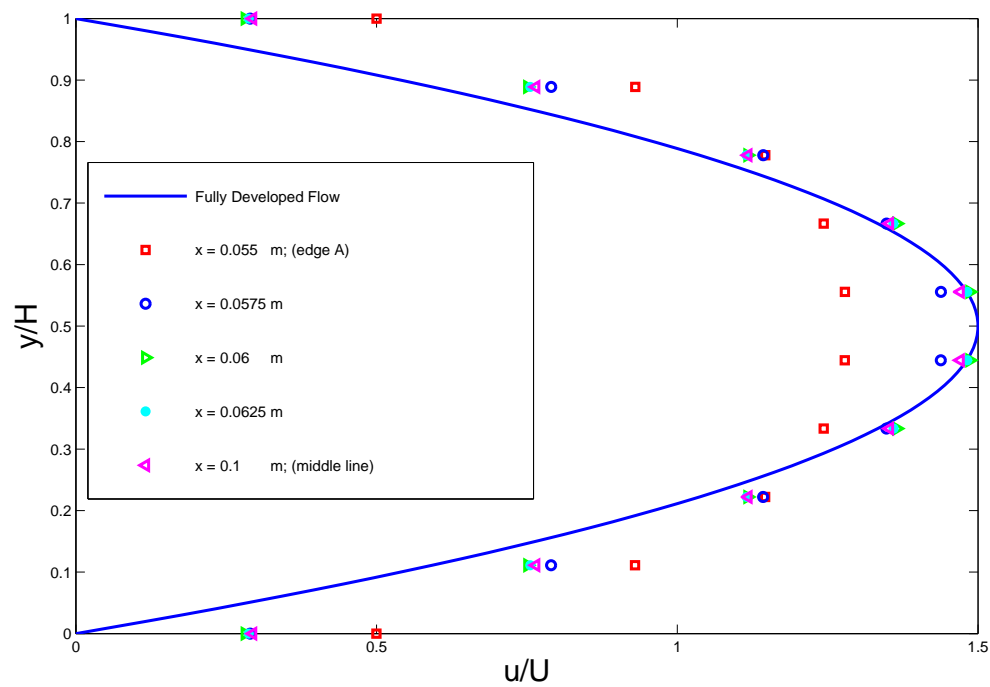
(b) $Re_{c_{\parallel}} = 30; \epsilon = 0.19$

Figure 5.5: The variation of the stream-wise velocity distribution at the entrance of the parallel surfaces (edge A) within the RRUC geometry for Case 1.
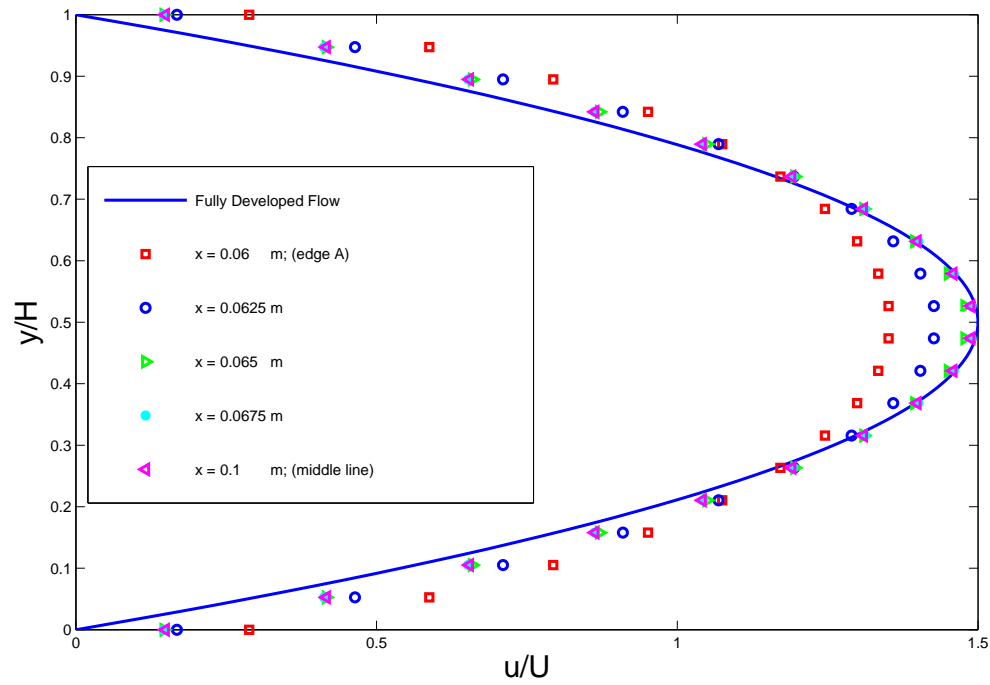
(a) $Re_{c_{\parallel}} = 5; \epsilon = 0.36$
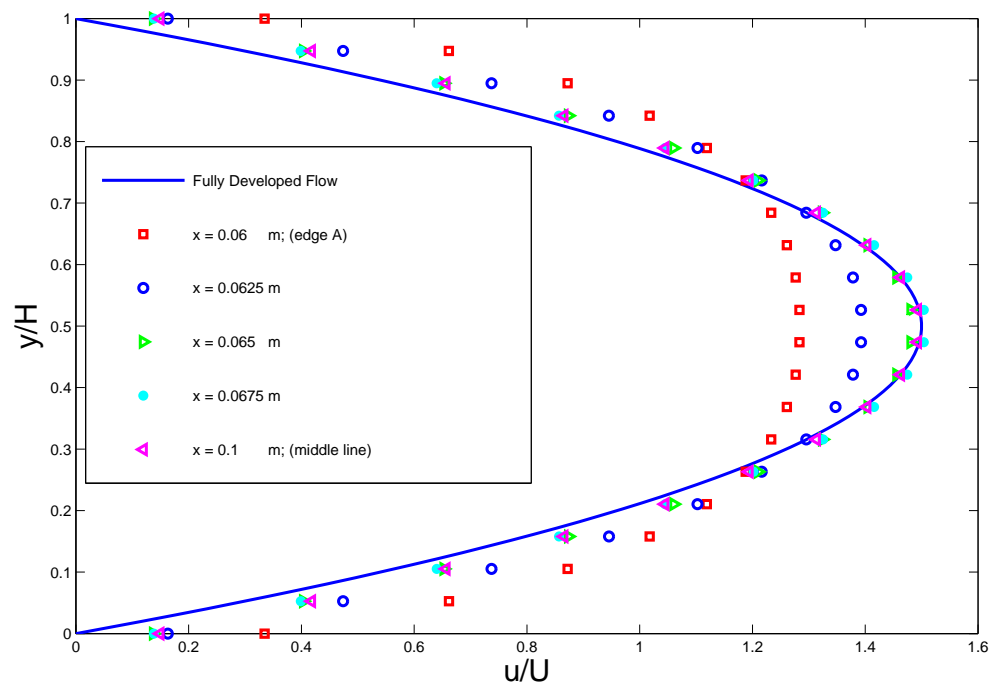
(b) $Re_{c_{\parallel}} = 30; \epsilon = 0.36$

Figure 5.6: The variation of the stream-wise velocity distribution at the entrance of the parallel surfaces (edge A) within the RRUC geometry for Case 2.

(a) $Re_{c_{\parallel}} = 5; \epsilon = 0.51$

(b) $Re_{c_{\parallel}} = 30; \epsilon = 0.51$

Figure 5.7: The variation of the stream-wise velocity distribution at the entrance of the parallel surfaces (edge A) within the RRUC geometry for Case 3.

(a) $Re_{c_{\parallel}} = 5; \epsilon = 0.64$

(b) $Re_{c_{\parallel}} = 30; \epsilon = 0.64$

Figure 5.8: The variation of the stream-wise velocity distribution at the entrance of the parallel surfaces (edge A) within the RRUC geometry for Case 4.

As pointed out earlier, in all four transverse channels present in the computational domain for all the porosities considered t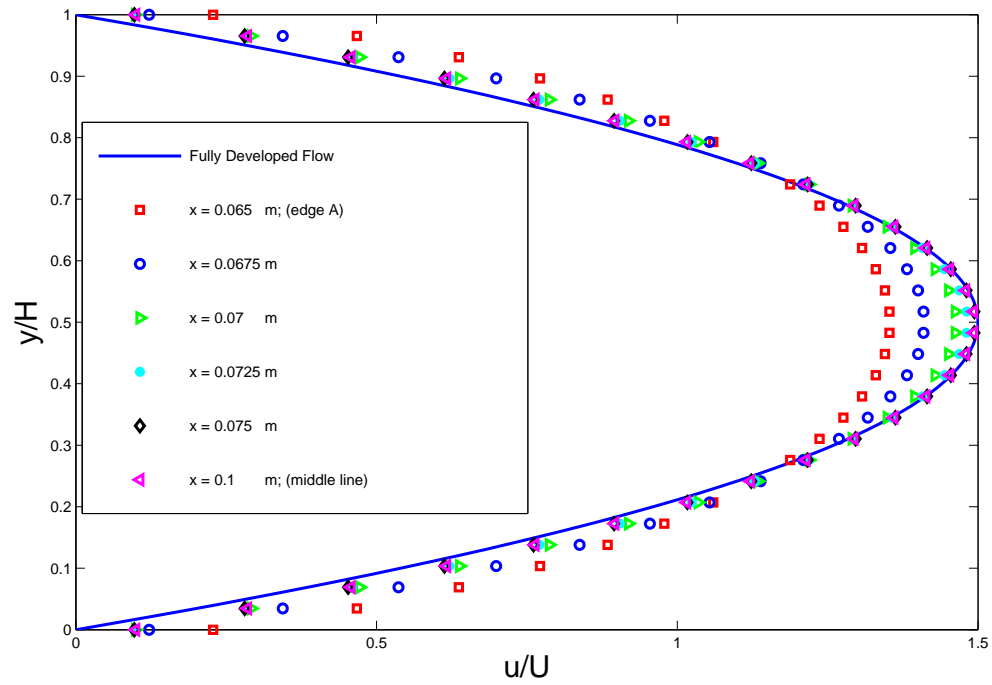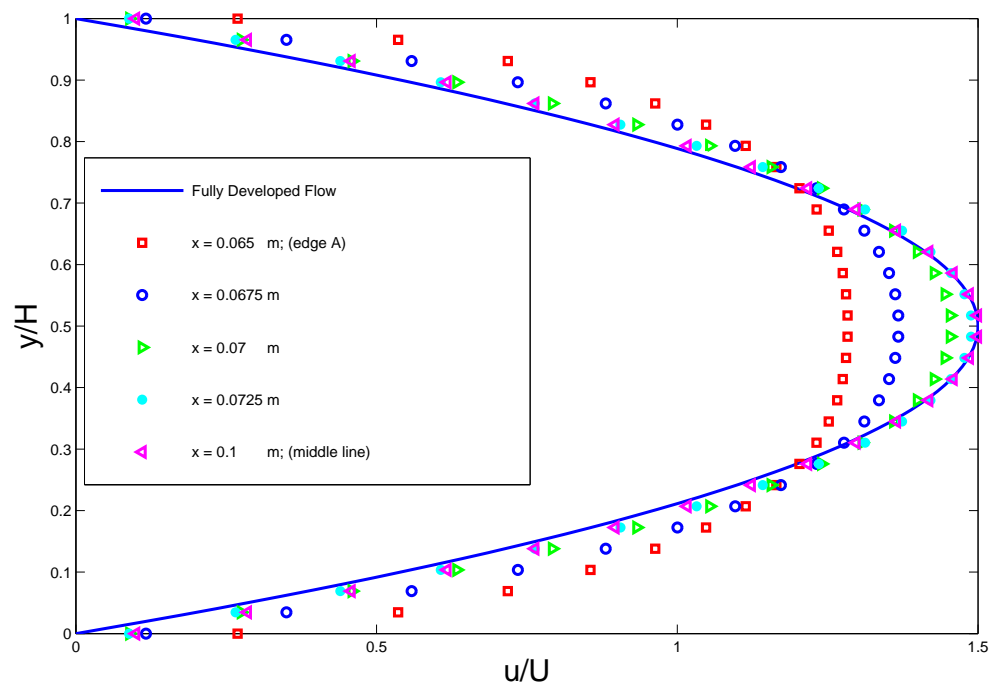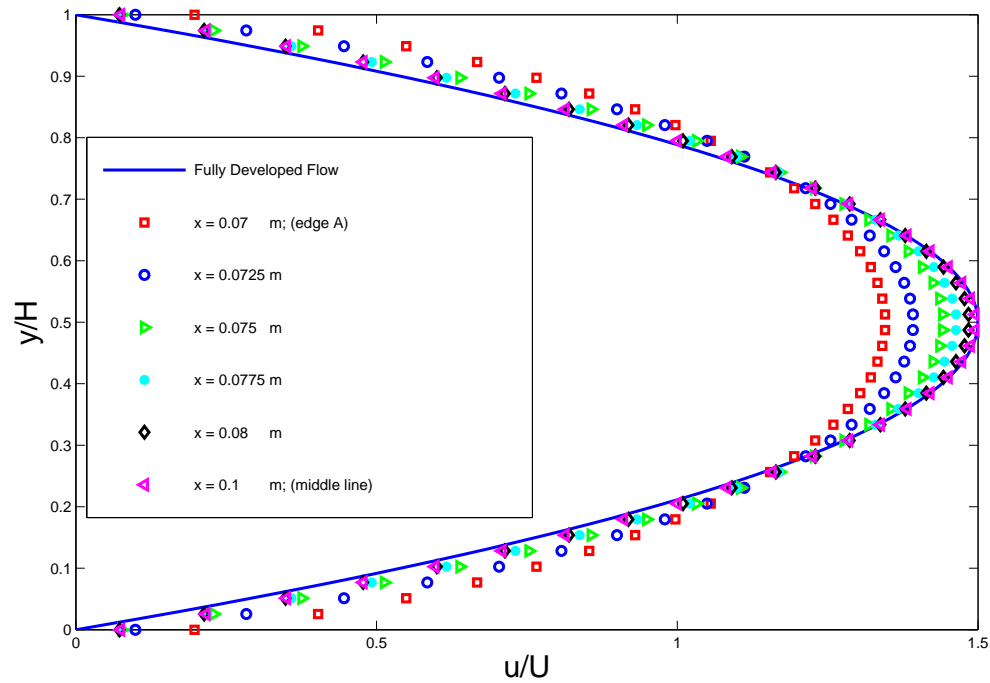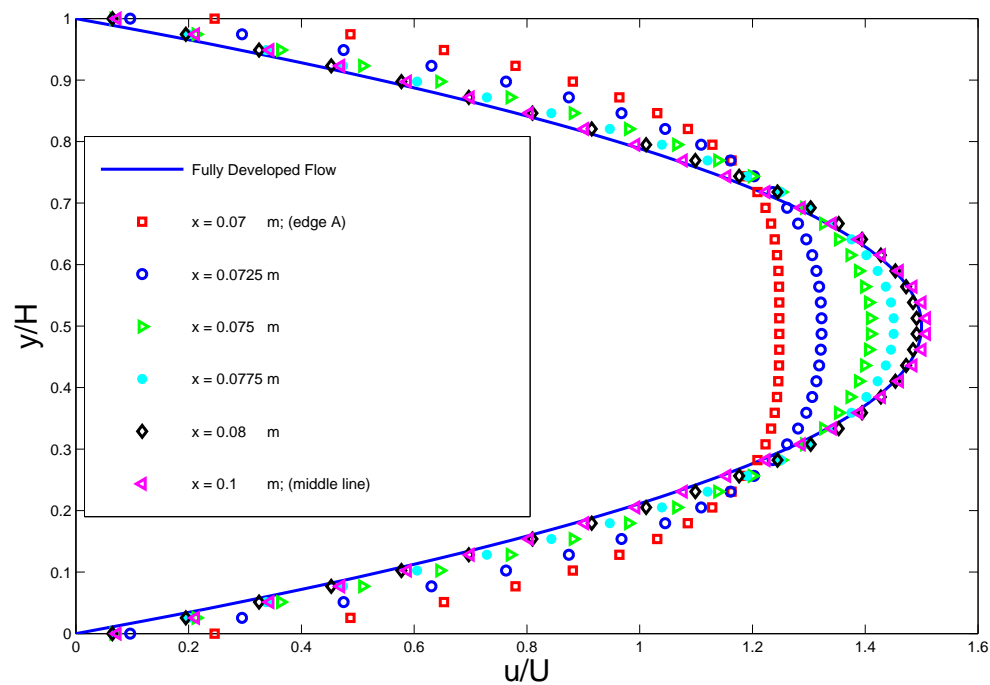he predicted velocity profile yield similar results at each location. Hence, the velocity predictions at several locations in the first transverse channel of the computational domain indicated by dotted lines 1 up to 4 in Figure 5.2 will be chosen for discussion.

If $w_\parallel$ and $w_\perp$ are the channel average velocities in the stream-wise volume, $U_\parallel$, and transverse volume, $U_\perp$, respectively, the RRUC model assumes the following relationship, $w_\perp = \beta w_\parallel$. In a case of a staggered geometry the stream-wise flux is split into two in the transverse channel and flux conservation yields:

$$w_\parallel \frac{d_\perp}{2} = w_\perp d_\parallel.$$
(5.4)

It then follows that

$$w_\perp = \frac{w_\parallel}{2} \frac{d_\perp}{d_\parallel},$$
(5.5)

where $\frac{d_\perp}{d_\parallel} = \alpha^*$ is an aspect ratio, which is equal to unity in this case. Therefore the value of $\beta = \frac{1}{2}$, and the analytical velocity profile will be adjusted accordingly for comparison with the transverse velocity profile.

The staggering level of the solid structure within the computational domain considered is a fully staggered array. This configuration forces the flow to bifurcate in opposite directions from the stream-wise channel into the transverse channel. Figures 5.9 to 5.13 show the axial velocity profile at locations mentioned above in the transverse channel of the computational geometries and they are plotted together with the plane Poiseuille flow velocity profile.

It is mentioned earlier that the flow enters the stream-wise channel at the periodic boundary of the computational domains with a parabolic velocity profile. However, Figure 5.9 shows a noticeable change in the velocity profile of Case 1 at $y = 0.005$ m (line 2) and $y = -0.005$ m (line 3) for both $Re_{c_\perp} = 2.5$ and 15. It can be seen that the flow enters the transverse channel with a skewed velocity profile as plotted in Figure 5.9. This is mainly due to the sudden change in the flow direction and the large mass flow rate from the stream-wise channel into the transverse channel. But as flow progresses in the channel, the axial velocity profile becomes almost parabolic and it shows a good agreement with the theoretical fully developed velocity profile.

The velocity profile for Case 2 yields the same flow pattern as in Case 1 for $Re_{c_\perp} = 2.5$, as illustrated in Figure 5.10 (a). Figure 5.10 (b) shows that an increase in the Reynolds number yield a different flow behaviour for Case 2. It is noticed that the location of the maximum velocity shifted slightly from the plane Poiseuille flow velocity profile, but it can be seen that the flow still has a parabolic profile.

The velocity distributions in the transverse channels for Cases 3 through 5 are shown in Figures 5.11 to 5.13 for $Re_{c_\perp} = 2.5$ and 15. It is observed that the velocity along the transverse channels deviate completely from the plane Poiseuille flow velocity profile. The visualization of the flow pattern in these figures reveals that, the fully developed plane Poiseuille flow assumption does not apply for flow between neighboring solid surfaces for high porosities. Velocity distribution for Case 6 through 8 (not plotted) exhibits similar flow behavior.

(a) $\epsilon = 0.19$; $Re_{c_\perp} = 5$
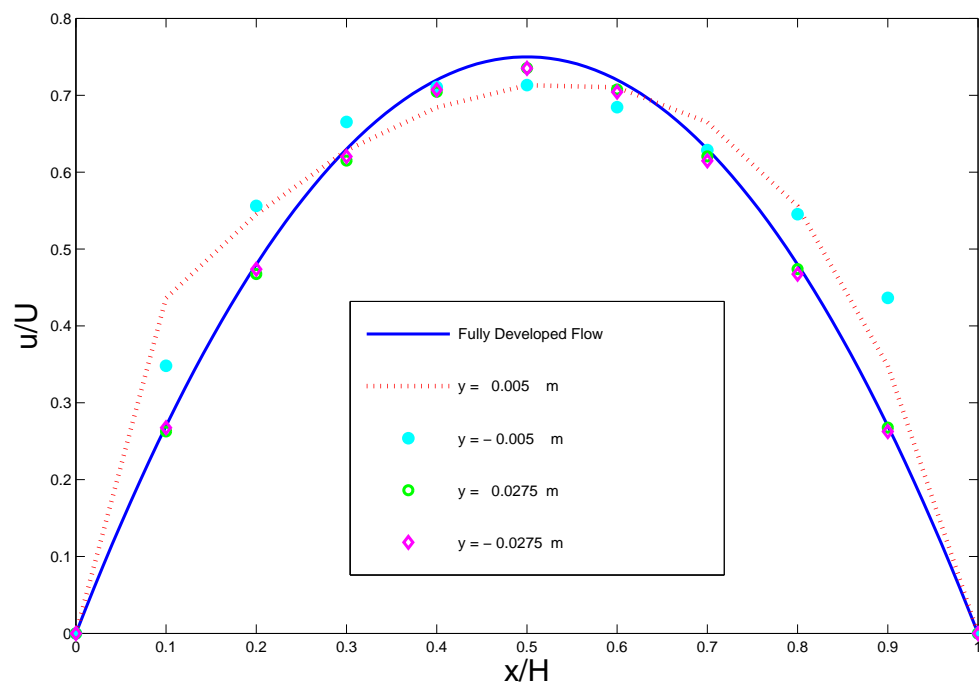
(b) $\epsilon = 0.19$; $Re_{c_\perp} = 30$

Figure 5.9: Comparison between predicted transverse velocity profiles at different locations with the analytical solution for Case 1.
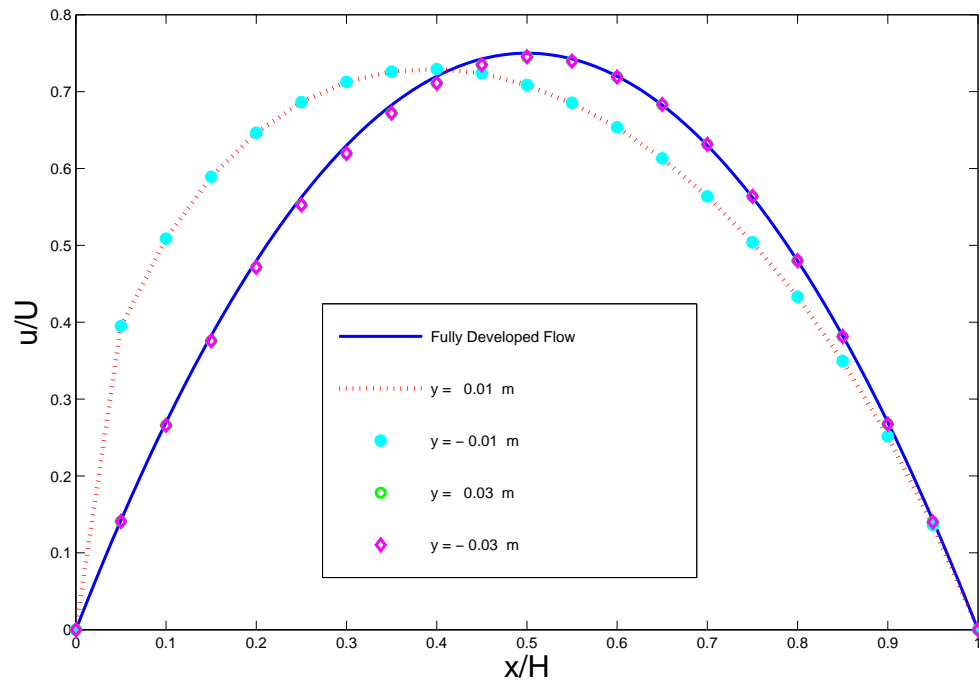
(a) $\epsilon = 0.36$; $Re_{c_\perp} = 5$
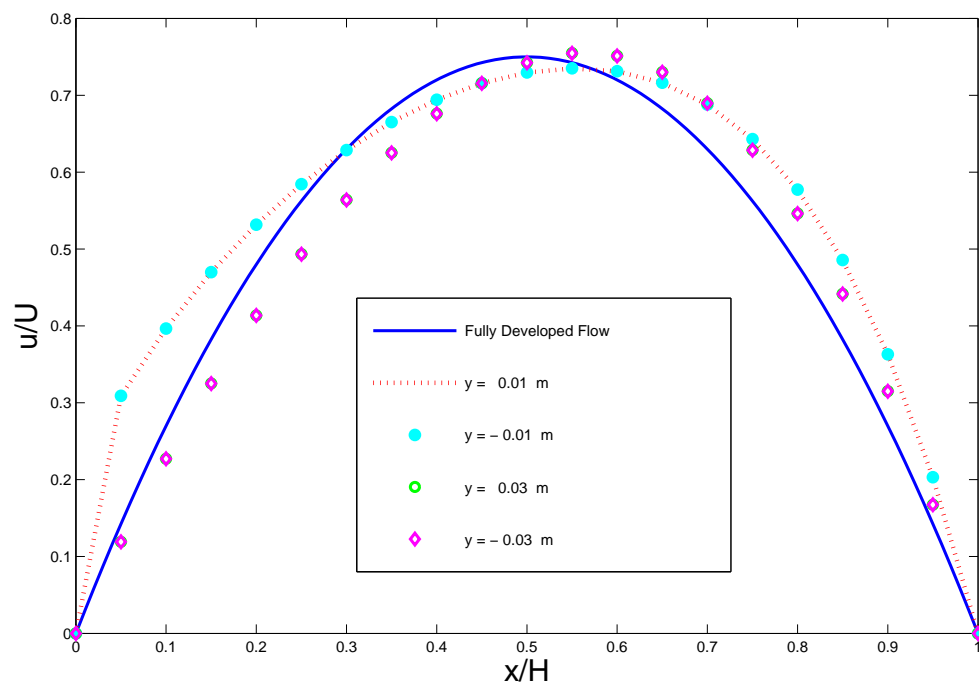
(b) $\epsilon = 0.36$; $Re_{c_\perp} = 30$

Figure 5.10: Comparison between predicted transverse velocity profiles at different locations with the analytical solution for Case 2.
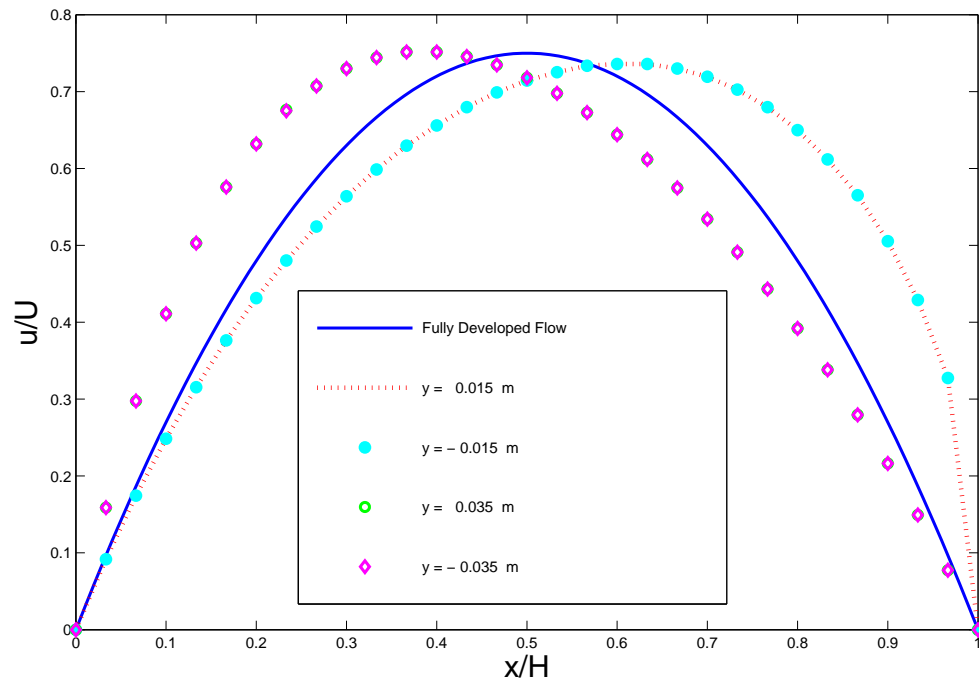
(a) $\epsilon = 0.51$; $Re_{c_\perp} = 5$
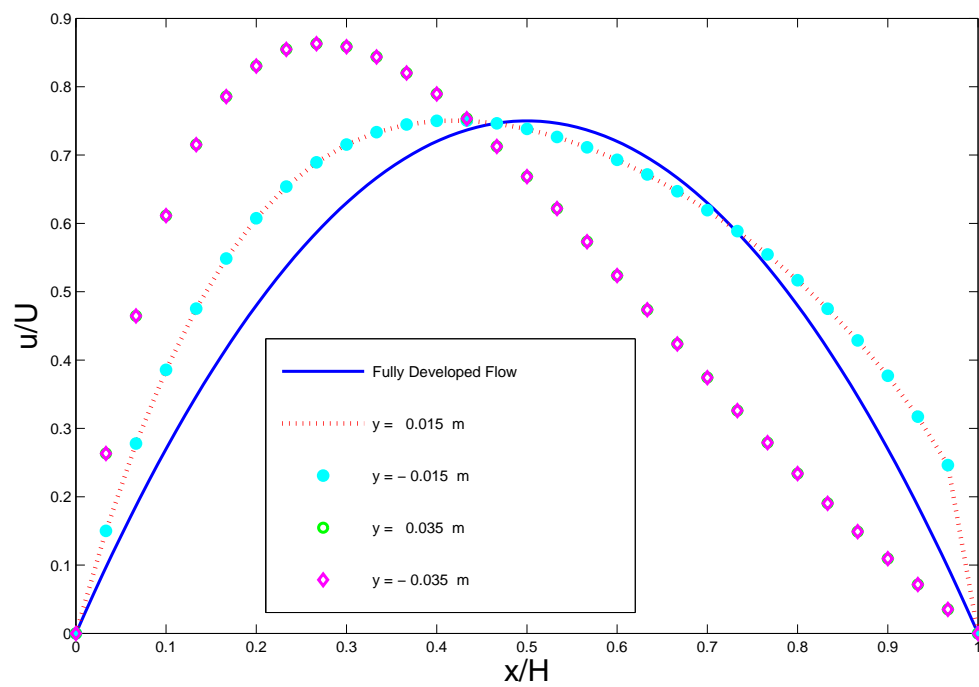
(b) $\epsilon = 0.51$; $Re_{c_\perp} = 30$

Figure 5.11: Comparison between predicted transverse velocity profiles at different locations with the analytical solution for Case 3.

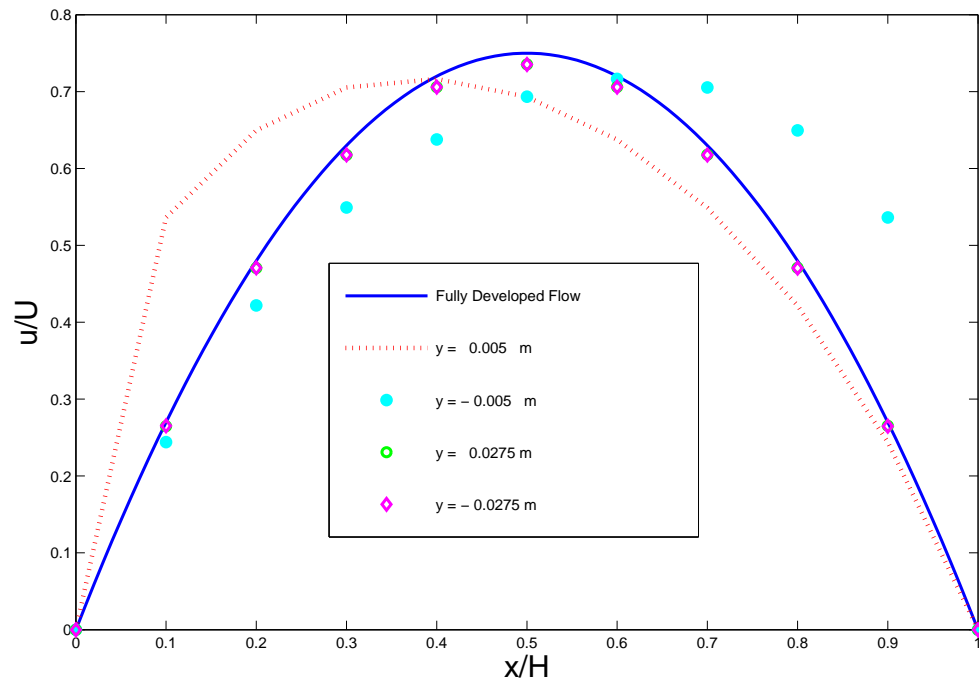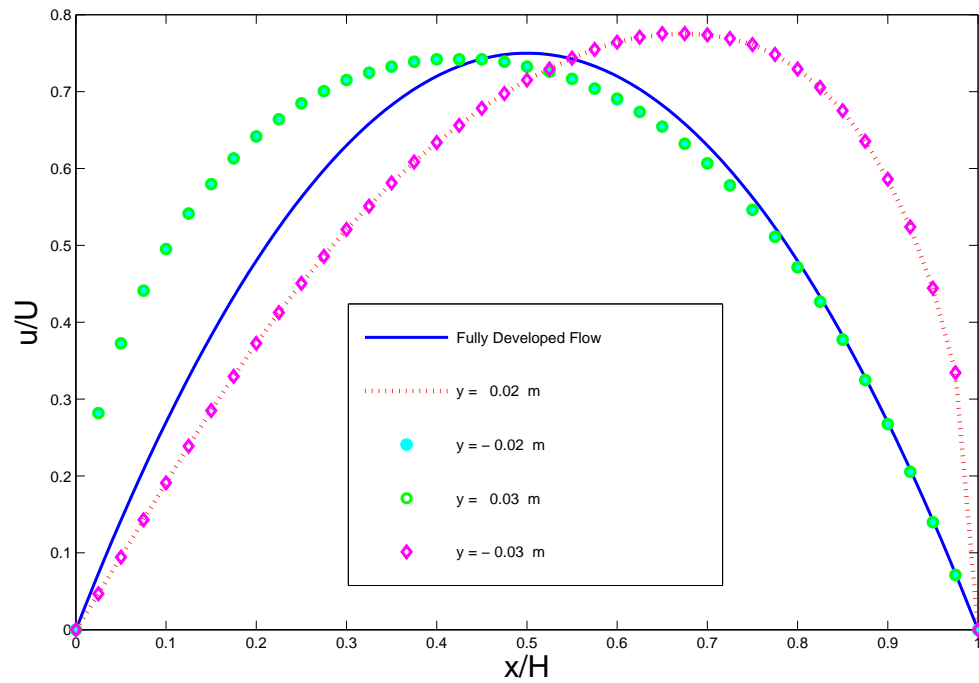(a) $\epsilon = 0.64$; $Re_{c_\perp} = 5$
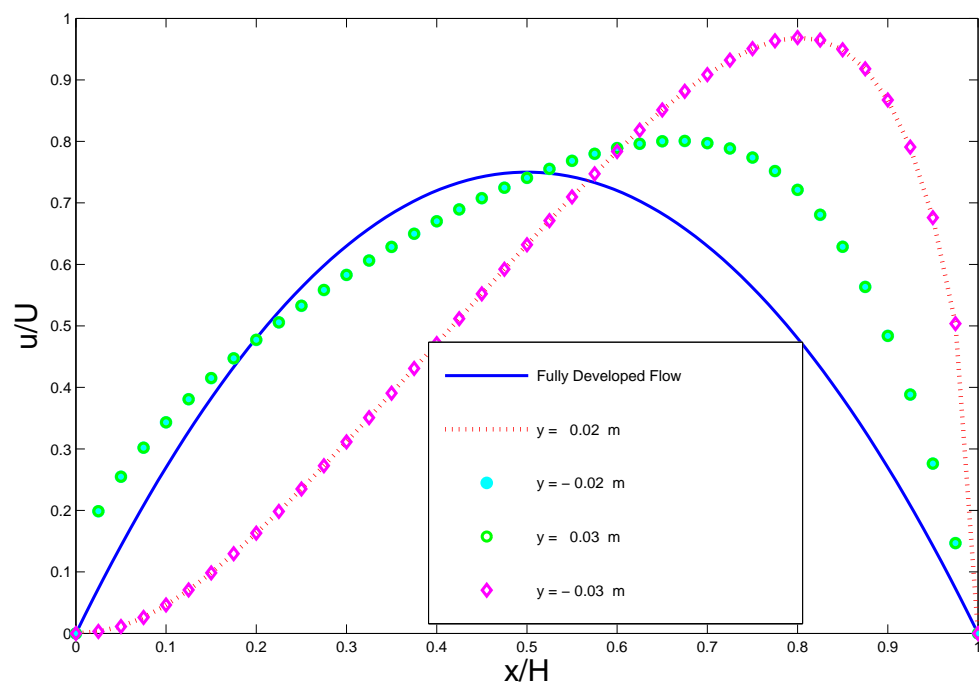
(b) $\epsilon = 0.64$; $Re_{c_\perp} = 30$

Figure 5.12: Comparison between predicted transverse velocity profiles at different locations with the analytical solution for Case 4.
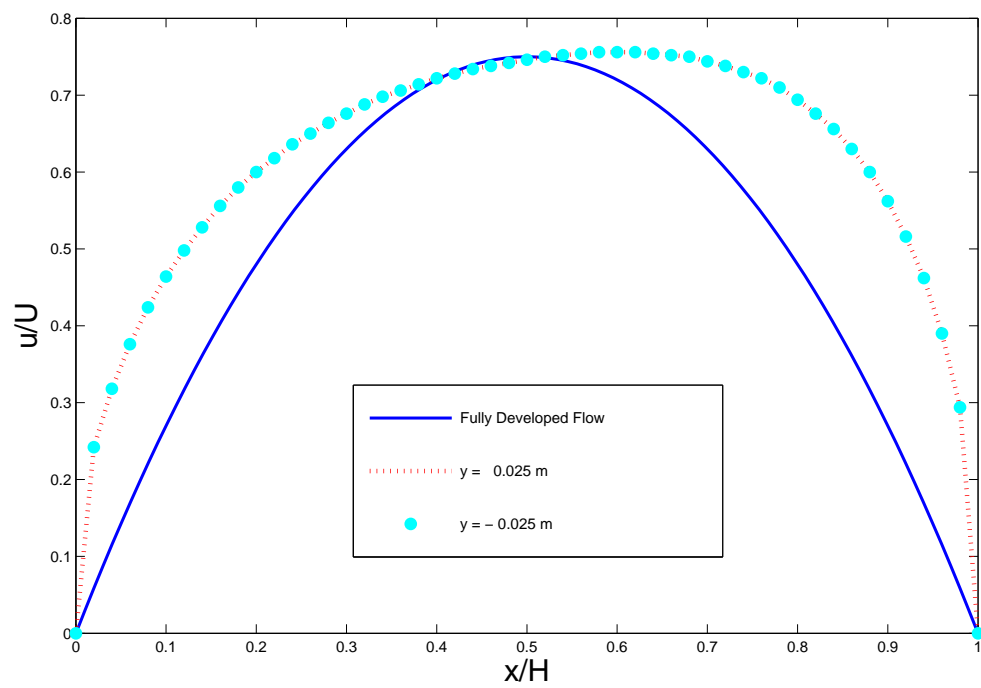
(a) $\epsilon = 0.75 \, ; Re_{c_\perp} = 5$

Figure 5.13: Comparison between predicted transverse velocity profiles at different locations with the analytical solution for Case 5.

Figure 5.14 shows the pattern of the flow, presented by the velocity path lines around the solid structure within the computational domain. A steady flow symmetrically circulating around the solid structure within the computational domain of porosity 0.75 is observed in Figure 5.14 at $Re_{c_\parallel} = 10$. As the Reynolds increases, $Re_{c_\parallel} \geq 30$, Figure 5.15 reveals the presence of small recirculations around the solid structure within the geometry. Du Plessis (1994) mentioned that the recirculation zone are caused by the prevailing inertial effects.

It is worth mentioning that the simulations for Case 1 through 8, were conducted with various Reynolds number up to $Re_{c_\parallel} = 40$. This observation of flow recirculations started to occur for a computational model of porosity 0.75 at approximately $Re_{c_\parallel} = 30$. It must be kept in mind that the level of porosity also have an effect on the flow. This particular flow behaviour resembles flow over a square cylinder and it probably contributes greatly to the deviation of the prediction of the theoretical model from the numerical results at high porosities. The numerical results are further analyzed to determine the wall shear stresses along the fluid-solid interfaces in the stream-wise and transverse channels.
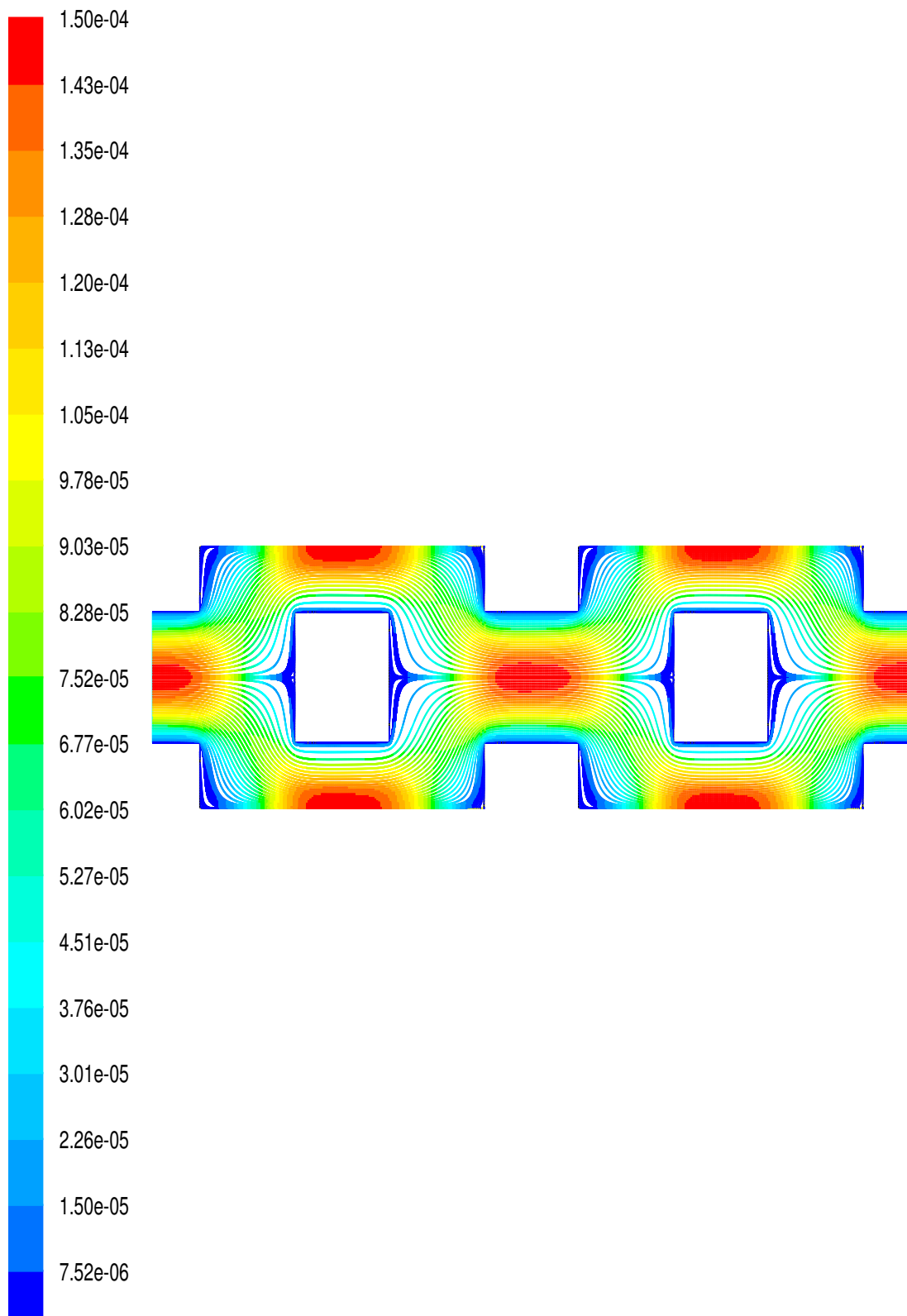
Figure 5.14: Velocity path lines in the computational domain, $Re_{c_\parallel} = 10$ and $\epsilon = 0.75$.
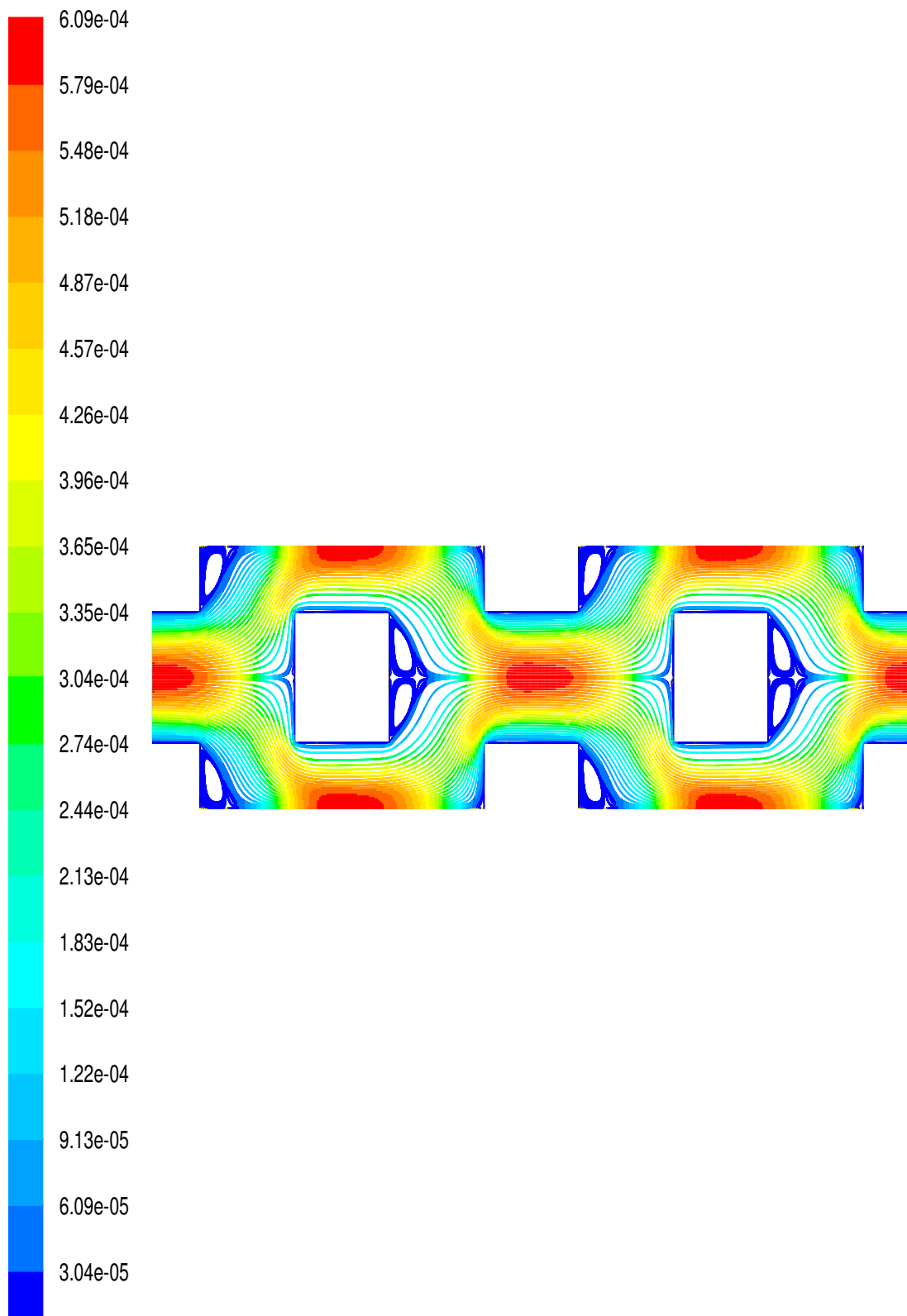
Figure 5.15: Velocity path lines in the computational domain, $Re_{c_\parallel} = 30$ and $\epsilon = 0.75$.

5.2.2   Wall Shear Stress τ_w

As mentioned previously plane Poiseuille flow is assumed in the pore sections of the porous media and constant wall shear stresses

$$\tau_{w_\parallel} = \frac{6\mu w_\parallel}{d_{c_\perp}} \quad \text{and} \quad \tau_{w_\perp} = \frac{6\mu w_\perp}{d_{c_\parallel}}, \tag{5.6}$$

are therefore assumed to exist throughout the stream-wise and transverse fluid-solid interface, respectively. The wall shear stress on the stream-wise and transverse fluid-solid interfaces, corresponding to the plane Poiseuille flow will be denoted respectively by $(\tau_{w_\parallel})_{\text{theory}}$ and $(\tau_{w_\perp})_{\text{theory}}$. The magnitude of the numerical wall shear stress depends on both the stream-wise and transverse channel configurations and they will be denoted by $(\tau_{w_\parallel})_{\text{num}}$ and $(\tau_{w_\perp})_{\text{num}}$, respectively.

The numerical dimensional wall shear stress on the stream-wise fluid-solid interface is plotted against the axial distance x from the leading edge A to the trailing edge B of the channel considered. On the same axis, the wall shear stress corresponding to the stream-wise plane Poiseuille flow [equation (5.6)] is also plotted together with the predicted constant wall shear stress obtained from the simulation of the flow between the uninterrupted parallel plates. This constant value is the predicted value of fully developed flow. For the uninterrupted parallel plate model simulation, the channel width between the parallel plates was chosen to match the stream-wise channel width $d_{c_\perp}$ of the RRUC computational domain and the simulations were run similarly as in Chapter 4.

Du Plessis & Collins (1992) used the plane Poiseuille flow Fanning friction factor $fRe = 24$ in equation (4.24), to obtain a new proposed hydrodynamic entrance length $x_c^+ = 0.0205$. To obtain an apparent friction factor independent of the axial position, Du Plessis & Collins (1992) substituted the proposed entrance length in equation (4.16) and the following constant value was obtained,

$$(f_{app}Re)_c = 32.1. \tag{5.7}$$

The Fanning friction factor formula was used to determine the wall shear stress τ_w corresponding to equation (5.7). The results will also be plotted on the same axis with other graphs already mentioned above, in order to determine if the results obtained by Du Plessis & Collins (1992) do not give a better estimation than equation (5.6) for average τ_w.

The stream-wise wall shear stress $\tau_{w_\parallel}$, obtained from simulations of Case 1 through Case 8 will be presented graphically for only two Reynolds numbers, i.e, $Re_{c_\parallel} = 5$ and 30. The transverse wall shear stress $\tau_{w_\perp}$ will also be discussed for Cases 1 and 2 at $Re_{c_\perp} = 2.5$ and 15, and Case 3 for only $Re_{c_\perp} = 2.5$ due to the deviation of the flow profile from fully developed as porosity increases.

The percentage error calculated as the percentage of the difference between the theoretical fully developed flow wall shear stress, $(\tau_w)_{\text{theory}}$, and the numerical predicted fully developed flow wall shear stress $(\tau_w)_{\text{num}}$, will be used to obtained the percentage error of the simulation results. The percentage error is presented mathematically as follows:

$$\text{Percentage error} = \frac{(\tau_w)_{\text{theory}} - (\tau_w)_{\text{num}}}{(\tau_w)_{\text{theory}}} \times 100. \tag{5.8}$$

Figures 5.16 through 5.20 show a good agreement between the fully developed flow wall shear stress $(\tau_{w_\parallel})_{\text{num}}$, obtained from the computations of the flow between the uninterrupted parallel plates and the plane Poiseuille flow wall shear stress $(\tau_{w_\parallel})_{\text{theory}}$. The numerical solution for the wall shear stress on the parallel surfaces under investigation, shows that at any instant of time there exist three flow regimes in this channel, namely: an entrance region (edge A), a fully developed flow regime and an exit region (edge B). The existence of the entrance and exit region is due to the sharp corners at the leading edge A and B that lead to sudden change of flow direction.

Following the sudden pressure drop at the entrance region (edge A), the predicted stream-wise wall shear stress $(\tau_{w_\parallel})_{\text{num}}$ for Case 1 at $Re_{c_\parallel} = 5$ decreases asymptotically from the maximum value almost immediately downstream and becomes independent of the axial distance, as depicted in Figure 5.16 (a). An increase in the predicted $(\tau_{w_\parallel})_{\text{num}}$ at the exit region (edge B) is observed, [Figure 5.16]. It should be noted that the drastic increase in the value of the predicted wall shear stress at either end of the parallel surfaces is owing to the change of flow direction from the stream-wise into the transverse channel, with the entrance effect being predominant. The fully developed flow $(\tau_{w_\parallel})_{\text{num}}$ in Case 1 for $Re_{c_\parallel} = 5$ under-predicted the plane Poiseuille flow wall shear stress $(\tau_{w_\parallel})_{\text{num}}$ by 1.7%.

The results of computation shown in Figure 5.16 (b) are qualitatively identical with data in Figure 5.16 (a) revealing, however, one noticeable difference downstream of the entrance region. The plot clearly shows that as $Re_{c_\parallel}$ increases, the entrance effect is dominant, leading to an extension of the length to reach an axial independent wall shear stress. The $(\tau_{w_\parallel})_{\text{num}}$ in this case, also under predicted the analytical wall shear stress by 1.25%. Figure 5.17 also shows similar stream-wise wall shear stress distribution as in Figure 5.16.

The numerical results for fully developed flow, for Cases 3 through 5 and for each case of the flow between the uninterrupted parallel plates are shown in Figures 5.18 through 5.20 to be in excellent agreement with the analytical solution. However, the comparison of the predicted $(\tau_{w_\parallel})_{\mathrm{num}}$ for Case 5 at $Re_{c_\parallel} = 30$ with $(\tau_{w_\parallel})_{\mathrm{theory}}$ in Figure 5.20 (b) reveals that due to the short lengths of the streamwise channel as porosity increases, the flow is not quite fully developed and the entire flow length is in the developing flow region. The flow deviation from the fully developed flow for this particular Re and higher Reynolds numbers may also be due to the fact that the hydrodynamic entrance length increases linearly with the Reynolds number. It should also be noted that this is the case where the flow recirculation started to show.

This deviation extends to even higher porosities (Cases 6 through 8). Figure 5.20 to 5.21 demonstrates the discrepancy in the flow behaviour as the porosity increases. These results are to be expected since as explained in the case of the velocity profile that at higher porosities the neighboring solid materials within the computational domain become far apart from each other. This geometry as porosity increases deviates from the assumption made in the development of the RRUC model, [Du Plessis (1994)], of neighboring solid materials forming parallel surfaces. However, for the high porosity case as depicted in Figure 5.22 it seems that the wall shear stress according to Du Plessis & Collins (1992) gives a better representation when compared to the numerical wall shear stress.
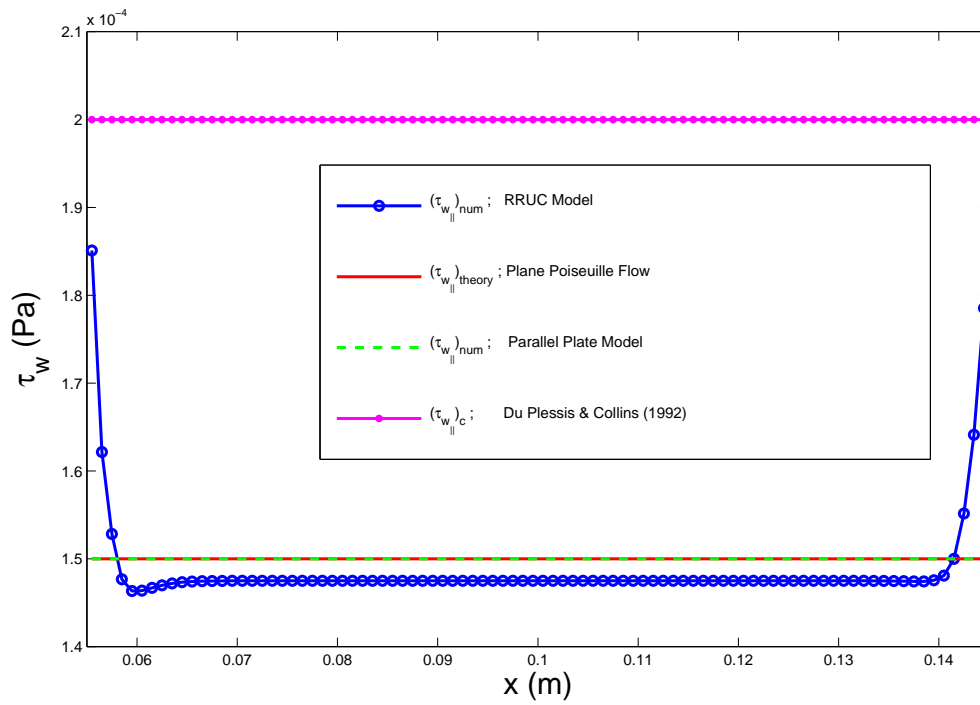
(a) $\epsilon = 0.19$; $Re_{c_{\parallel}} = 5$
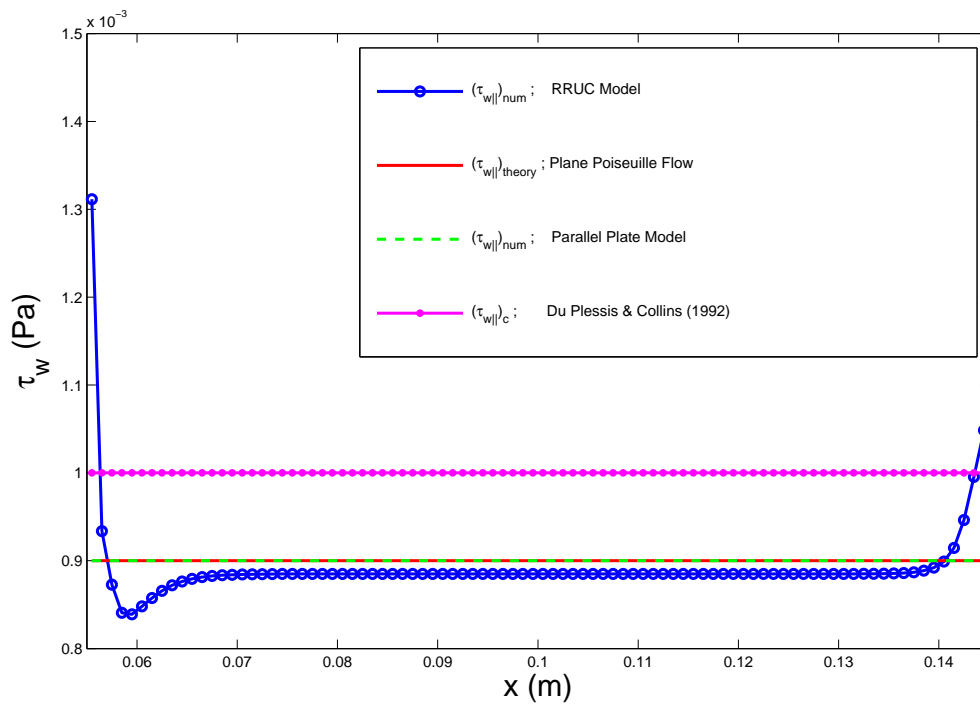
(b) $\epsilon = 0.19$; $Re_{c_{\parallel}} = 30$

Figure 5.16: Dimensional stream-wise wall shear stress $\tau_{w_{\parallel}}$ as a function of axial distance x for Case 1.
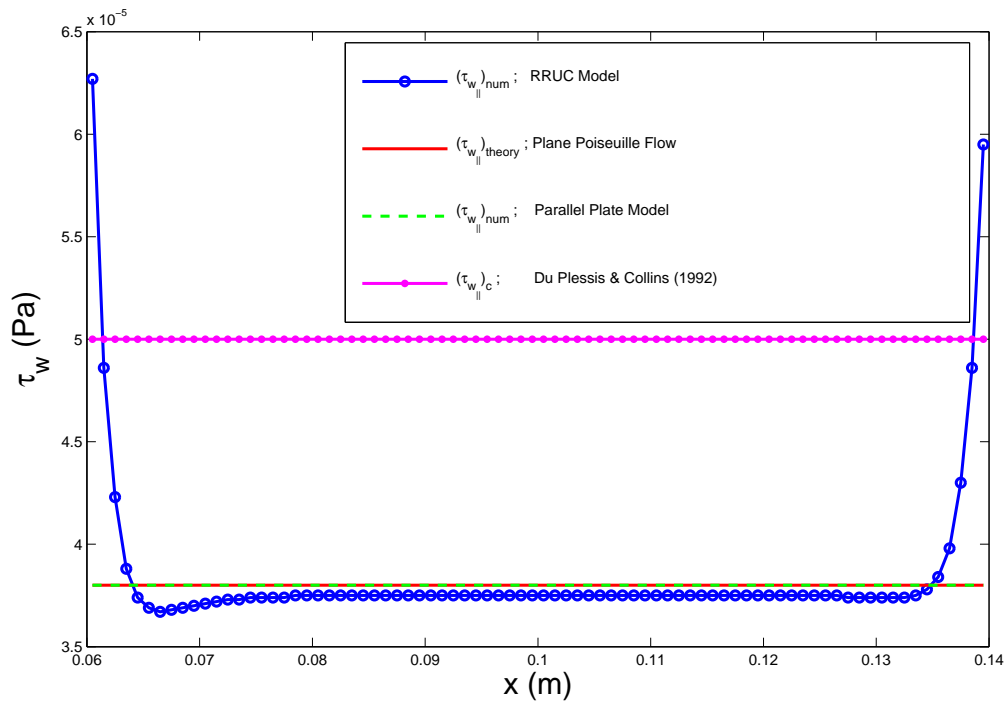
(a) $\epsilon = 0.36$; $Re_{c_\parallel} = 5$
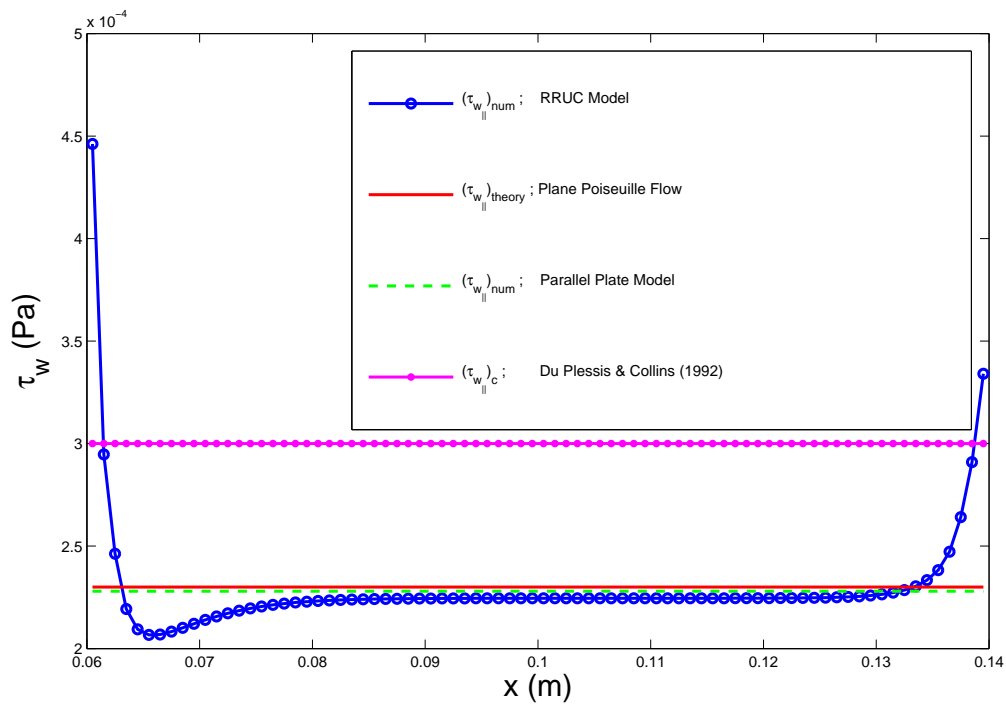
(b) $\epsilon = 0.36$; $Re_{c_\parallel} = 30$

Figure 5.17: Dimensional stream-wise wall shear stress $\tau_{w_\parallel}$ as a function of axial distance x for Case 2.
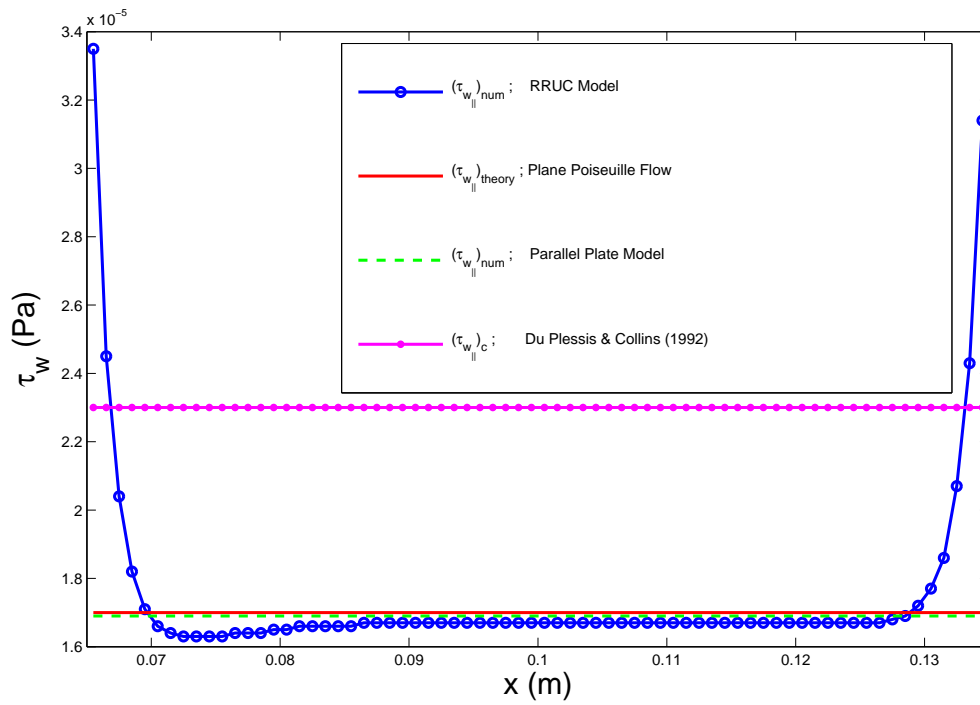
(a) $\epsilon = 0.51$; $Re_{c_\parallel} = 5$
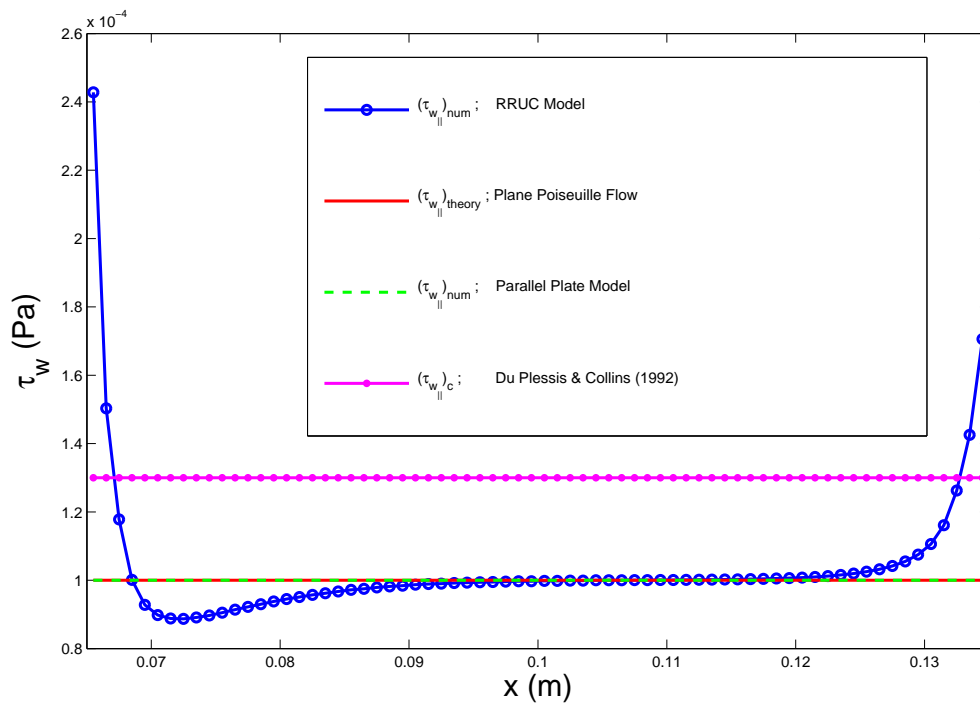
(b) $\epsilon = 0.51$; $Re_{c_\parallel} = 30$

Figure 5.18: Dimensional stream-wise wall shear stress $\tau_{w_\parallel}$ as a function of axial distance x for Case 3.
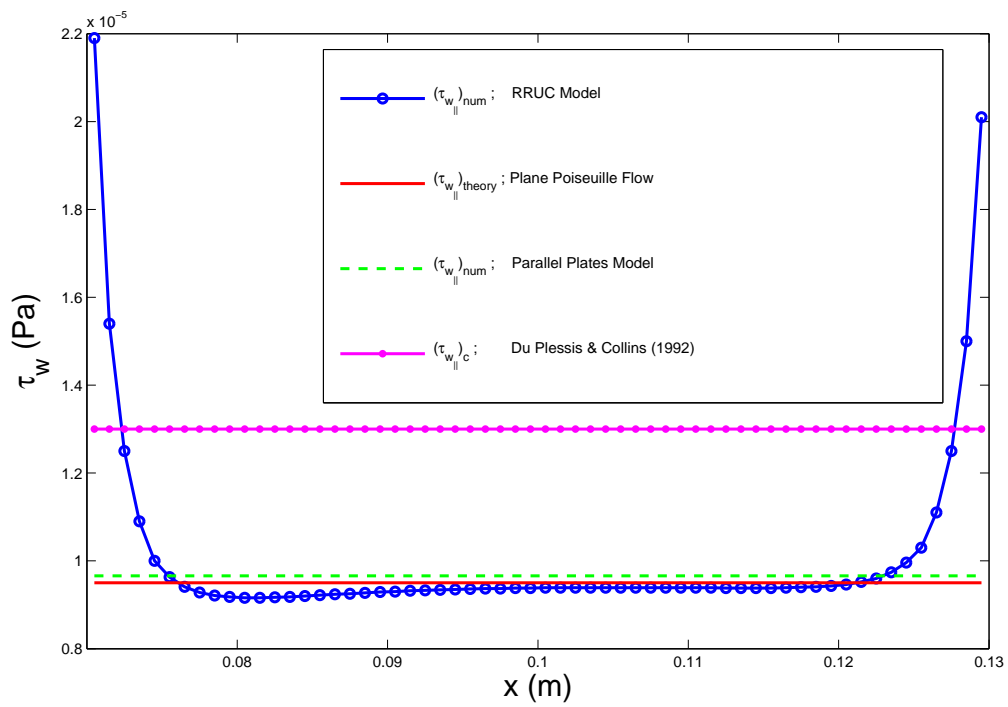
(a) $\epsilon = 0.64 \, ; Re_{c_{\parallel}} = 5$
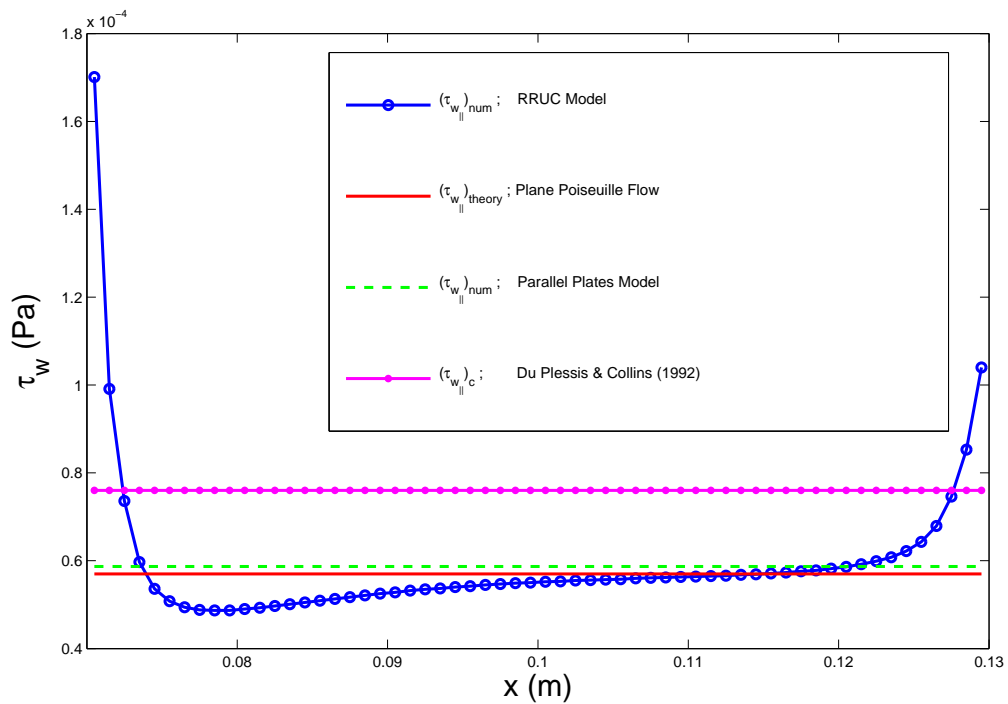
(b) $\epsilon = 0.64 \, ; Re_{c_{\parallel}} = 30$

Figure 5.19: Dimensional stream-wise wall shear stress $\tau_{w_{\parallel}}$ as a function of axial distance x for Case 4.
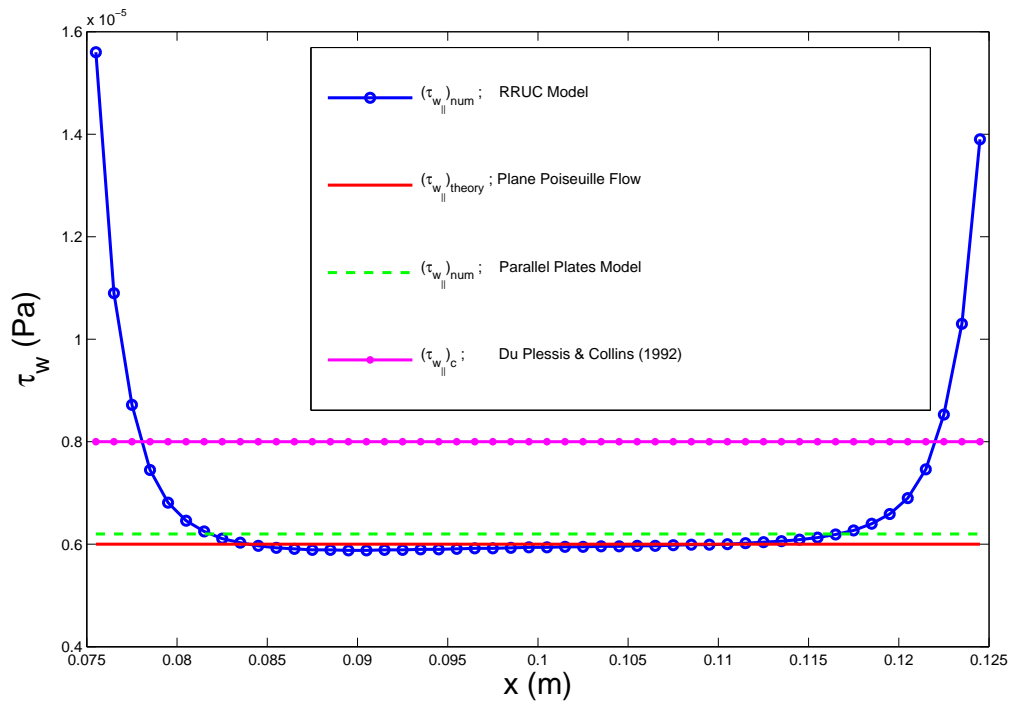
(a) $\epsilon = 0.75$; $Re_{c_{\parallel}} = 5$
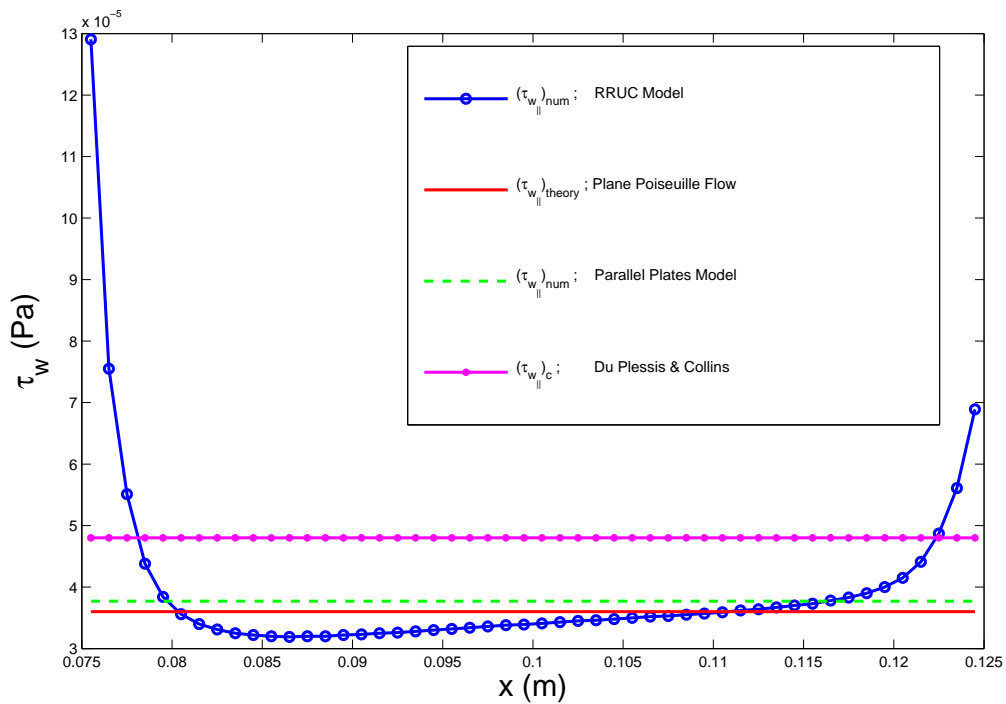
(b) $\epsilon = 0.75$; $Re_{c_{\parallel}} = 30$

Figure 5.20: Dimensional stream-wise wall shear stress $\tau_{w_{\parallel}}$ as a function of axial distance x for Case 5.
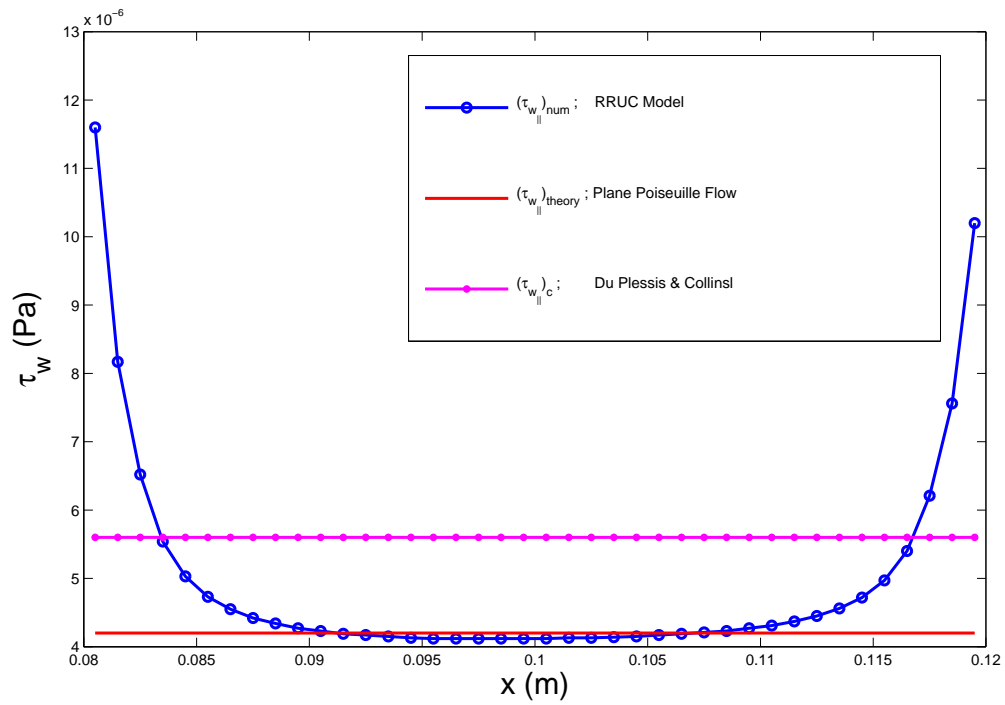
(a) $\epsilon = 0.84$; $Re_{c_\parallel} = 5$
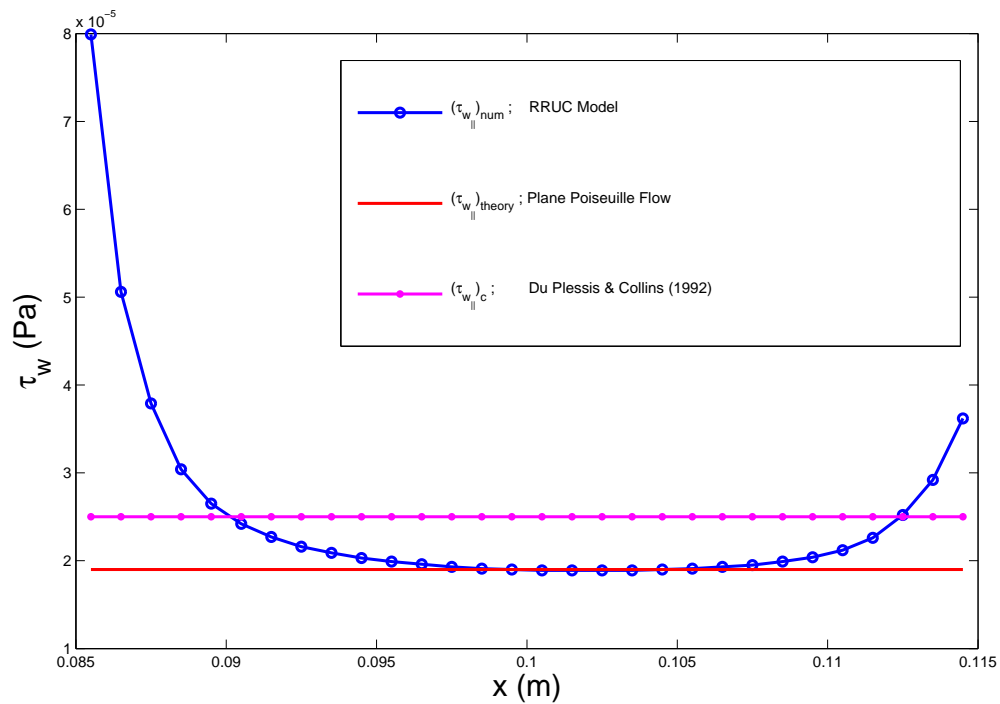
(b) $\epsilon = 0.91$; $Re_{c_\parallel} = 30$

Figure 5.21: Dimensional stream-wise wall shear stress $\tau_{w_\parallel}$ as a function of axial distance x for Case 6 and Case 7.
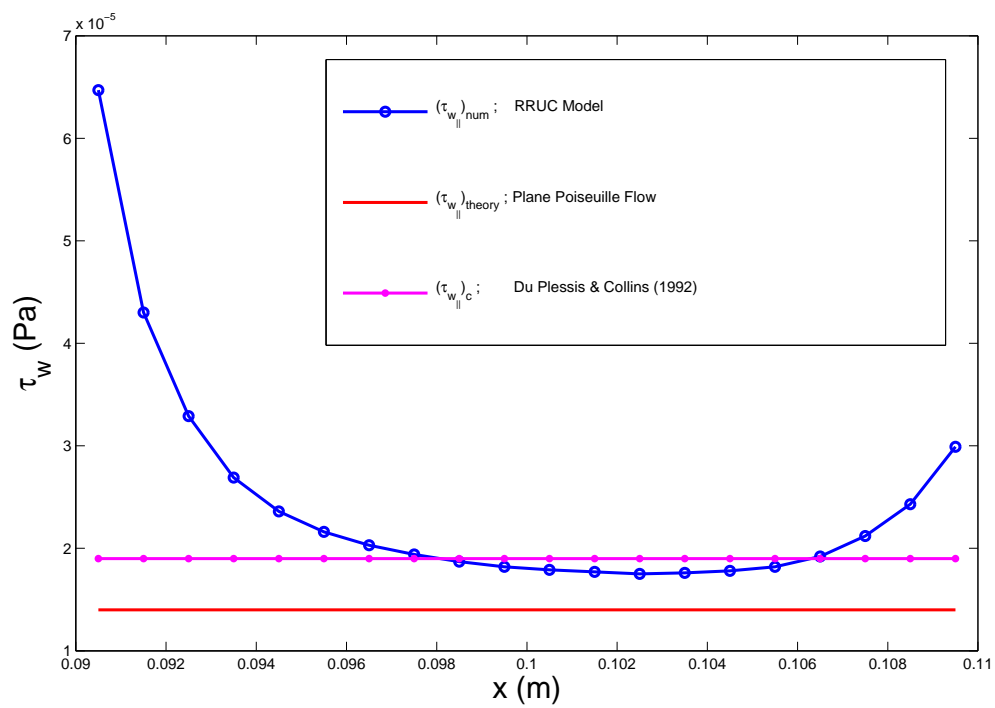
(a) $\epsilon = 0.96$; $Re_{c_{\parallel}} = 30$

Figure 5.22: Dimensional stream-wise wall shear stress $\tau_{w_{\parallel}}$ as a function of axial distance x for Case 8.

The wall shear stress in the transverse channels will be analyzed similarly to the stream-wise channels except that the three RRUC models mentioned previously have different regions where the wall shear stress is constant in the transverse channels. Model 1 [Diedericks (1999)], divided the fluid volume into two sub-volume, the stream-wise volume $U_{\parallel}$ and transverse volume $U_{\perp}$ [Figure 2.2 (a)], and a constant wall shear stress is assumed to prevail on the entire fluid-solid interface of these sub-volumes.

The other two models, [Lloyd et al. (2004) and Cloete & Du Plessis (2006)], treated the fluid volume as three different volumes $U_{\parallel}$, $U_{\perp}$ and the transfer volume U_t. It is shown in Figure 2.2 (b) and (c) that the transfer volumes of the two models are different. The transfer volume defined by Model 2, [Lloyd et al. (2004)], does not consist of any solid interfaces as illustrated in Figure 2.2 (b), hence for this model the transfer volume just acts as a transfer volume for fluid and the pressure drop is assumed to be zero in this volume. Therefore for Model 2 a constant wall shear stress also exists along the entire fluid-solid interface as in Model 1.

Model 3, [Cloete & Du Plessis (2006)] has a different scenario from the other two models as also depicted in Figure 2.2 (c). Model 3 suggests that the constant wall shear stress exists only on sections of the fluid-solid interface not occupied by the transfer volume. Model 3 neglected the wall shear stresses acting on the solid-interfaces in the transfer volume and further assumed that the pressure drop is zero there.

Figures 5.23 through 5.25 show the transverse wall shear stress on the wall opposite the stream-wise channel. The most notable phenomenon in Figure 5.23 (a), is variation of the wall shear stress along the fluid-solid interface in the transverse channel. However it is also observed in the same graph that in the farther transverse distance exceeding the dimensions of the middle section of the wall, the wall shear stress $(\tau_{w_{\perp}})_{\text{num}}$ is practically constant. The constant $(\tau_{w_{\perp}})_{\text{num}}$ observed on a portion of the transverse wall is a convincing evidence of the fully developed flow.

It is also demonstrated that under the same flow rate the wall shear stresses at the middle of the wall, where there is no parallel plates, are less than the constant value expected from the plane Poiseuille flow wall shear stress [equation (5.6)]. The numerical wall shear stress at $-0.04\ m\ <y>\ 0.04\ m$ of the transverse wall underestimated the plane Poiseuille flow value by up to 67% [Figure 5.23 (a)]. At the trailing edges of the walls the flow yields a different flow profile from the plane Poiseuille flow, very high values of the $(\tau_{w_{\perp}})_{\text{num}}$ are observed with a difference of up to 100%. This is due to velocity gradients experienced by the flow at these points.

At $\epsilon = 0.36$, the difference, at the section mentioned above, between the numerical values and the expected analytical values starts to increase to up to 83%, and this difference will definitely be higher for higher porosities. The deviation from the plane Poiseuille flow between the transverse channels is increasing as the porosity increases as illustrated in Figures 5.24 and 5.25. This is due to the fact that as the porosity increases, the length of the perpendicular solid-fluid interface $d_{s_\perp}$ decreases and as a result the flow is not taking place between parallel plates anymore, but around an obstacle.

Due to the short sections the flow will not become fully developed, thus, the flow through the pore sections of an RRUC at high porosities will be mostly in the developing stage. Similarly like in the stream-wise channel, Figures 5.24 (b) and 5.25 show that as the porosity increases the wall shear stress predicted by Du Plessis & Collins (1992) gives relative better approximations than the plane Poiseuille flow wall shear stress when compared to the numerical results.
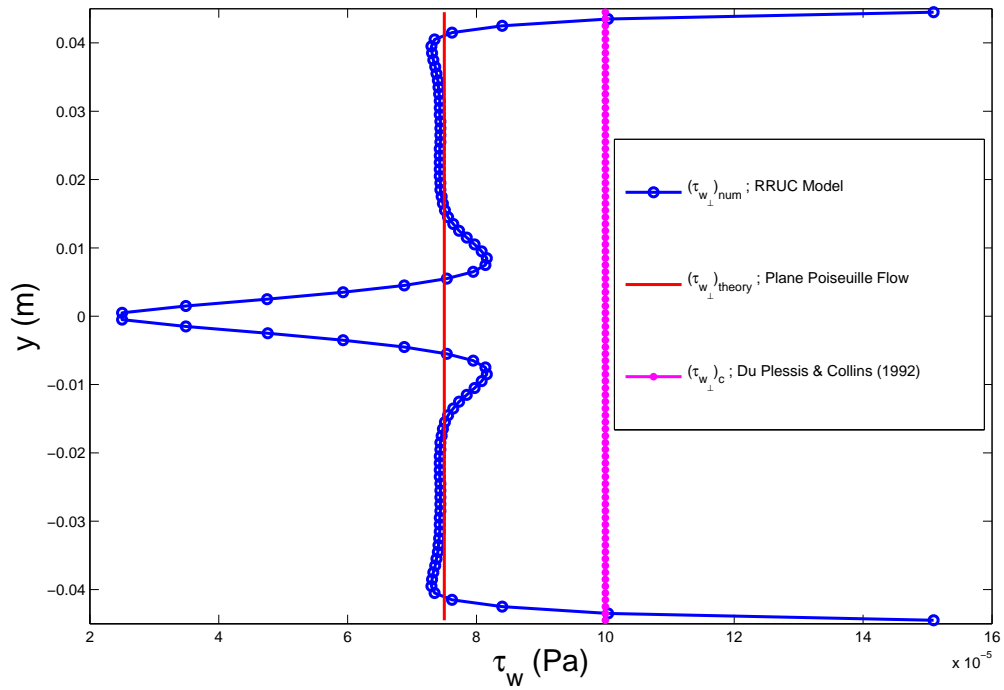
(a) $\epsilon = 0.19$; $Re_{c_\perp} = 2.5$
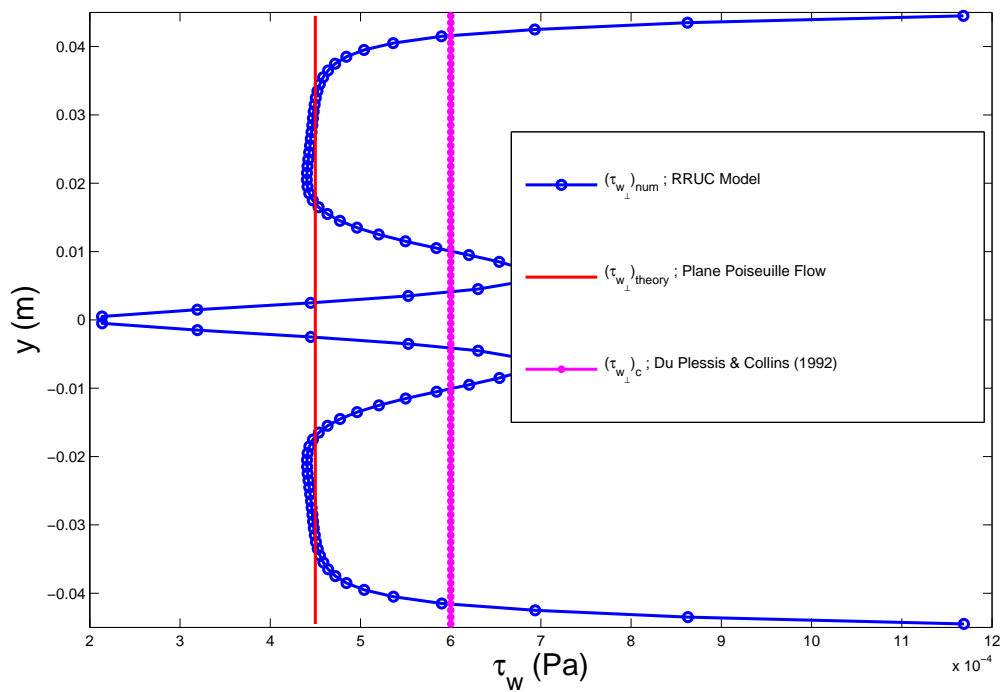
(b) $\epsilon = 0.19$; $Re_{c_\perp} = 15$

Figure 5.23: Dimensional transverse wall shear stress $\tau_{w_\perp}$ as a function of radial distance y for Case 1.
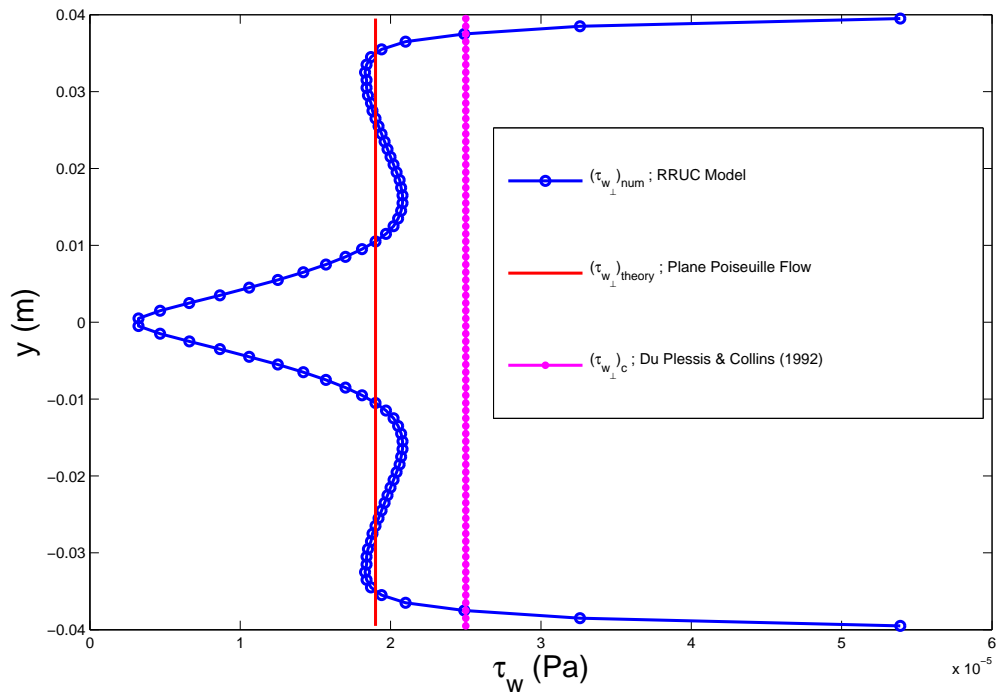
(a) $\epsilon = 0.36$; $Re_{c_\perp} = 2.5$
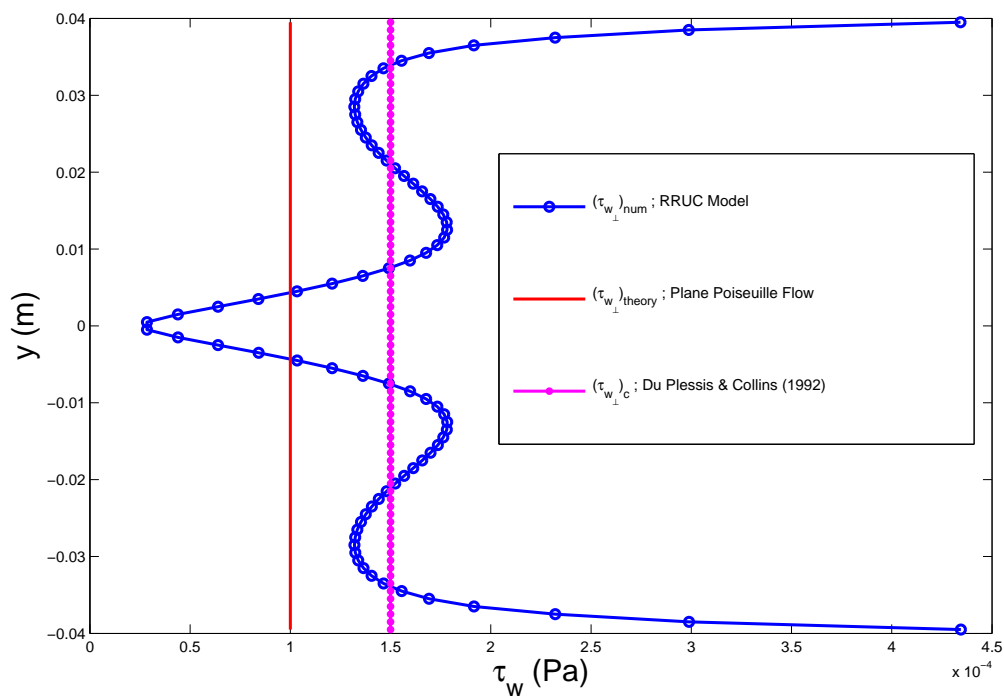
(b) $\epsilon = 0.36$; $Re_{c_\perp} = 15$

Figure 5.24: Dimensional transverse wall shear stress $\tau_{w_\perp}$ as a function of radial distance y for Case 2.
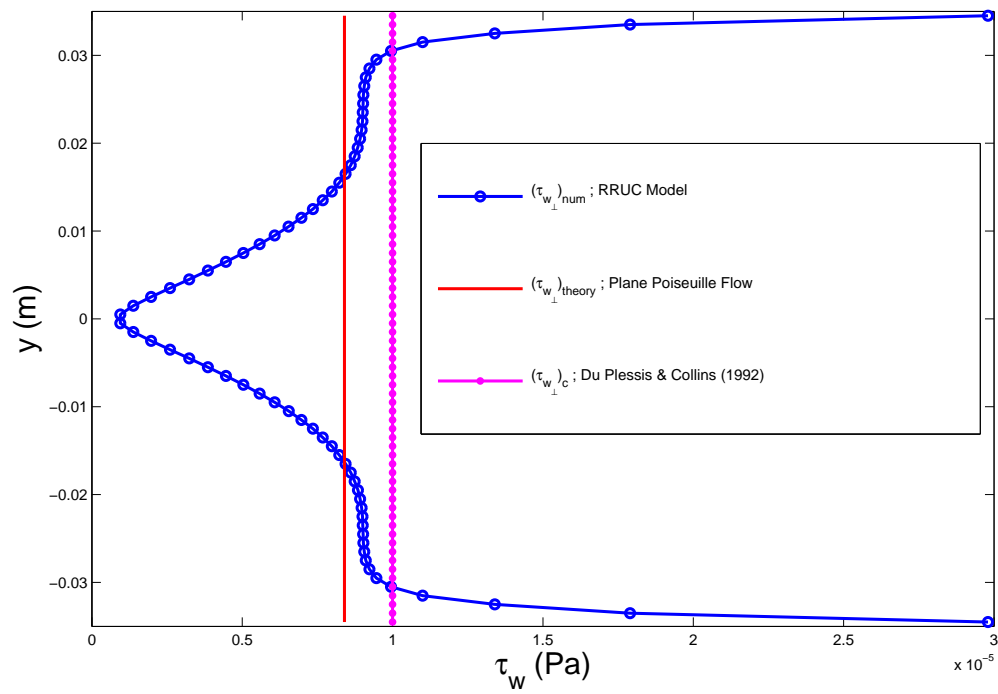
(a) $\epsilon = 0.51$; $Re_{c_\perp} = 2.5$

Figure 5.25: Dimensional transverse wall shear stress $\tau_{w_\perp}$ as a function of radial distance y for Case 3.

5.2.3 Comparison Between Models

This subsection is aimed at comparing the performance of the three different models described above, by graphically analyzing the dimensionless permeability, K, obtained from each model. The numerical results are also tested against the three analytical predictions. In this case as discussed previously the geometric configuration considered was an array of which square solids are staggered in the cross-sectional direction, yielding an aspect ratio α^* to be unity.

The dimensionless permeability K, is plotted as a function of porosity in Figure 5.26. All three models perform well at low porosities, with deviation from values predicted by Model 3, [Cloete & Du Plessis (2006)], as the porosity increases [Figure 5.26]. However these results are expected since for staggered configurations the model predicted the permeability for porosities up to a point where $d_{s_\perp} = d_{c_\perp}$. Despite the difference between Model 1, [Diedericks (1999)], and Model 2 [Lloyd et al. (2004)], they yield similar results with a slight difference at high porosities.

The numerical values in Figure 5.26 predicted the solutions of the three models very well at lower porosities, and followed closely the two models, [Diedericks (1999) and Lloyd et al. (2004)], as porosity increases.
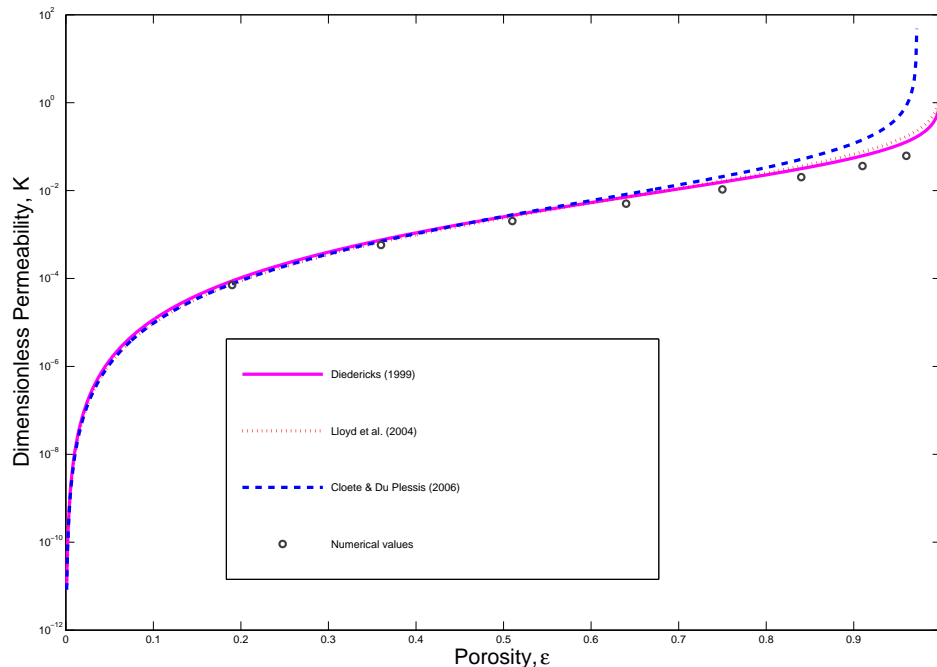
Figure 5.26: Numerical and analytical dimensionless permeability predictions.

5.3   Discussion

The theoretical based RRUC models under investigation in this study [Diedericks (1999), Lloyd et al. (2004) and Cloete & Du Plessis (2006)], assumed fully developed laminar flow in the pore sections of the porous domain, and the fluid-solid interface in both the stream-wise and transverse channels are exposed to a constant wall shear stress at very low Reynolds numbers. The main aim of the present analysis was to verify the capacity of the plane Poiseuille flow throughout the stream-wise and transverse channels of the porous geometry (RRUC). We also tested the performance of these models by analyzing the dimensionless permeability obtained from each model graphically.

To achieve our objective we performed a detailed numerical analysis of the velocity profiles and wall shear stress distribution in eight two-dimensional porous geometries referred to as Cases 1 to 8, each representing a different porosity, for Reynolds numbers ranging from 0.1 to 40. It should also be remarked that the effect of different porosities on the flow behaviour was also revealed. The numerical simulations of single-phase fluid flow between parallel plates presented in Chapter 4 resulted in comparable velocity profiles with the plane Poiseuille flow, confirming the validity of the data obtained by numerical simulation.

Numerical solutions gave good approximations when compared to the dimensionless permeability obtained from the three models for this range of porosities $0.19 \leq \epsilon \leq 0.75$. It was shown in Figure 5.26 that the numerical solutions for the remaining porosities considered, approximated solutions obtained from Model 1 and 2 fairly well. Thus it can be concluded that the models can be successfully used to predict the permeability for flow through porous structures similar to our computational domains to reduce the empiricism on this value.

To determine more precisely the areas over which the flow is fully developed, we analyzed the velocity profile at various positions from the leading edge A of the parallel surfaces chosen for investigation. The simulations showed that the velocity profile in the stream-wise direction is fully developed for the major percentage of the channel length. The velocity gradients only occurred at the leading edge A and downstream in the channel, due to the change of flow direction from the transverse channel to the stream-wise channel and vise versa caused by the sharp corners of the solid structures embedded in the RRUC geometry.

The predicted velocity profile in the transverse channel approximated fully developed flow conditions less accurately when compared to the estimations from the stream-wise channels. However, the fully developed flow was observed in some sections of the transverse channels at very low porosities. This difference in the parabolic velocity profile in the transverse channels is more predominant at high porosities as illustrated in the figures. It can be concluded that the flow in the transverse channel deviate from the plane poiseuille flow at high porosi-

ties, due to the fact that as porosity increases only small sections of the parallel surfaces are opposite each other.

Therefore, based on the velocity profiles predicted numerically, a general conclusion can be made that indeed the plane Poiseuille flow between all pairs of parallel surfaces exists only for very low porosities ($\epsilon \ll 0.5$). Furthermore it should also be mentioned that the plane Poiseuille flow is approximated much better in the stream-wise channels than transverse channels, as it was observed earlier that the parabolic velocity profile in the stream-wise channel prevail for porosities slightly higher than 0.5, ($\epsilon \leq 0.75$). The numerical results were further analyzed to determine the wall shear stresses along the fluid-solid interfaces in the stream-wise and transverse channels.

The wall shear stress predicted numerically, in the stream-wise direction estimated the theoretical wall shear stress $(\tau_w)_{\text{theory}}$ fairly accurately, except at the entrance region and exit region, for the same reasons advanced for the velocity profile. However, it is once more demonstrated that the results in the transverse channel do not produce the expected conditions. It was shown graphically, in the previous section, that the wall shear stress becomes constant at a certain section of the transverse wall at very low porosities. The wall shear stress in the transverse channel drops by more than 60% from the constant value and the variations of the wall shear stress became greater as the porosity is increased.

It should also be mentioned that a geometric configuration considered for this analysis has limitations. As porosity reaches $\epsilon \equiv 0.75$ the solid structures in the transverse channels do not overlap anymore to form parallel surfaces with the neighbouring solid structures. From Figures 5.16 through 5.25 for both the stream-wise and transverse channels, we noticed that, in contrast with the numerical wall shear stress, which reaches asymptotically the fully developed flow values, and the plane Poiseuille flow wall shear stress, the wall shear stress distribution obtained using Du Plessis & Collins (1992)'s analysis, exhibited a certain deviation except in certain cases mentioned in the previous section.

The computations clearly showed that the plane Poiseuille flow conditions are not well represented in the transverse channels of the porous media. Thus, further work should focus on the means, either numerically or theoretically, to correctly determine the wall shear stress at regions where the flow is not fully developed and in cases of higher porosities. Based on simulation predictions it is recommended that for low porosities the fluid-solid interface in the transverse channels, should be divided into sections, where the flow has reached the fully developed flow condition and the other section should represent the wall shear stress where it forms a certain percentage of the constant value given by equation (5.6), or should be represented by other estimations for wall shear stress τ_w, for an example, estimation according to Du Plessis & Collins (1992) at higher porosities.

Chapter 6

A Simulation of Airflow Through a Timber Stack End

The purpose of this chapter is twofold: to better understand the process of timber drying in a timber drying kiln and a CFD analysis will be performed on a section of a scale model tested in a wind tunnel, conducted by Du Plessis (2002), to investigate the airflow through the timber stack in a drying kiln, which forms the major purpose of this chapter. The numerical results will be compared to the experiment measurements obtained by Du Plessis (2002).

Experimental laboratory kilns are used for drying schedule development or optimization but this approach is expensive, time consuming and the results are not always representative of industrial drying as far as biological variability and energy consumption are concerned, [Fortin et al. (2004)]. If the numerical results could successfully predict the experimental data, this will demonstrate that the CFD models can provide fast, reliable and low cost solutions. This will be of great help to the timber drying kiln designers and operators, to overcome the challenges experienced in the laboratories as indicated by Fortin et al. (2004).

The stacking arrangement of timber in a timber drying kiln, results in the staggered ends that resembles an anisotropic porous structure. Hence, the two-dimensional pore scale models, for an anisotropic porous media presented in Section 2.2, are used to predict the airflow through the timber stack ends. This investigation forms the second purpose of this study.

Firdaouss & Du Plessis (2004) indicated that the circulation of warm air through a timber stack for drying, is an example of flow through porous structures modeled by the RRUC models in Chapter 2. This phenomenon guarantee us a fair comparison. The analytic predictions obtained from the pore scale models will be tested against the experimental data as well. The numerical results will again be validated gainst the three RRUC models as presented in Section 2.2. The subsequent section will give a brief background of wood drying in a timber drying kiln.

6.1 Airflow Through A Stack In A Timber-Drying Kiln

Wood drying is a process where the moisture content of the wood is reduced to a specific level. One primary method for drying timber is through air drying, which exposes the stack of sawn timber to natural atmospheric conditions. It is said that this method is cheaper but, it also has certain limitations for example it can be a slow process during winter in South Africa. The disadvantage of this method is that, the drying rate depends on the prevailing weather conditions and there is little control over the drying degrade. Therefore, timber drying kilns were developed to overcome some of the limitations that the air drying method has.

Drying timber protects timber against stains, decay and damage caused by insects, it also adds value to the wood processing industries. Drying of green timber can be expensive and time consuming, however, a well designed timber drying kiln makes it possible to dry timber boards to an acceptable standard in the shortest time in order to produce quality wood products. A timber drying kiln may be defined as a closed structure designed for the purpose of reducing the moisture content of timber and other wood products. A schematic diagram of a typical timber kiln is shown in Figure 6.1.

The process of kiln drying is energy intensive because great amount of energy is needed to reduce the total amount of water in timbers to a specific percentage of moisture content. The contribution of energy to the total drying of timber is obtained from direct fire, that is, burning wood wastes, although some kilns use heat exchangers to generate heat. Electrical energy is also used to generate air movement through timber stack by means of fans.

Drying Conditions (air temperature, humidity and air velocity) and the changes of these conditions within a timber stack can affect the drying rate and the moisture content distribution, [Hua et al. (2001)]. Hence, the goal of most researchers has been to develop drying schedules which can achieve maximum drying rate with less drying defects. Due to technological advances the operation of modern kilns depend on automated, computerized drying schedules, which control the temperature, relative humidity and air velocity during the drying process. These

conditions are designed to increase the rate of drying so as to achieve the most economical drying conditions without causing drying defect.

The configuration of wood stack in a wood drying kiln has a great influence on the air flow pattern, [Sun & Carrington (1999)]. The correct piling of timber is of importance in optimizing the drying process. Stickers are small uniform sized boards, which create spaces for air to move across the timber stack. The stickers are used in stacks to give space between timbers so that air can move through the stack. Based on the way the timber boards are stacked, their configuration can be divided into three parts. The first is the central area where the boards create a flat rectangular duct section in the flow direction. The other two parts have a staggered layout at both ends of the stack, [Smit et al. (2007)]. A picture of a timber stack showing how the stickers are used is shown in Figure 6.2.

The optimization of kilns does not depend only on the well controlled drying schedule and proper stacking of timber, it is also necessary to consider the influence of the airflow across the timber stack. Airflow is necessary to transfer hot and moist air through the timber stacks. The uniformity of drying and the quality of the wood in a kiln are strongly influenced by the airflow, [Hua et al. (2001)]. Thus the airflow has a major impact on the final drying of wood.

Airflow resistance in a kiln is caused by changes in kiln geometry that affect the pressure loss in the kiln and redistribute the airflow, [Hua et al. (2001)]. Hence it is necessary when optimizing a kiln design to know the pressure loss across the stack for different configurations. The airflow in the timber drying kilns is influenced by parameters such as the geometry of the kiln plenum, air ducts, roof design, the timber dimensional control and the stacking method of wood, [Hua et al. (2001)]. In the next section we will see how the staggered ends of the stack influence the pressure through the timber stack in a kiln.
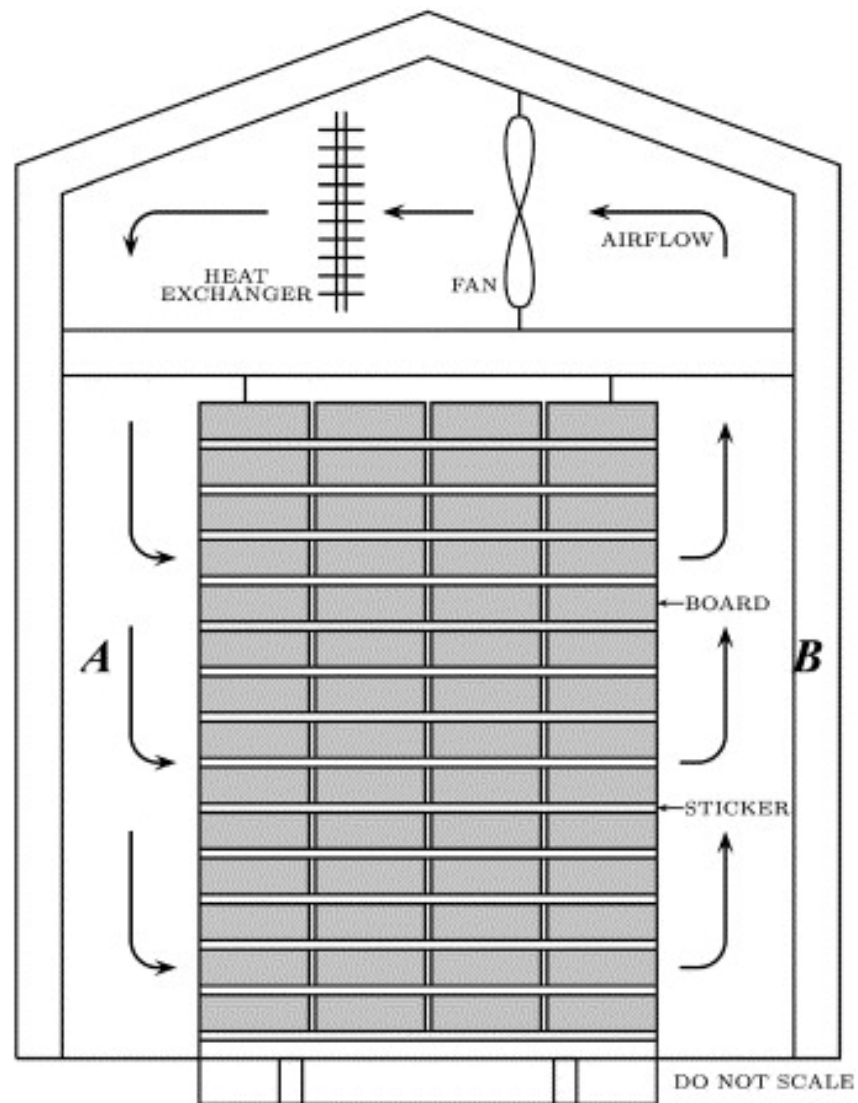
Figure 6.1: A schematic of a typical timber-drying kiln with a stack in the center.

Figure 6.2: A picture of a typical cross-piled timber stack to be dried in a kiln.

6.2   Review Of Experimental Data

The end parts of a stack, which are in a staggered form due to the stacking method, resemble a staggered configuration of an RRUC model presented in Section 2.2. For further analysis the staggered ends of the stack will be considered as a porous medium with an anisotropic unidirectional microstructure. The model tested in the experiment conducted by Du Plessis (2002) is depicted in Figure 6.3 and the simplified timber stack of the staggered ends is shown in Figure 6.4.

The applicable drag coefficient C_D, used in equations obtained from the RRUC models will be obtained from the drag coefficient values published by White[8] (1994). The drag coefficient was obtained for a range of rectangular cylinders with different aspect ratios. A curve fitted through the data resulted in the following expression [Du Plessis (2002)]

$$C_D = \left(c_1 + c_2 \left(\frac{d_{s_\parallel}}{d_{s_\perp}} \right) + c_3 \left(\frac{d_{s_\parallel}}{d_{s_\perp}} \right)^2 \right)^{-1} \tag{6.1}$$

where $c_1 = 0.238$; $c_2 = 0.198$; $c_3 = -0.00849$

Figure 6.3: Test model of stack end.

---

[8]Reference not read, referenced in Du Plessis (2002)
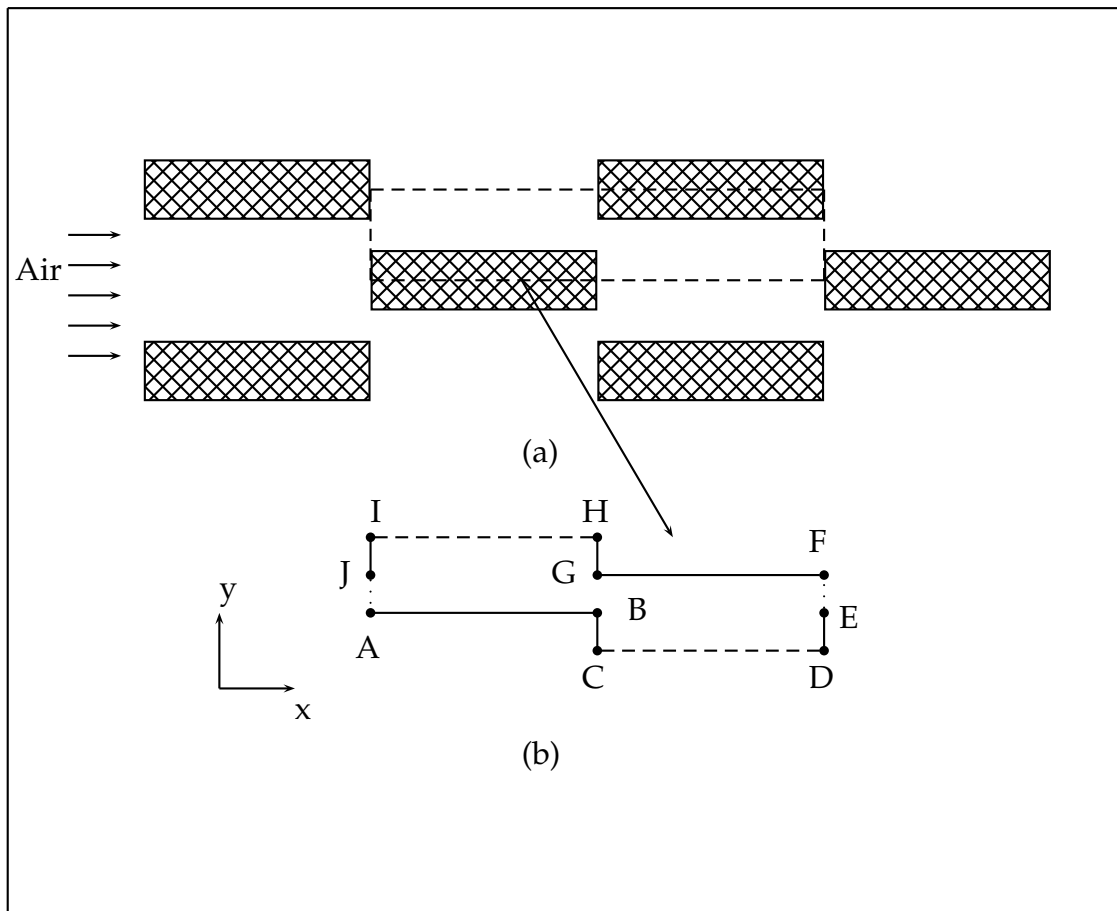
Figure 6.4: (a) A view of a section through stack end; (b) Computational domain considered in the airflow simulations.

 Du Plessis (2002) experimentally determined the pressure drop of airflow through the timber stack ends. Throughout the experiment the timber boards for the stack ends were placed in a controlled wind tunnel, and the air was forced through the inlet with a uniform speed. Measurements of pressure drop across the stack were conducted with a set of Betz manometers and standard Bernoulli obstruction flow meters. The volume airflow was calculated from the mouth pieces readings and air properties from which the air speed through the stack can be determined. The air properties used during the experiment and during the present numerical simulations are listed in Table 6.1 together with the dimensional values of the experimental model of the staggered stack.

Table 6.1: *Air properties and experimental data obtained from the model of a stack end in the wind tunnel.*

Property	Value	Variable	Description	Value [mm]
Temperature	20 [^oC]	-	Stack width	468
Density	1.225 [kg/m^3]	ρ	Stack height	485
Humidity	60 [%]	-	Stack depth	455
Viscosity	1.8 x 10^{-5} [N.s/m^2]	μ	Board width	65
			Board height	20.6
			Sticker width	20
			Sticker height	11.5
			Distance between stickers	428

The dimensional values presented by Du Plessis (2002) were used to obtained results for the RRUC model equations given in Section 2.2.4, and they are given in Table 6.2 below. The experimental results obtained by Du Plessis (2002) are presented in Table 6.3 and will be used later for comparison with numerical and theoretical models. In Table 6.3, Q is the total volume flow through the stack and Δp_{stack} is the total pressure drop across the experimental stack. Various parameters such as the mean velocity and the Fanning friction factor will be calculated using this data for comparison with the computed data.

Table 6.2: *Values used to produce results for the RRUC solution.*

Variable	Value
$d_\perp$	0.0332 [m]
$d_\parallel$	0.130 [m]
$d_{s_\perp}$	0.0206 [m]
$d_{s_\parallel}$	0.065 [m]
U_0/z	0.0044 [m^2]
ϵ	0.69
χ	1.82
β	0.19
C_D	1.29

Table 6.3: *Experimental data obtained from the model of a stack end in the wind tunnel.*

Airflow Q [m^3/s]	Δp_{stack} [Pa]
0.07422	2.5
0.11036	6
0.15685	10
0.23256	23
0.37496	55
0.56138	126
0.81999	271.5

6.3   Numerical Analysis

In this section, three different CFD viscous models, namely: Laminar model, Standard $k - \epsilon$ model and Reynolds-Stress model are evaluated by modeling an incompressible airflow across a portion of the scale model of the staggered timber ends, tested by Du Plessis (2002). FLUENT v6.2.16 facilitates the numerical simulation of fluid flow features using both laminar and turbulence models, by solving appropriate partial differential equations.

The two turbulence models were chosen randomly from a list of models available in Fluent Inc. (2005), after an earlier transition occurred in FLUENT when using the Laminar model. It is reported that the Standard $k - \epsilon$ model is widely used in turbulence simulations, because of its general applicability, despite its limitations of being a semi-empirical based model, [Fluent Inc. (2005)]. The effectiveness of the two turbulence models will also be investigated.

6.3.1   Problem Description And Boundary Conditions

Figure 6.4 (a) shows the staggered arrangement of six timber boards of a large staggered timber stack. The basic unit indicated by dashed lines is considered as a computational domain for this numerical model and is shown in Figure 6.4 (b). The dimensions used to create the computational geometry are the same as the ones used by Du Plessis (2002) for the RRUC models, also listed in Table 6.2. The present simulation assumes a periodic boundary condition over the computational domain.

The operating fluid in this case is air and the fluid is assumed to be Newtonian, incompressible and steady with constant properties. The variable parameter for these computations is the pressure gradient, and the flow Reynolds number varies from $0 \leq Re \leq 5538$. More than 40 cases were computed for this part of this study and the variable parameters for the three models considered are tabulated in Table 6.5 to 6.7.

The periodic boundary conditions were applied at lines AJ and EF from Figure 6.4 (b), symmetric boundary conditions were used at lines CD and HI and, the solid lines AC, BC, DE, FG, GH and IJ are modeled as walls. A no-slip boundary condition is imposed on these walls. For all the cases considered in this study the pressure gradient for each case was specified as the periodic boundary condition, and the predicted mass flow rate from FLUENT was used to calculate flow parameters of interest to this study.

6.3.2 Mesh Independence

The effect of the grid size on the accuracy of the results was evaluated by conducting three pre-tests simulations. The results were obtained using the default parameters provided by FLUENT, using the Reynolds-Stress model. The pressure gradient for this analysis was maintained at $\nabla p = -5.495$ [Pa/m], which gives a Reynolds number of $Re = 548.9$. The following three different grid sizes are employed, to achieve the optimum mesh,

(i) 3023 nodes; 2860 elements.

(ii) 4668 nodes; 4480 elements.

(iii) 6513 nodes; 6300 elements.

The computational results of the grid independence study are shown in Table 6.4. The results from Table 6.4 show that the numerical errors between (i) and (ii) meshes are 2.4% and 3.4% for the mass flow rate and maximum velocity respectively. The numerical error between (ii) and (iii) meshes is less than 2% for both the mass flow rate and maximum velocity.

Table 6.4: *Grid Independence.*

Number of elements	INPUT $-\nabla p$ [Pa/m]	OUTPUT Mass flow rate [kg/s]	OUTPUT u_{max} [m/s]
2860	5.495	0.0142	1.1968
4480	5.495	0.0146	1.2390
6300	5.495	0.0144	1.2280

Figure 6.5 shows the stream-wise velocity profiles for the three sets of grids tested at location $x = 0.065$ m. For the remaining computations, a grid size of 4480 number of elements has been used, as shown in Figure 6.5 and Table 6.4 that, this gives better results. The computational grid used in this simulation, meshed with quadrilateral elements is illustrated in Figure 6.6.
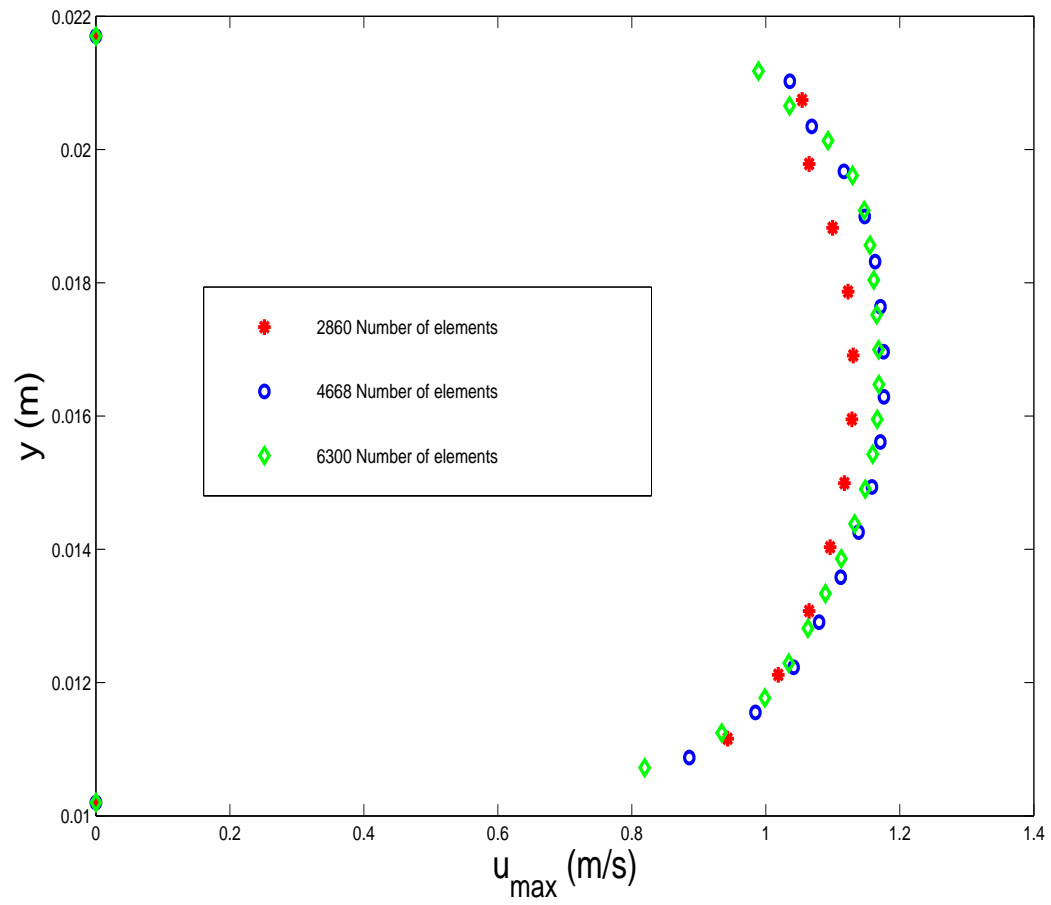
Figure 6.5: Velocity profiles
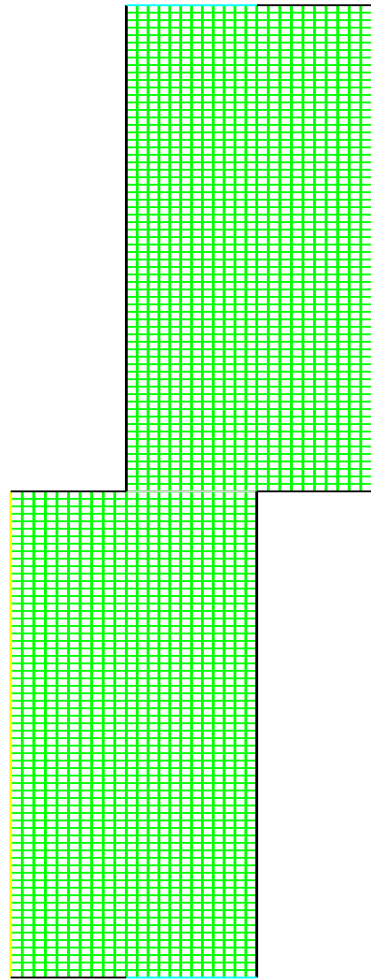
Figure 6.6: Mesh distributions

6.4   Presentation Of Results

This part of the present study was concerned with the numerical simulations of a steady laminar airflow through an anisotropic porous structure using SIMPLE based algorithm implemented into FLUENT version 6.2.16. Acceptable results could not be obtained with FLUENT using laminar model and therefore, we continued the simulations using the turbulence models. The wide array of available turbulence models, often developed for specific applications, creates a difficulty in selecting the right model for particular application. For this particular problem we chose the two turbulence models and one laminar model mentioned previously.

However, the two turbulence models are shown to consist of a different level of complexity, as well as computational efficiency , [Fluent Inc. (2005)]. Thus, the two models will be tested against the experimental data to test the sensitivity of these models on predicting the experiment values. The discussion of the results is divided into two sections: the first part will discuss the three viscous models flow characteristic prediction behaviour (such as recirculation zones, reattachment length and mean velocity). Secondly comparison of the numerical data with the experimental data and analytical predictions obtained from the RRUC models will be presented.

6.4.1   Evaluation Of The CFD Models

Various physical phenomena including flow separation, reattachment and recirculation are common features found in geometries similar to the computational domain considered in this chapter. This subsection will assess these features observed using the three mentioned models. Lack of experimental data, conducted by Du Plessis (2002), on the features mentioned above (recirculations and reattachment lengths) precludes the direct comparison with the numerical solutions. However, this section serves to demonstrate the difference between the models considered.

As mentioned earlier the predicted solutions computed using the viscous laminar model started to diverge at $Re = 108$, and we continued the computations using the turbulence models. It is evident from the value of the Reynolds number that the transition occurred under laminar flow conditions. Therefore, the use of turbulence models does not imply that the airflow through a timber stack experience turbulence immediately after the transition. The mean velocity obtained from the two turbulence models will be compared with the mean velocity calculated using the experimental data.

The pressure gradients specified as periodic boundary condition for the three models are tabulated in Tables 6.5 to 6.7. It is worth mentioning that the pressure gradients listed in Tables 6.6 and 6.7 from number 8 to 14, are specified from the experimental conditions and the Reynolds number was computed from the predicted results. The mass flow rates are also included in Tables 6.5 to 6.7 and they will be used in computing the mean velocity. The difference between the two turbulence models started to show when, the computer processing time needed for the solutions to converge using Reynolds-Stress model was found to be significantly less than that for the Standard $k - \epsilon$ model.

Table 6.5: *Parameters and Results for "Laminar Model".*

No.	Δp [Pa]	$d_{\parallel}$ [m]	INPUT $-\frac{\Delta p}{d_{\parallel}}$ [Pa/m]	OUTPUT $\dot{m}$ [kg/s]
1	0.00002	0.455	$4.4\text{x}10^{-5}$	$1.3\text{x}10^{-6}$
2	0.00005	0.455	$1.1\text{x}10^{-4}$	$4.5\text{x}10^{-6}$
3	0.0001	0.455	$2.2\text{x}10^{-4}$	$8.9\text{x}10^{-6}$
4	0.0005	0.455	$1.1\text{x}10^{-3}$	$4.3\text{x}10^{-5}$
5	0.001	0.455	$2.2\text{x}10^{-3}$	$8.4\text{x}10^{-5}$
6	0.002	0.455	$4.4\text{x}10^{-3}$	0.00016
7	0.003	0.455	$6.6\text{x}10^{-3}$	0.0002
8	0.004	0.455	$8.8\text{x}10^{-3}$	0.00028
9	0.005	0.455	0.01	0.00034
10	0.01	0.455	0.02	0.0006
11	0.02	0.455	0.04	0.0009
12	0.03	0.455	0.07	0.0013
13	0.04	0.455	0.09	0.0015
14	0.05	0.455	0.11	0.0018
15	0.1	0.455	0.22	0.0029

Table 6.6: *Parameters and Results for "Standard $k - \epsilon$ Model"*.

No.	Δp [Pa]	$d_{\parallel}$ [m]	INPUT $-\frac{\Delta p}{d_{\parallel}}$ [Pa/m]	OUTPUT $\dot{m}$ [kg/s]
1	0.15	0.455	0.33	0.0028
2	0.2	0.455	0.44	0.003
3	0.25	0.455	0.55	0.004
4	0.5	0.455	1.10	0.005
5	1	0.455	2.20	0.008
6	1.5	0.455	3.30	0.010
7	2	0.455	4.40	0.0111
8	2.5	0.455	5.50	0.0125
9	6	0.455	13.19	0.0195
10	10	0.455	21.98	0.025
11	23	0.455	50.55	0.038
12	55	0.455	120.88	0.059
13	126	0.455	276.92	0.090
14	271.5	0.455	596.70	0.133

Table 6.7: *Parameters and Results for "Reynolds-Stress Model"*.

No.	Δp [Pa]	$d_{\parallel}$ [m]	INPUT $-\frac{\Delta p}{d_{\parallel}}$ [Pa/m]	OUTPUT $\dot{m}$ [kg/s]
1	0.15	0.455	0.33	0.0032
2	0.2	0.455	0.44	0.0038
3	0.25	0.455	0.55	0.0045
4	0.5	0.455	1.10	0.0065
5	1	0.455	2.2	0.0093
6	1.5	0.455	3.3	0.011
7	2	0.455	4.40	0.013
8	2.5	0.455	5.50	0.0146
9	6	0.455	13.19	0.0225
10	10	0.455	21.98	0.030
11	23	0.455	50.55	0.045
12	55	0.455	120.90	0.068
13	126	0.455	276.92	0.098
14	271.5	0.455	596.70	0.141

The path lines coloured by velocity magnitude are illustrated in Figure 6.7 through to 6.10, in order to study the influence of the geometry as well as the Reynolds number on the fluid flow field. The laminar model simulation shows that the flow moves steadily throughout the computational domain at $Re = 0.14$. Figure 6.8 reveals the presence of small recirculation zones with very low velocity at the corners immediately upstream and downstream of the computational domain. The observation in Figure 6.8 is obtained from simulation using laminar viscous model at $Re = 5.9$. The recirculation regions should be expected in geometries similar to the current computational domain, since the flow encounters a sudden expansion followed by a sudden contraction.

The reattachment location is determined by finding the point where stream-wise wall shear stress is equal to zero. It is observed in Figure 6.11 (a) even though the flow started to recirculate in the laminar model regime the flow did not separate. The recirculation zones predicted by the two turbulence models are observed to grow in size as compared to the laminar model recirculations. In order to evaluate the difference between the two turbulence flow models by determining the reattachment lengths, we specified a similar periodic boundary condition at each model since the uniqueness of the solution is determined by the boundary conditions.

The different sizes of the recirculation zones depicted in Figures 6.8 and 6.9 are evident. The Standard $k - \epsilon$ model shows separation at more than one location. The first reattachment length predicted by the Standard $k - \epsilon$ model is at $x \equiv 0.002$ m and the second length is seen to take place at $x \equiv 0.008$ m. These predictions are illustrated in Figure 6.11 (b). The reattachment length predicted by the Reynolds stress model is longer than the one predicted by Standard $k - \epsilon$ and is at $x \equiv 0.025$ m as illustrated in Figure 6.11 (b). It is unfortunate that the predicted reattachment lengths can not be verified with the experimental results. However, it is clear that despite the unique boundary condition applied to the two turbulence models the predicted results showed different results.
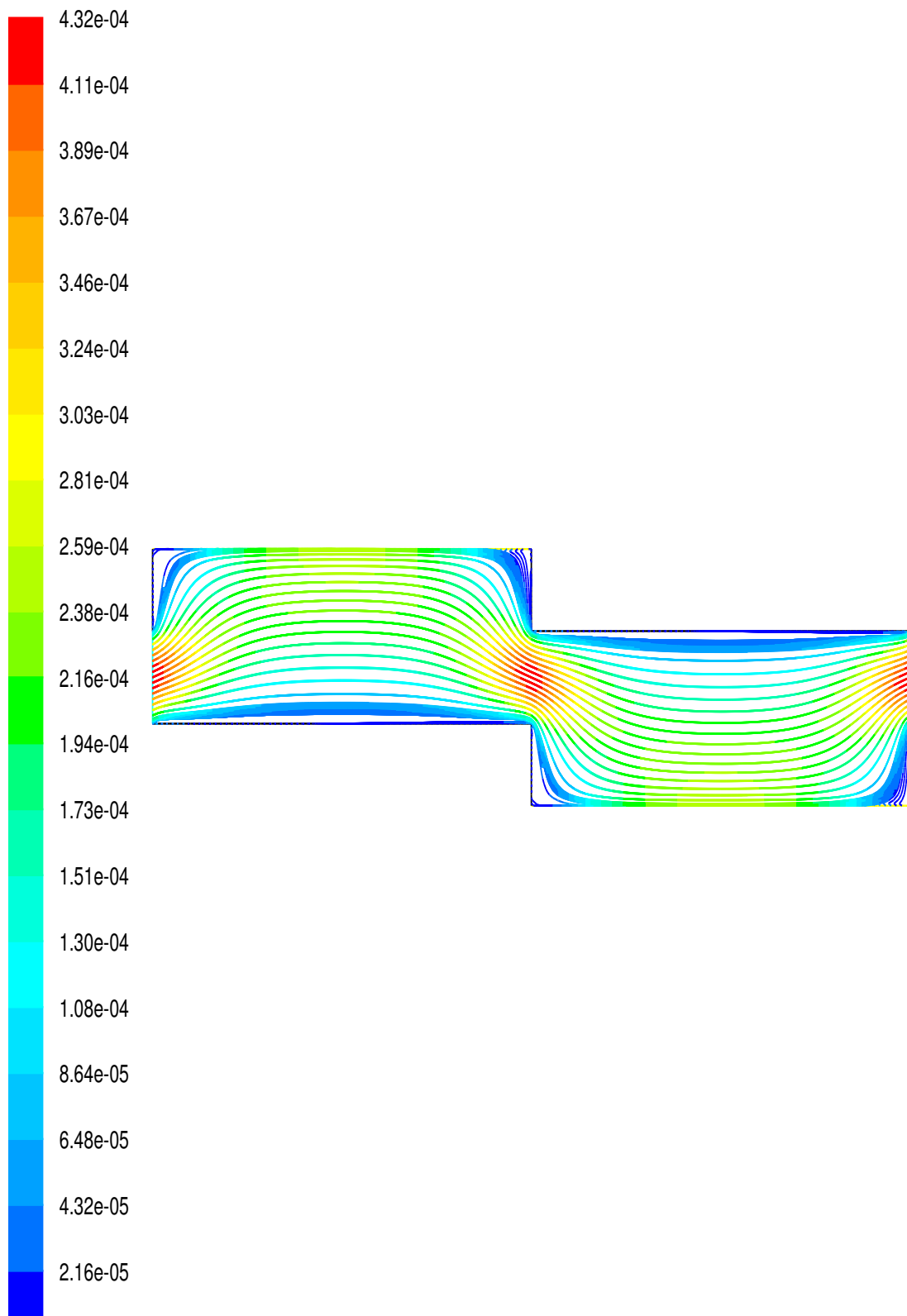
Figure 6.7: Predicted velocity path lines by Laminar viscous model, $Re = 0.14$.

1.51e-02
1.43e-02
1.36e-02
1.28e-02
1.21e-02
1.13e-02
1.06e-02
9.80e-03
9.05e-03
8.29e-03
7.54e-03
6.78e-03
6.03e-03
5.28e-03
4.52e-03
3.77e-03
3.02e-03
2.26e-03
1.51e-03
7.54e-04
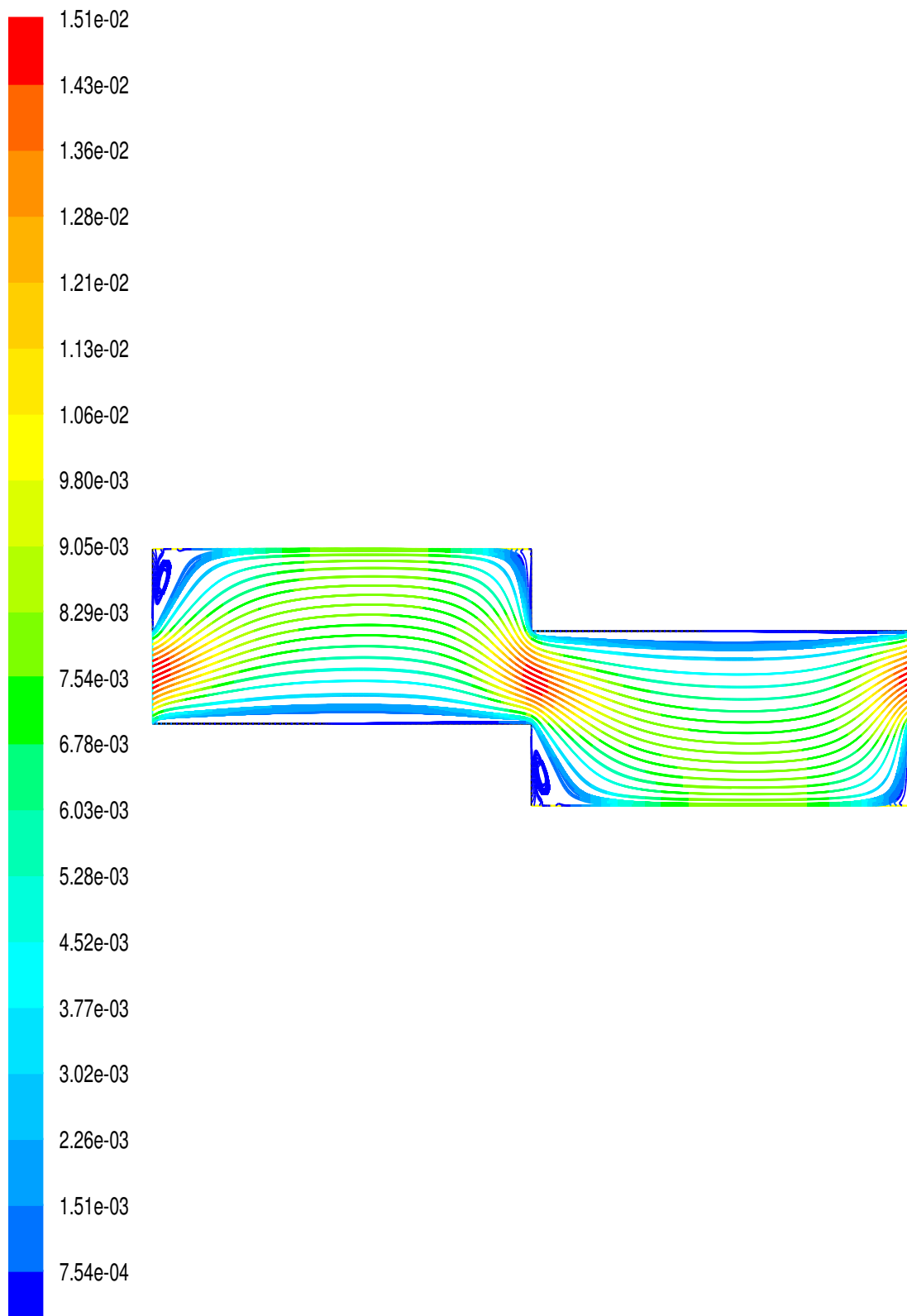
Figure 6.8: Predicted velocity path lines by Laminar viscous model, $Re = 5.9$.

1.04e+00
9.88e-01
9.36e-01
8.84e-01
8.32e-01
7.80e-01
7.28e-01
6.76e-01
6.24e-01
5.72e-01
5.20e-01
4.68e-01
4.16e-01
3.64e-01
3.12e-01
2.60e-01
2.08e-01
1.56e-01
1.04e-01
5.20e-02
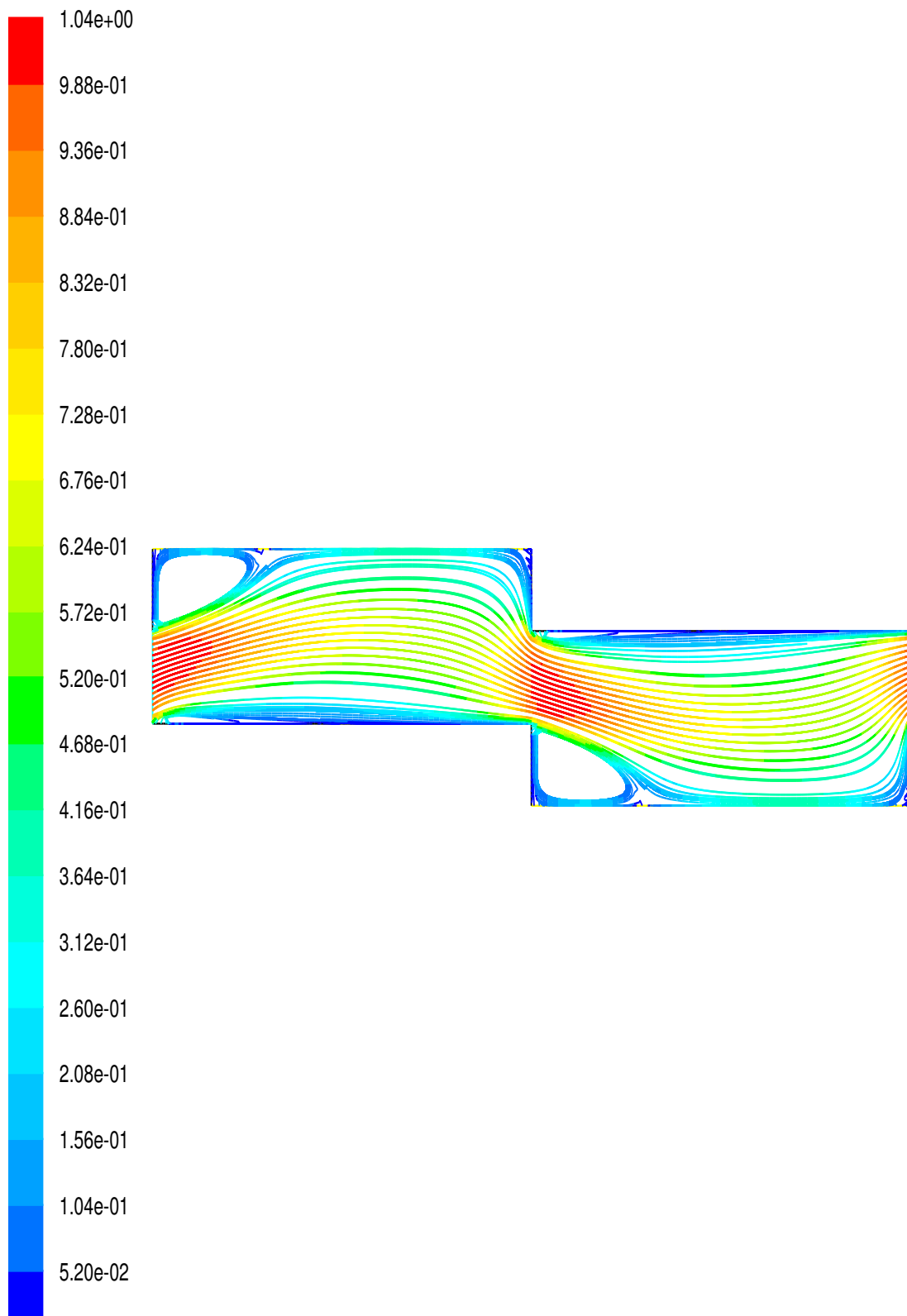
Figure 6.9: Predicted velocity path lines by Standard $k - \epsilon$ model, $Re = 0.14$.
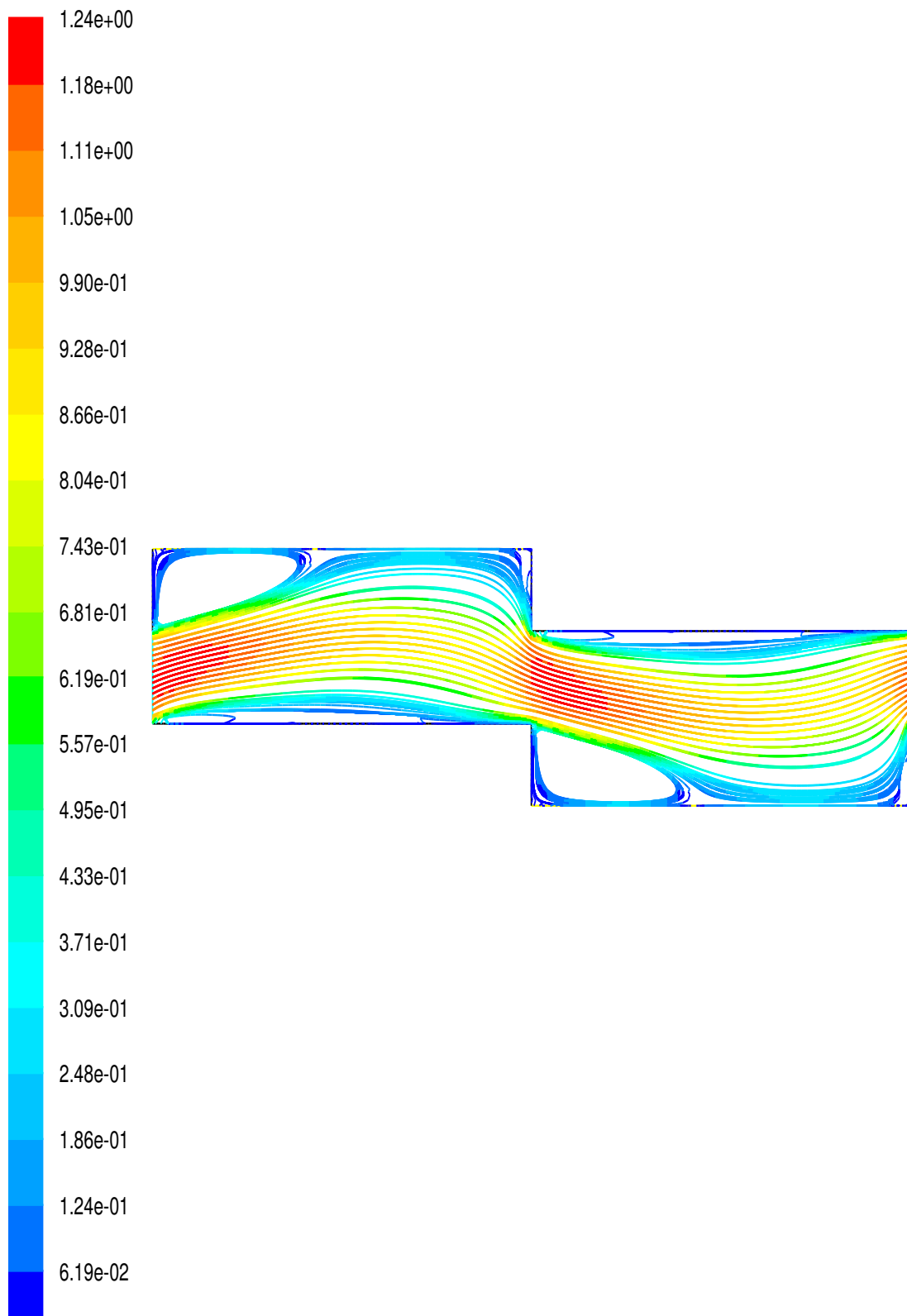
Figure 6.10: Predicted velocity path lines by Reynolds-Stress model, $Re = 0.14$
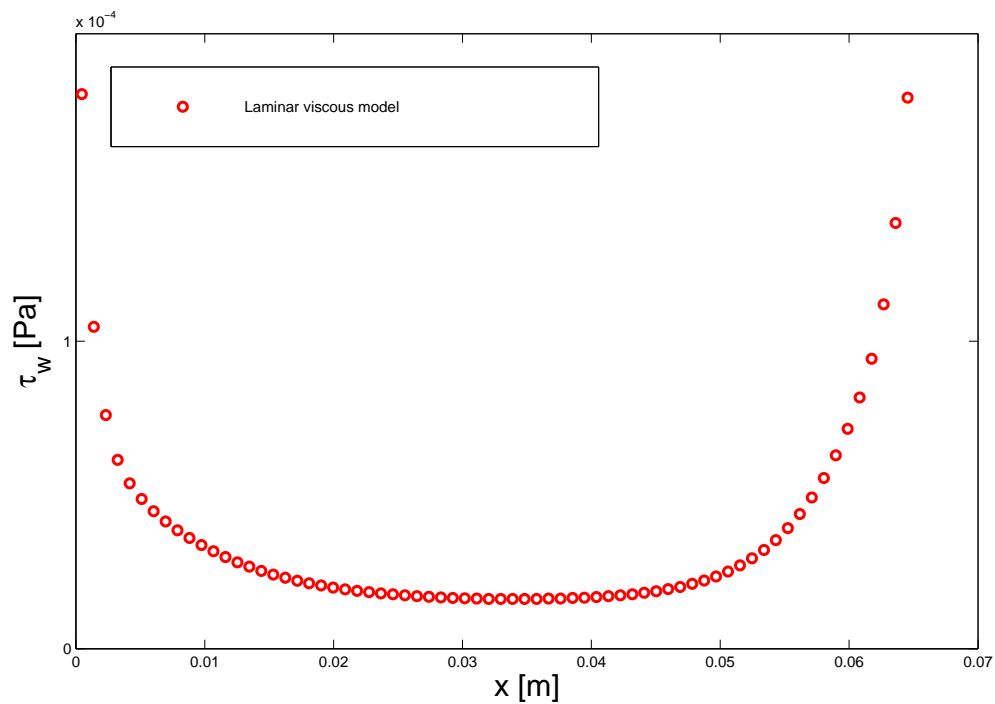
(a) τ_w predicted by Laminar viscous flow.
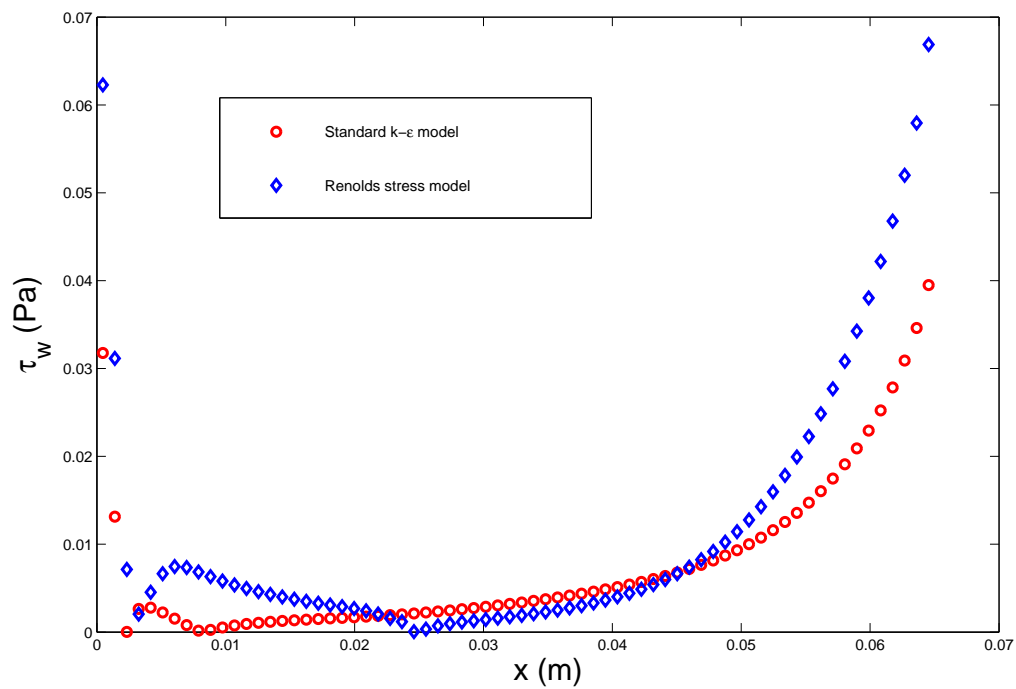
(b) τ_w predicted by Standard $k - \epsilon$ and Reynolds-Stress models.

Figure 6.11: Wall shear stress against the dimensional axil distance for predicted by Laminar viscous model ; Standard $k - \epsilon$ and Reynolds-Stress models.

The validation of the turbulence models against the experimental data is carried out here. The numerical mean velocities obtained using the computed mass flow rate from both the Standard $k - \epsilon$ and Reynolds-Stress models denoted by $(u_m)_{\text{num}}$ are calculated from the following expression,

$$(u_m)_{\text{num}} = \frac{\dot{m}_{\text{num}}}{\rho A},$$ (6.2)

where $\dot{m}_{(num)}$ is the numerical predicted mass flow rate, ρ is the fluid density and $A = d_{c_\perp}$ is the cross-sectional area. The mean velocity values through the entire experimental staggered timber stack obtained from the experimental data are calculated from the following expression,

$$(u_m)_{\text{exp}} = \left[\frac{Q_s}{H_s \times W_s} \right] \left(\frac{\chi}{\epsilon} \right),$$ (6.3)

where Q_s is the airflow through the stack, H_s is the stack height, W_s is the stack width, χ and ϵ are the tortuosity and the porosity of the anisotropic porous configuration, respectively. The experimental data will be used as a reference to compare the two turbulence models, and the comparison will be done through the percentage error (PE) for the mean velocity, which is defined as:

$$\mathrm{PE} = \frac{(u_m)_{\text{exp}} - (u_m)_{\text{num}}}{(u_m)_{\text{exp}}} \times 100\,\%.$$ (6.4)

According to the above expression for the percentage difference, positive values indicate that the numerical values under estimated while negative values indicate over estimation. A comparison of the numerical predicted mean velocities obtained from both the Standard $k - \epsilon$ and Reynolds-Stress models with the experimental data are summarized in Table 6.8 and 6.9, respectively together with their percentage error.

The pressure gradient $(-\nabla p)$, specified as an input, and the mass flow rate computed by FLUENT ($\dot{m}_{\text{num}}$) are listed again in Tables 6.8 and 6.9 for easy reference. For comparison, the mass flow rates obtained using experimental data are also listed in both tables mentioned above and they are represented by $\dot{m}_{\text{exp}}$.

Comparing the mean velocity obtained using the Standard $k - \epsilon$ model with the experimental mean velocity, as given in Table 6.8, it is apparent that the numerical predicted values under estimated the experimental data, except one value where the numerical solution over estimated the experimental data by 1.5 %. In this case the numerical results presented a difference ranging between 2.2 % and 9 % as listed in Table 6.8.

It is evident from Table 6.9 that the numerical mean velocities obtained using the Reynolds-Stress model tend to over estimate the measured values. The over estimation ranges between the maximum value of 17.7 % to the lowest value of 0.4 %. However, an under estimation of 0.8 %, for this case is observed also indicated in Table 6.9. In general the numerical predictive results compare fairly well with the experimental data.

Table 6.8: *Comparison of the predicted $(u_m)_{num}$ obtained using Standard $k - \epsilon$ model with measured $(u_m)_{exp}$ obtained from Du Plessis (2002) with their percentage errors.*

FLUENT-INPUT	FLUENT-OUTPUT				
$-\nabla p$	$\dot{m}_{num}$ [kg/s]	$\dot{m}_{exp}$ [kg/s]	$(u_m)_{num}$ [m/s]	$(u_m)_{exp}$ [m/s]	(PE) [%]
5.50	0.0125	0.0129	0.89	0.91	2.2
13.19	0.0195	0.0191	1.38	1.36	- 1.5
21.98	0.025	0.0272	1.79	1.93	7.3
50.55	0.038	0.0403	2.72	2.86	4.9
120.90	0.059	0.065	4.20	4.61	8.9
276.92	0.090	0.0973	6.39	6.90	7.4
596.70	0.133	0.1421	9.41	10.08	6.7

Table 6.9: *Comparison of the predicted $(u_m)_{num}$ obtained using Reynolds stress model with measured $(u_m)_{exp}$ obtained from Du Plessis (2002) with their percentage errors.*

FLUENT-INPUT	FLUENT-OUTPUT				
$-\nabla p$	$\dot{m}_{num}$ [kg/s]	$\dot{m}_{exp}$ [kg/s]	$(u_m)_{num}$ [m/s]	$(u_m)_{exp}$ [m/s]	(PE) [%]
5.50	0.0146	0.0129	1.03	0.91	- 13.2
13.19	0.0225	0.0191	1.60	1.36	- 17.7
21.98	0.030	0.0272	2.09	1.93	- 8.3
50.55	0.045	0.0403	3.19	2.86	- 11.5
120.90	0.068	0.065	4.84	4.61	- 5.0
276.92	0.098	0.0973	6.93	6.90	- 0.4
596.70	0.141	0.1421	10.00	10.08	0.8

6.4.2   Comparison Of The Numerical Results With Experimental And Theoretical Results.

A number of computations have been performed to investigate the airflow through a timber stack end shown in Figure 6.4 (b), using three different CFD models mentioned earlier. This subsection is aimed at validating the results obtained from these CFD models by comparing them with the experimental data obtained from Du Plessis (2002), and the solutions obtained from the expressions for the dimensionless friction factor through anisotropic porous media obtained in Chapter 2. The analytic predictions from the three RRUC model expressions will also be tested against the experimental data.

The predicted values obtained from all three viscous models considered in this problem and the experimental results by Du Plessis (2002) are presented as the dimensionless friction factor $Fd_{s_\perp}^2$ to be compared with the three RRUC models presented in Section 2.2. It is evident from the graphs in Figure 6.12 to 6.14 that equations (2.47) and (2.49) yield results that are not near the experimental data, therefore, these two equations are not appropriate methods to represent the Forchheimer regime for this type of flow. Thus, for further comparison with the numerical results only the RRUC models from equations (2.62), (2.65) and (2.68) will be used.

Figure 6.12: Comparison of dimensionless friction factor between theoretical RRUC Model 1 equations with experimental data (Du Plessis (2002)); $\epsilon = 0.69$.
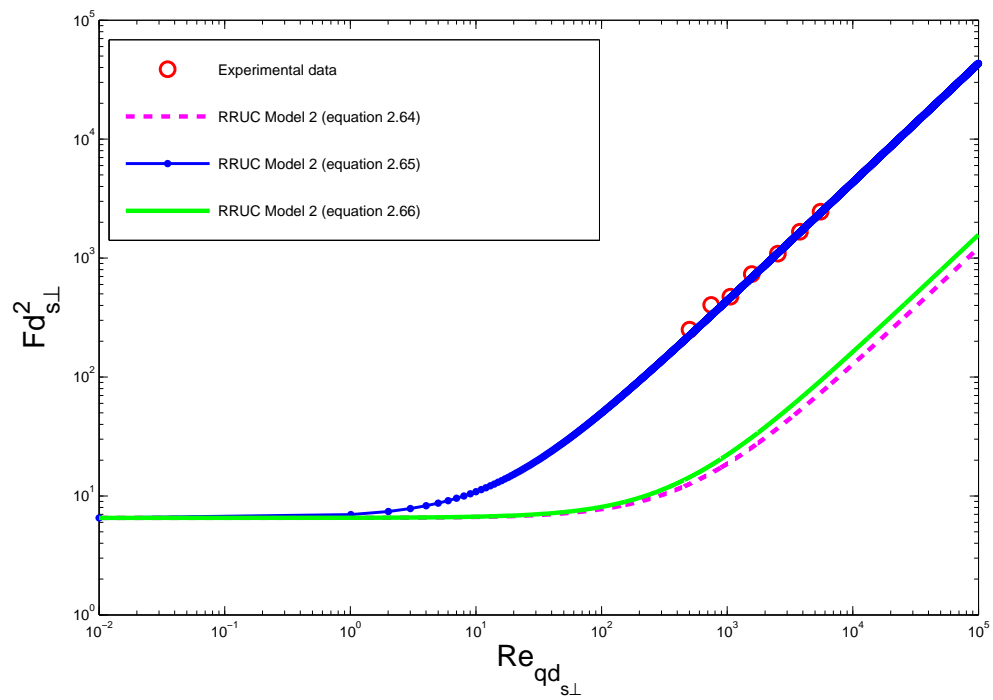
Figure 6.13: Comparison of dimensionless friction factor between theoretical RRUC Model 2 equations with experimental data (Du Plessis (2002)); $\epsilon = 0.69$.
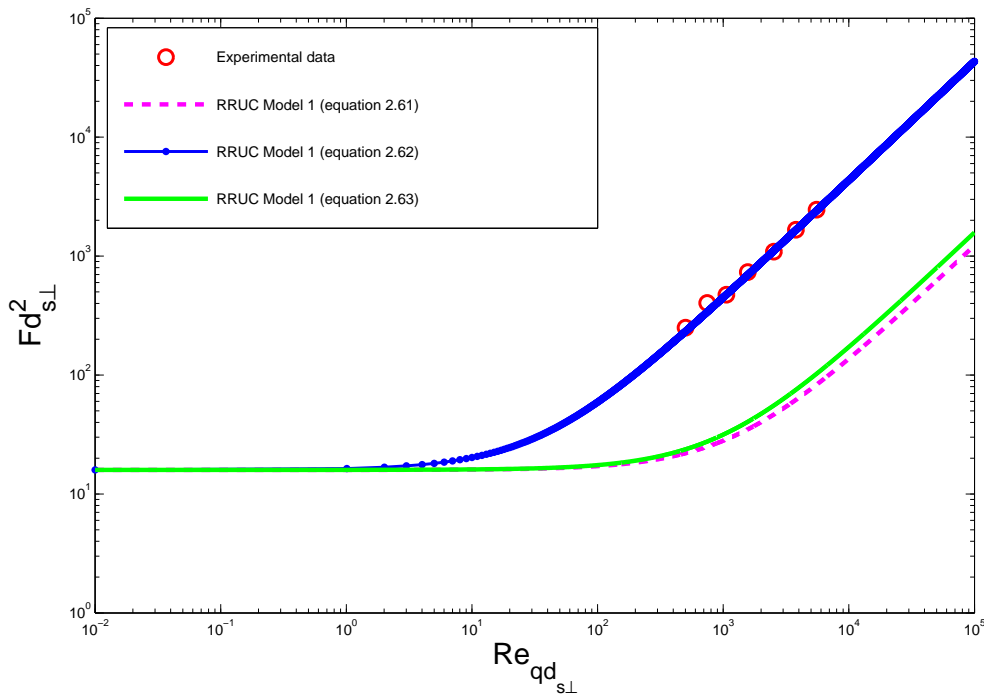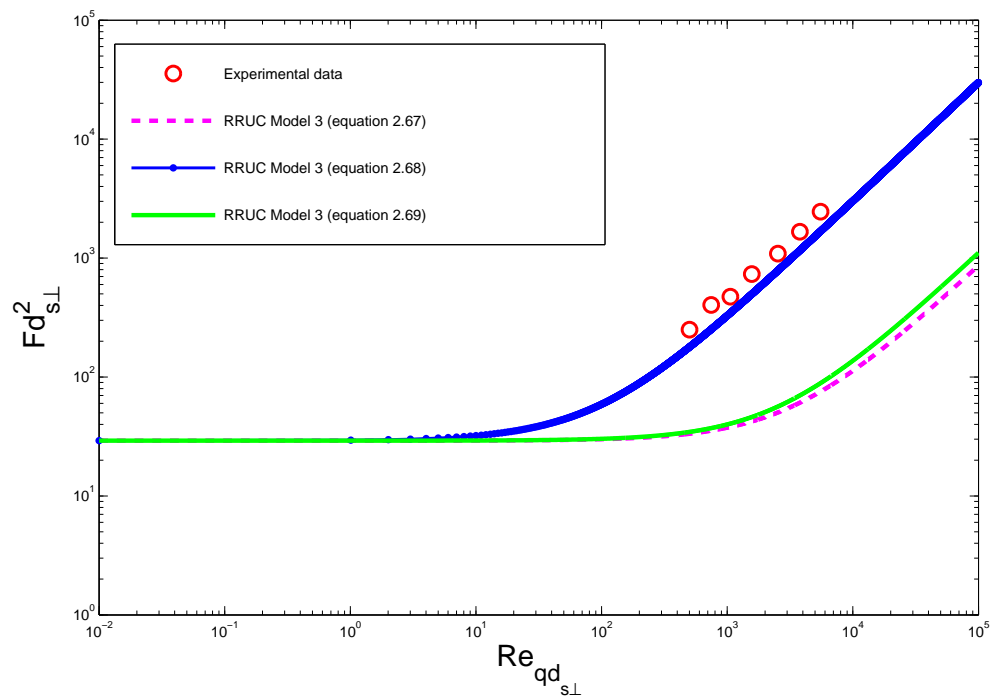
Figure 6.14: Comparison of dimensionless friction factor between theoretical RRUC Model 3 equations with experimental data (Du Plessis (2002)); $\epsilon = 0.69$.

Figure 6.15 through 6.17 illustrate the comparison between the three CFD models, the theoretical models and the experimental data. The results will be presented in the following chronological order: firstly the computed dimensionless friction factor obtained from the Laminar model, will be compared to the theoretical RRUC Model 1, Model 2 and Model 3, respectively. The numerical solutions obtained using the Standard $k - \epsilon$ and the Reynolds-Stress model will respectively, be compared to the three RRUC models. The two turbulence models (Standard $k - \epsilon$ and Reynolds-Stress models) will be validated using the experimental measurements. Lastly the theoretical RRUC models will also be tested against the experimental data.

The percentage errors listed in Tables 6.10 to 6.12 are calculated as the percentage of the difference between the dimensionless friction factor from the theoretical RRUC models and the numerical results divided by the theoretical models values. The percentage error expression yield:

$$\text{err} = \frac{(Fd_{s_\perp}^2)_{\text{RRUC}} - (Fd_{s_\perp}^2)_{\text{num}}}{(Fd_{s_\perp}^2)_{\text{RRUC}}} \times 100\,\% \tag{6.5}$$

The predicted dimensionless friction factor obtained from the Laminar viscous model are listed in Table 6.10 and illustrated in Figure 6.15 together with the results obtained from an RRUC Model 1 proposed by Diedericks (1999). It can be clearly seen from Figure 6.15 that the numerical solution from the laminar model correspond reasonably with the RRUC Model 1 results, obtained from equation (2.62). The percentage error between the two results represented by err_1 in Table 6.10 varies between 6.5 % and 26 %, except one point that is above the theoretical solution by 29.26 %.

Figure 6.16 illustrates the deviation of the numerical predicted results, obtained from the laminar model, from the theoretical RRUC Model 2, proposed by Lloyd et al. (2004). The numerical results in this case over estimated the theoretical results calculated from equation (2.65). The difference between the two results is listed in Table 6.10 as a percentage error represented by err_2. However, it is seen from Figure 6.16 that the numerical prediction becomes better as the Reynolds number increases but still in the laminar model regime.

The numerical dimensionless friction factor obtained from the laminar model gives less accurate results when compared to the theoretical RRUC Model 3 results proposed by Cloete & Du Plessis (2006). A comparison between the numerical data and the calculated dimensionless friction factor obtained from equation (2.68) is given in Figure 6.17, and as can be seen the numerical results under estimated the analytic predictions obtained from an RRUC Model 3. The numerical values in this case are lower by the difference ranging between 23 % and 49 %. This difference is presented in Table 6.10 as a percentage error represented by

err$_3$.

Table 6.10: *Comparison of the predicted $Fd_{s_\perp}^2$ obtained using "Laminar viscous model" with analytical predicted $Fd_{s_\perp}^2$ obtained from the three RRUC Models 1, 2 and 3 with their percentage errors.*

$Fd_{s_\perp}^2$							
$Re_{qd_{s_\perp}}$	RRUC Model 1	err$_1$ %	RRUC Model 2	err$_2$ %	RRUC Model3	err$_3$ %	Laminar Model
0.0486	15.9530	-29.26	6.5581	-214.44	29.1728	29.31	20.6213
0.1674	16.0044	6.48	6.6095	-126.46	29.2082	48.76	14.9677
0.3340	16.0765	6.66	6.6816	-124.59	29.2580	48.71	15.0062
1.6344	16.6393	7.85	7.2444	-111.66	29.6463	48.28	15.3335
3.1673	17.3027	8.54	7.9079	-100.12	30.1041	47.43	15.8249
5.9340	18.5001	8.68	9.1053	-85.53	30.9303	45.38	16.8934
8.3915	19.5637	8.41	10.1689	-76.21	31.6642	43.41	17.919
10.6279	20.5317	8.12	11.1368	-69.39	32.3321	41.65	18.8643
12.6988	21.4280	7.90	12.0331	-64.01	32.9505	40.11	19.735
21.5325	25.2512	7.82	15.8563	-46.80	35.5885	34.59	23.2775
35.4776	31.2866	9.69	21.8918	-29.07	39.7530	28.92	28.2557
47.0808	36.3084	12.04	26.9136	-18.67	43.2180	26.10	31.938
57.3638	40.7589	14.25	31.3641	-11.43	46.2888	24.49	34.9504
66.7931	44.8399	16.32	35.4451	-5.86	49.1047	23.59	37.5205
107.9226	62.6407	25.86	53.2459	12.78	61.3873	24.34	46.4428

As mentioned earlier, the use of the turbulence models do not imply that the flow experiences turbulence, therefore, for comparison with the RRUC models we assume that the flow is in the Forchheimer region at the point where FLU-ENT ceases to use the laminar model. On comparison with an RRUC Model 1 dimensionless friction factor, it becomes clear that the numerical solutions obtained from using the Standard $k - \epsilon$ model over estimated the analytical predictions. The comparison is schematically illustrated in Figure 6.15. The difference given in Table 6.11 as err$_1$ varies between 14% and 26%.

Although the numerical results obtained using the laminar model over estimated the analytical results obtained from an RRUC Model 2 in the Darcian regime, it is evident from Figure 6.16 that the Standard $k - \epsilon$ model results predicted the theoretical solutions nearly correctly in the Forchheimer regime. However, an over estimation ranging between 26% and 35% is observed as listed in Table 6.11 as err$_2$. The numerical results obtained using the same model as above also over estimated the results obtained from the RRUC Model 3 as depicted in Figure 6.17, but in this case the difference is higher when compared to the other two RRUC models. The difference is also listed in Table 6.11, ranging between 16% to a maximum value of 79.6% and these values are represented by err$_3$.

Table 6.11: *Comparison of the predicted $Fd_{s_\perp}^2$ obtained using "Standard $k - \epsilon$ model" with analytical predicted $Fd_{s_\perp}^2$ obtained from the three RRUC Models 1, 2 and 3 with their percentage errors.*

$Re_{qd_{s_\perp}}$	$Fd_{s_\perp}^2$						
	RRUC Model 1	err$_1$ %	RRUC Model 2	err$_2$ %	RRUC Model3	err$_3$ %	Standard $k - \epsilon$ Model
106.3	62.00	-14.03	52.60	-34.41	60.90	-16.09	70.70
124.6	69.90	-15.02	60.50	-32.89	66.40	-21.08	80.40
140.8	76.90	-15.73	67.50	-31.85	71.20	-25.00	89.00
204.1	104.30	-17.74	94.90	-29.40	90.10	-36.29	122.80
293.5	143.00	-19.44	133.60	-27.84	116.80	-46.23	170.80
362	172.60	-20.34	163.20	-27.27	137.30	-51.27	207.70
419.6	197.60	-20.90	188.20	-26.94	154.50	-54.63	238.90
470.4	219.50	-21.37	210.10	-26.80	169.60	-57.08	266.40
734.4	333.80	-22.68	324.40	-26.23	248.50	-64.79	409.50
950.8	427.40	-23.35	418.00	-26.12	313.10	-68.38	527.20
1442.1	640.10	-24.89	630.70	-26.75	459.80	-73.86	799.40
2229.8	981.00	-26.02	971.60	-27.24	695.10	-77.86	1236.30
3388.5	1482.50	-25.72	1473.10	-26.52	1041.10	-79.02	1863.80
4989	2175.10	-25.41	2165.70	-25.95	1519.00	-79.57	2727.70

Table 6.12 gives a summary of the comparison between the numerical results obtained using the Reynolds-Stress model and the three RRUC models. The numerical results are found to be less than the RRUC Model 1's results as listed in Table 6.12 and also illustrated in Figure 6.15. The percentage error represented by err$_1$ in Table 6.12 shows that the difference fluctuates between 8.4% and 25%. As mentioned previously, the negative percentage error indicates an over estimation, it also applies in this case. The numerical results also show a better correspondence with the results obtained from the RRUC Model 2, illustrated in Figure 6.16.

The percentage error, err$_2$, in Table 6.12 shows that at the point of transition when $Re = 120.5$, the numerical predictions over predicted the theoretical results and also when $Re = 143, 1442.1, 3677.9$ and 5306.6. At other values of the Reynolds numbers, err$_2$ shows that the numerical solutions under predicted the RRUC Model 2's results by a difference ranging from 4.09% to 9.13% also given in Table 6.12. The numerical results obtained from using the Reynolds stress model under estimated the RRUC Model 3's results as tabulated in Table 6.12 by err$_3$, but as the Reynolds number increases the numerical results yield higher values compared to the RRUC Model 3's results as depicted in Figure 6.17 and also listed in Table 6.12.

Table 6.12: *Comparison of the predicted $Fd_{s_\perp}^2$ obtained using "Reynolds-Stress model" with analytical predicted $Fd_{s_\perp}^2$ obtained from the three RRUC Models 1, 2 and 3 with their percentage errors.*

$Re_{qd_{s_\perp}}$	$Fd_{s_\perp}^2$						
	RRUC Model 1	err$_1$ %	RRUC Model 2	err$_2$ %	RRUC Model3	err$_3$ %	Reynolds-Stress Model
120.5	68.10	8.37	58.70	-6.30	65.10	4.15	62.40
143	77.80	9.90	68.40	-2.49	71.90	2.50	70.10
168.2	88.70	16.01	79.30	6.05	79.40	6.17	74.50
244.5	121.80	15.85	112.40	8.81	102.20	-0.29	102.50
349.4	167.20	14.23	157.80	9.13	133.50	-7.42	143.40
428.7	201.50	12.95	192.10	8.69	157.20	-11.58	175.40
494.8	230.10	11.95	220.70	8.20	176.90	-14.53	202.60
548.8	253.50	9.94	244.10	6.47	193.10	-18.23	228.30
848.9	383.30	7.57	373.90	5.24	282.70	-25.33	354.30
1110.5	496.60	9.12	487.20	7.37	360.80	-25.08	451.30
1442.1	640.10	-24.89	630.70	-26.75	459.80	-73.86	799.40
1693.3	748.80	9.08	739.40	7.93	534.80	-27.30	680.80
2569.4	1127.90	4.88	1118.60	4.09	796.40	-34.72	1072.90
3677.9	1607.70	-6.80	1598.30	-7.43	1127.50	-52.29	1717.10
5306.6	2312.60	-10.89	2303.20	-11.34	1613.90	-58.89	2564.40

The experimental data is also plotted on the graphs in Figures 6.15 through 6.17 and is used as a reference value in equation (6.5) to calculate the percentage error for comparison with both the numerical solutions and the analytical predictions from the three RRUC Models. Both the turbulence models yield a good approximation when compared to the experimental data as can be seen from all the three figures [Figure 6.15 to 6.17]. The percentage error between the experimental data and the Standard $k - \epsilon$ and Reynolds stress model is represented by err$_1$ and err$_2$, respectively in Table 6.13.

Table 6.13: *Comparison of the predicted $Fd_{s_\perp}^2$ obtained using "Standard $k - \epsilon$ model" and "Reynolds-Stress model" with the experimental data.*

	$Fd_{s_\perp}^2$				
$Re_{qd_{s_\perp}}$	Standard $k - \epsilon$ Model	err$_1$ %	Reynolds-Stress Model	err$_2$ %	Experimental Data
501.3	266.40	-6.56	228.30	8.68	250.00
745.3	409.50	-1.49	354.30	12.19	403.50
1059.3	527.20	-11.41	451.30	4.63	473.20
1570.7	799.40	-8.91	680.80	7.25	734.00
2532.4	1236.30	-13.57	1072.90	1.44	1088.60
3791.4	1863.80	-11.89	1717.10	-3.09	1665.70
5538	2727.70	-11.01	2564.40	-4.36	2457.20

The following comparison demonstrate how each RRUC model produces the experimental data. The difference between the experimental data and the results obtained from the expressions of the RRUC Model 1, 2 and 3 are listed in Table 6.14 as err$_1$, err$_2$ and err$_3$, respectively. The RRUC Model 1 and Model 2 predicted the experimental data fairly well as illustrated in Figures 6.15 and 6.16 respectively. However, as shown in Figure 6.17 the analytical predictions from the RRUC Model 3 under estimated the experimental data by far when compared to other two RRUC models.

Table 6.14: *Comparison of the analytic predicted $Fd_{s_\perp}^2$ obtained from the three RRUC Models 1, 2 and 3 with the experimental data.*

| $Re_{qd_{s_\perp}}$ | $Fd_{s_\perp}^2$ | | | | | | |
	RRUC Model 1	err_1 %	RRUC Model 2	err_2 %	RRUC Model3	err_3 %	Experimental Data
501.3	232.90	6.84	223.50	10.60	178.90	28.44	250.00
745.3	338.50	16.11	329.10	18.44	251.70	37.62	403.50
1059.3	474.40	-0.25	465.00	1.73	345.50	26.99	473.20
1570.7	695.70	5.22	686.30	6.50	498.20	32.13	734.00
2532.4	1111.90	-2.14	1102.60	-1.29	785.40	27.85	1088.60
3791.4	1656.90	0.53	1647.50	1.09	1161.40	30.28	1665.70
5538	2412.80	1.81	2403.40	2.19	1683.00	31.51	2457.20

Figure 6.15: Comparison between the friction factor predicted by Laminar viscous model ; Standard $k - \epsilon$ and Reynolds-Stress models with the experimental data and theoretical Model 1.

Figure 6.16: Comparison between the friction factor predicted by Laminar viscous model ; Standard $k - \epsilon$ and Reynolds-Stress models with the experimental data and theoretical Model 2.
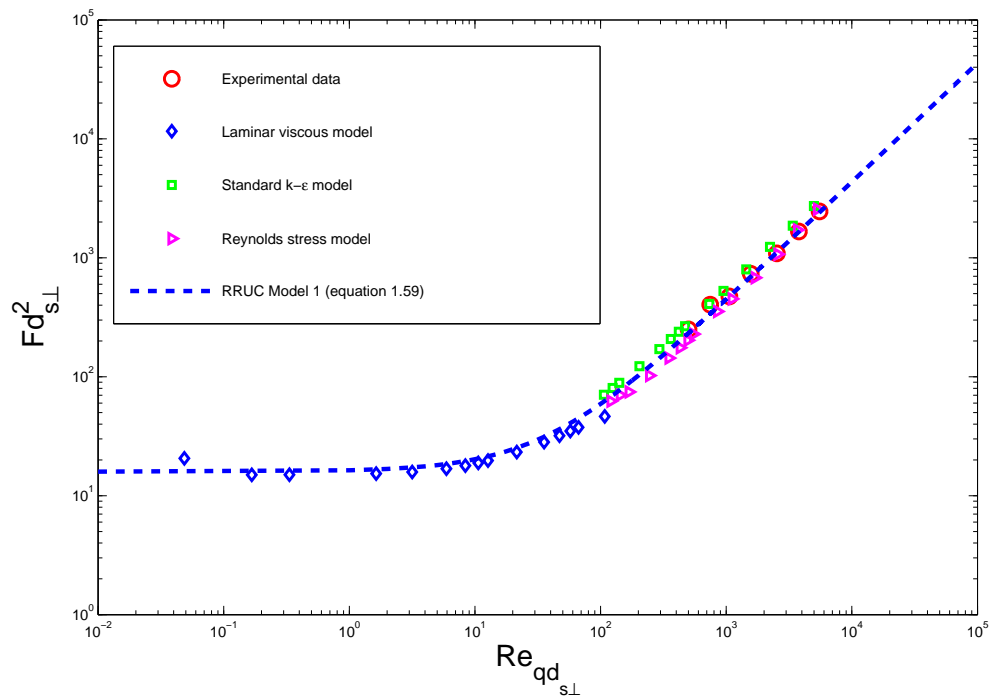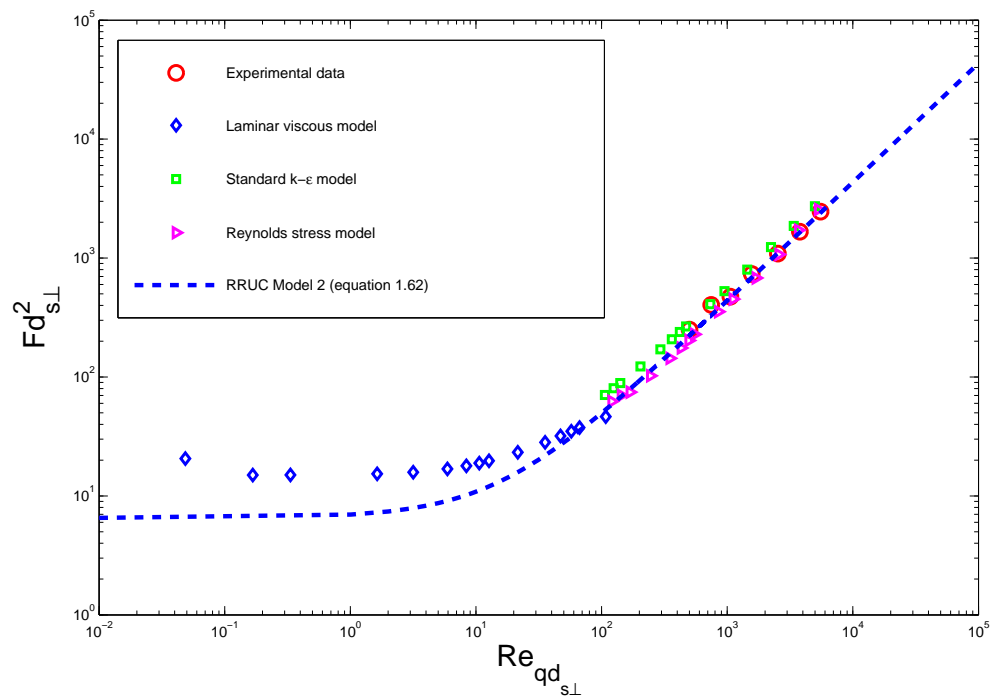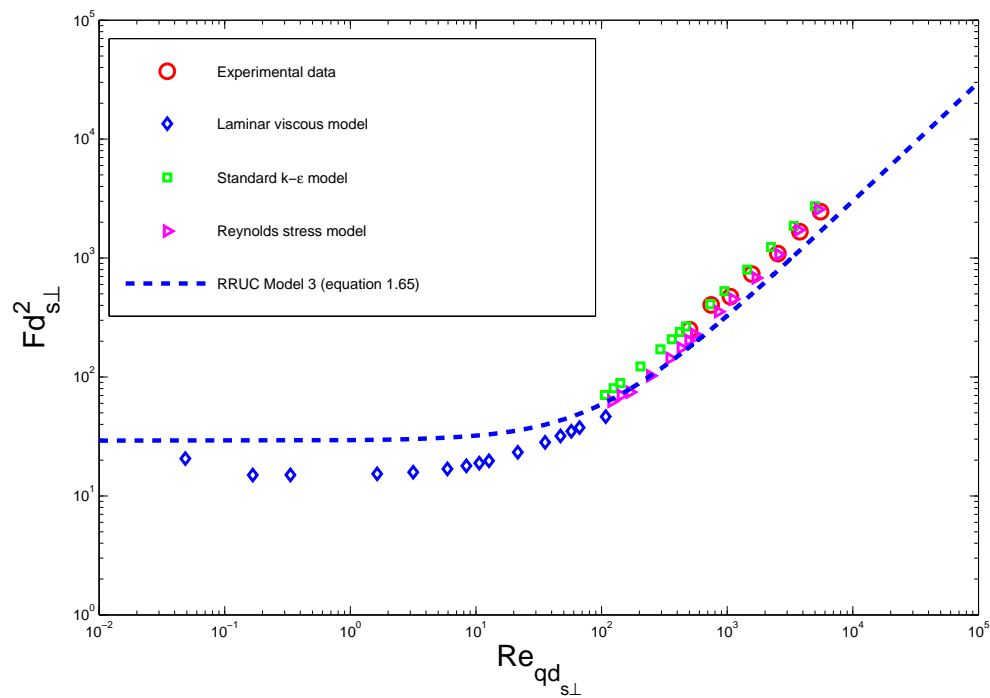
Figure 6.17: Comparison between the friction factor predicted by Laminar viscous model ; Standard $k - \epsilon$ and Reynolds-Stress models with the experimental data and theoretical Model 3.

6.5   Discussion

The pressure drop across the timber stack end in a timber drying kiln, presented as a dimensionless friction factor $Fd_{s_\perp}^2$, was the main parameter of interest of the present chapter. A set of numerical simulation has been carried out to simulate airflow through the timber stack end, resembling an anisotropic porous structure for several Reynolds numbers from a low value to 5538. The simulations were conducted using the commercial CFD code FLUENT 6.2.16.

The choice of grid size of 4668 nodes and 4480 number of elements was found to provide grid independence results reported in the previous sections of this chapter. Three tests for the grid independence were done, for the purpose of improving the accuracy of the results. The grids were refined with subsequent repeat of simulation to arrive at this grid distribution, as discussed in Subsection 6.3.2.

Du Plessis (2002) presented experimental measurements of the airflow through the entire timber stack, for both the inline and staggered ends. His results for the timber stack ends are used for comparison with the current simulation results, in order to gain confidence in the numerical predictions. Three different porous medium models representative of an anisotropic porous structure, referred to as RRUC Model 1, 2 and 3 have been introduced, and were applied to predict the dimensionless friction factor across the timber stack end. The numerical results were also validated using these models in both the Darcy and Forchheimer regimes. Lastly the RRUC models were tested against the experimental data.

The mean velocity profiles across the computational domain and parameters such as reattachment lengths and recirculation zones were also investigate. We noticed, as presented in Subsection 6.4.1 that the flow through the computational domain encountered a sudden expansion followed by a sudden contraction downstream, hence, the formation of the recirculation zones as the Reynolds number increases from very low values. The reattachment lengths obtained from using the Standard $k - \epsilon$ model and Reynolds-Stress model yielded different values, despite common boundary conditions applied to each model. This observation gave us an overview of these two models.

A comparison of the numerical mean velocity values, obtained from using both the Standard $k - \epsilon$ model and Reynolds stress model, with the experimental data is summarized in Tables 6.8 and 6.9. it is evident that the Standard $k - \epsilon$ model generally under estimated the experimental mean velocity values, while the Reynolds-Stress model's results over estimated the measured values. This observation also showed the difference between the two turbulence models.

The principal objective of the validation study presented above was to examine the sensitivity of the numerical results to the different models used in the present simulations by comparing them with the available data. In Subsection 6.4.2 we plotted the dimensionless friction factor $Fd_{s_\perp}^2$ as a function of the Reynolds number, as illustrated in Figures 6.15 through 6.17. A better correspondence of the numerical results, from all the CFD viscous models considered, with the analytical predictions from an RRUC Model 1, indicate that the model adequately addresses the geometric structure of the computational domain considered in this chapter. The predictions obtained from the RRUC Model 1 also predicted the experimental data fairly well, confirming the above statement.

The two turbulence models still show a slight difference when compared to both the experimental data and analytical predictions, as can be seen in Figures 6.15 to 6.17. Thus it can be concluded that the results obtained from each model are not unique. The Laminar viscous model gave less accurate results when compared with both the analytical predictions from the RRUC Models 2 and 3. The discrepancy in these cases is due to the limitations these models have on the geometric structure. However, the two turbulence models gave a reasonable correspondence when compared to the RRUC Model 2 in the Forchheimer region. The predictions from an RRUC Model 2 also compared well with the experimental data in this region.

Although equations (2.54) and (2.57) (Model 2 and 3) are reported to be sufficiently accurate for porosities up to 0.75 some limitations were revealed numerically in the previous chapter. This difference between the results predicted by RRUC Model 2 and 3 with the numerical results, is indicative of the fact that these two models are limited to a certain range of porosity less than 0.75 since the porosity for the current porous structure is 0.69.

Another factor contributing to the discrepancy between the predicted results, experimental data and the theoretical Model 3 may be explained by noting that the configuration of the present geometry, Figure 6.4, differs from the conceptual geometry used in the derivation of equation (2.57). For a staggered array, equation (2.57) was modeled for geometries where the solid phase in the transverse channel is greater than or equal to the width of the stream-wise fluid channel, $d_{s_\perp} \geq d_{c_\perp}$, [Cloete & Du Plessis (2006)].

Chapter 7

Conclusion

Detailed numerical studies were performed in order to investigate the quantitative correspondence of fully developed laminar flow in porous structures represented by an RRUC model. To achieve this, an investigation of low Reynolds number fluid flow in parallel plates has been conducted using a two dimensional finite-volume Navier-Stokes solver FLUENT, Fluent Inc. (2005). The validation of numerical solutions was accomplished by comparing numerical and analytical fully developed velocity profiles across the channel. In addition, hydrodynamic entrance lengths are compared with data published in earlier studies

The numerical results of the non-dimensional entrance length L_{hy}/D_H, determined using the different criteria showed not to vary with Reynolds number at $1 \leq Re \leq 60$ and increased with increasing Reynolds number. It was also observed that numerically predicted L_{hy}/ReD_H values are approximately constant at $Re \geq 80$. In general, the calculated values considered comparable with those reported in the literature. However based on numerical calculations and analysis, the entrance length proposed by Du Plessis & Collins seem to perform better than those predicted based on estimation of the centerline velocity of the fully developed flow.

As mentioned previously the main part of this study was to verify an assumption made in the RRUC pore-scale model with respect to the fully developed flow throughout the pore section. To accomplish this, we have simulated two-dimensional single phase fluid flow for eight different geometries. The periodic boundary conditions were used to attain the fully developed flow condition. Based on numerical analysis in a few geometries for porosities ranging from 0.19 to 0.96, we conclude that indeed the plane Poiseuille flow is constant through the stream-wise pore sections of the RRUC geometry, provided the porosity ϵ, does not exceed a certain threshold value. This upper limit, though, will vary depending on configuration of the geometry considered.

However, it was found that the plane Poiseuille flow is not well represented in the transverse channels. This research also underlines the care which must be taken in interpreting the wall shear stress along the transverse channels of the RRUC. It was numerically observed that the wall shear stress in the transverse channels cannot be estimated on the basis of the plane Poiseuille flow. It requires a careful separation of the wall shear stress in the transverse region of interest.

Three different numerical CFD models have been employed to simulate airflow through a section of the timber stack end model. The predictions of the anisotropic prismatic materials were validated against the experimental dimensionless friction factor and numerical predictions. The Standard $k - \epsilon$ and Reynolds-Stress turbulence models appeared to reflect the experimental conditions with equal accuracy. However, Reynolds-Stress model demanded less computational time than the Standard k-epsilon model, which could be a method of choice for large size problems.

Qualitative trends are captured equally well by the two turbulence models when compared to the dimensionless friction factor obtained from Model 1 and 2 in the Forchheimer regime. Model 1 and 2 proposed by Diedericks (1999) and Lloyd et al. (2004), provide the best overall approximation when compared with the experimental data. The numerical solutions in the Laminar model regime also gave good approximations when compared to RRUC Model 1 in the Darcian regime. RRUC Models 1 and 2 gave greater differences when compared to the numerical solutions in the Darcian regime.

In summary, we were able to confirm the plane Poiseuille flow through streamwise channels of the RRUC geometry numerically. We determined that the deterministic expression relating the pressure gradient to the flow rate of Newtonian fluid flow through anisotropic porous media (Model 1), despite its simplicity, may be successfully used in practical applications. CFD simulations using FLUENT (Fluent Inc. (2005), have proved to be a useful tool for predicting flow through complex geometries including porous media

Appendix A

Averaging Identities And Rules

A.1 Derivation Of Volume Averaging Identities

The averaging identities are useful when deriving and transforming the averaged transport equations. The following identities, with α constant and ψ and λ fluid phase tensors of similar order, are derived using the averaging operator definitions presented in Section 2.1.1. Only the Identities used in the volumetric averaging procedure are derived.

The relation between the phase average and intrinsic phase averages is given by

$$
\begin{aligned}
\langle \psi \rangle &= \frac{1}{U_0} \iiint_{U_f} \psi \, dU \\
&= \frac{U_f}{U_0} \frac{1}{U_f} \iiint_{U_f} \psi \, dU \\
&= \epsilon \langle \psi \rangle_f.
\end{aligned}
\tag{A.1}
$$

If we set $\psi = 1$ in equation (2.5) it follows that,

$$
\begin{aligned}
\langle 1 \rangle &= \frac{1}{U_0} \iiint_{U_f} 1 \, dU \\
&= \frac{U_f}{U_0} \\
&= \epsilon.
\end{aligned}
\tag{A.2}
$$

The intrinsic phase average of $\psi = 1$ yields:

$$
\begin{aligned}
\langle 1 \rangle_f &= \frac{1}{U_f} \iiint_{U_f} 1 \, dU \\
&= \frac{U_f}{U_f} \\
&= 1.
\end{aligned}
\tag{A.3}
$$

Using the definition of the phase average, equation (2.5) we obtain the following identity

$$
\begin{aligned}
\langle \psi + \lambda \rangle &= \frac{1}{U_0} \iiint_{U_f} (\psi + \lambda) \, dU \\
&= \frac{1}{U_0} \iiint_{U_f} \psi \, dU + \frac{1}{U_0} \iiint_{U_f} \lambda \, dU \\
&= \langle \psi \rangle + \langle \lambda \rangle.
\end{aligned}
\tag{A.4}
$$

If α is any constant, it may be removed from the averaging operator in case of the average of a product between α and a dependent variable

$$
\begin{aligned}
\langle \alpha \psi \rangle &= \frac{1}{U_0} \iiint_{U_f} \alpha \psi \, dU \\
&= \alpha \frac{1}{U_0} \iiint_{U_f} \psi \, dU \\
&= \alpha \langle \psi \rangle.
\end{aligned}
\tag{A.5}
$$

Applying the definition of the intrinsic phase average, we obtain

$$
\begin{aligned}
\langle \psi \rangle_f \langle \lambda \rangle_f + \langle \{\psi\}\{\lambda\} \rangle_f &= \frac{1}{U_f} \iiint_{U_f} \psi \, dU \frac{1}{U_f} \iiint_{U_f} \lambda \, dU + \frac{1}{U_f} \iiint_{U_f} \{\psi\}\{\lambda\} \, dU \\
&= \frac{1}{U_f} \iiint_{U_f} \psi \lambda \, dU \\
&= \langle \psi \lambda \rangle_f.
\end{aligned}
\tag{A.6}
$$

The following identity shows that the average of the deviation is zero

$$
\begin{aligned}
\langle\{\psi\}\rangle &= \frac{1}{U_0} \iiint_{U_f} \{\psi\}\, dU \\
&= \frac{1}{U_0} \iiint_{U_f} (\psi - \langle\psi\rangle_f)\, dU \\
&= 0.
\end{aligned}
\tag{A.7}
$$

A.2 Identities Based On The Averaging Theorem

Slattery's averaging theorem yields the following equation

$$
\nabla \iiint_{U_f} \psi\, dU = \iint_{S_{ff}} \underline{n}\psi\, dS.
\tag{A.8}
$$

The following theorem is derived using equation (A.8) and the divergence theorem. The divergence theorem as applied to U_f yields

$$
\begin{aligned}
\iiint_{U_f} \nabla\psi\, dU &= \iint_{\partial U_f} \underline{n}\psi\, dS \\
&= \iint_{S_{fs}} \underline{n}\psi\, dS + \iint_{S_{ff}} \underline{n}\psi\, dS
\end{aligned}
\tag{A.9}
$$

and

$$
\iint_{S_{ff}} \underline{n}\psi\, dS = \iiint_{U_f} \nabla\psi\, dU - \iint_{S_{fs}} \underline{n}\psi\, dS
\tag{A.10}
$$

Substituting equation (A.10) into equation (A.8), we obtain

$$
\nabla \iiint_{U_f} \psi\, dU = \iiint_{U_f} \nabla\psi\, dU - \iint_{S_{fs}} \underline{n}\psi\, dS
\tag{A.11}
$$

It then follows that

$$
\iiint_{U_f} \nabla\psi\, dU = \nabla \iiint_{U_f} \psi\, dU + \iint_{S_{fs}} \underline{n}\psi\, dS.
\tag{A.12}
$$

Taking the volume U_0 to be of constant magnitude and shape, we get

$$\frac{1}{U_0} \iiint_{U_f} \nabla \psi \, dU = \nabla \left(\frac{1}{U_0} \iiint_{U_f} \psi \, dU \right) + \frac{1}{U_0} \iint_{S_{fs}} \underline{n} \psi \, dS. \tag{A.13}$$

Using the phase average definition we obtain the following theorem

$$\langle \nabla \psi \rangle = \nabla \langle \psi \rangle + \frac{1}{U_0} \iint_{S_{fs}} \underline{n} \psi \, dS. \tag{A.14}$$

If we set $\psi = 1$ and use the results of equation (A.2), equation (A.14) yields

$$\nabla \epsilon = -\frac{1}{U_0} \iint_{S_{fs}} \underline{n} \, dS. \tag{A.15}$$

Using the identity in equation (A.1), equation (A.14) can be written as

$$\langle \nabla \psi \rangle = \nabla \left(\epsilon \langle \psi \rangle_f \right) + \frac{1}{U_0} \iint_{S_{fs}} \underline{n} \psi \, dS. \tag{A.16}$$

Applying the identity $\nabla \alpha \xi = (\nabla \alpha) \xi + \alpha (\nabla \xi)$ to the term $\nabla \left(\epsilon \langle \psi \rangle_f \right)$ in equation (A.16) together with equation (A.15), we obtain

$$
\begin{aligned}
\langle \nabla \psi \rangle &= \nabla \left(\epsilon \langle \psi \rangle_f \right) + \epsilon \nabla \langle \psi \rangle_f + \frac{1}{U_0} \iint_{S_{fs}} \underline{n} \psi \, dS \\
&= \langle \psi \rangle_f \left(-\frac{1}{U_0} \right) \iint_{S_{fs}} \underline{n} \, dS + \frac{1}{U_0} \iint_{S_{fs}} \underline{n} \psi \, dS + \epsilon \nabla \langle \psi \rangle_f \\
&= \frac{1}{U_0} \iint_{S_{fs}} \underline{n} (\psi - \langle \psi \rangle_f) \, dS + \epsilon \nabla \langle \psi \rangle_f \\
&= \epsilon \nabla \langle \psi \rangle_f + \frac{1}{U_0} \iint_{S_{fs}} \underline{n} \{\psi\} \, dS.
\end{aligned}
\tag{A.17}
$$

Since equation (A.14) is valid for any tensorial quantity ψ, it also yields the following

$$\langle \nabla \cdot \psi \rangle = \nabla \cdot \langle \psi \rangle + \frac{1}{U_0} \iint_{S_{fs}} \psi \cdot \underline{n} \, dS. \tag{A.18}$$

A.3   Volume Averaging Of Transport Equations

The following expression gives a relation between the superficial velocity $\underline{q}$ and the interstitial velocity $\underline{v}$

$$\underline{q} \equiv \langle \underline{v} \rangle = \epsilon \langle \underline{v} \rangle_f \tag{A.19}$$

The volumetric phase averaging of the continuity equation (2.1), yields

$$\langle \nabla \cdot \underline{v} \rangle = \nabla \cdot \langle \underline{v} \rangle + \frac{1}{U_0} \iint_{S_{fs}} \underline{n} \cdot \underline{v} \, dS = 0 \qquad \{\text{rule } A.18\} \tag{A.20}$$

Applying the no-slip condition to the above equation (Eq. (A.20)), yields:

$$
\begin{aligned}
\nabla \cdot \langle \underline{v} \rangle + 0 &= 0 \\
\nabla \cdot \underline{q} &= 0. \qquad \{\text{Eq. } A.19\}
\end{aligned}
\tag{A.21}
$$

The volumetric averaging of each term in the momentum transport equation (2.2) respectively, yields

$$
\begin{aligned}
\left\langle \rho \frac{\partial \underline{v}}{\partial t} \right\rangle &= \rho \left\langle \frac{\partial \underline{v}}{\partial t} \right\rangle \qquad \{\text{rule } A.5\} \\
&= \rho \frac{\partial}{\partial t} \langle \underline{v} \rangle \\
&= \rho \frac{\partial \underline{q}}{\partial t} \qquad \{\text{Eq. } A.19\}
\end{aligned}
\tag{A.22}
$$

$$
\begin{aligned}
\langle \nabla \cdot (\rho \underline{v}\underline{v}) \rangle &= \rho \langle \nabla \cdot \underline{v}\underline{v} \rangle & \{\text{rule } A.5\} \\
&= \rho \nabla \cdot \langle \underline{v}\underline{v} \rangle + \frac{\rho}{U_0} \iint_{S_{fs}} \underline{n} \cdot \underline{v}\underline{v} \, dS & \{\text{rule } A.18\} \\
&= \rho \nabla \cdot \langle \underline{v}\underline{v} \rangle & \{\text{rule } A.18\} \\
&= \rho \nabla \cdot \left\{ \frac{1}{\epsilon} \langle \underline{v} \rangle \langle \underline{v} \rangle + \epsilon \langle \{\underline{v}\}\{\underline{v}\} \rangle_f \right\} & \{\text{rule } A.1 \;\&\; A.6\} \\
&= \rho \nabla \cdot \left\{ \underline{q}\underline{q}/\epsilon + \epsilon \langle \{\underline{v}\}\{\underline{v}\} \rangle_f \right\} & \{\text{rule } A.1 \;\&\; \text{Eq. } A.19\}
\end{aligned}
\tag{A.23}
$$

$$
\begin{aligned}
\langle \rho \underline{g} \rangle &= \rho \langle \underline{g} \rangle && \{\text{rule } A.5\} \\
&= \frac{\rho}{U_0} \iiint_{U_f} \underline{g} \, dU && \{\text{Eq. } (2.5)\} \\
&= \rho \underline{g} \cdot \frac{U_f}{U_0} \\
&= \epsilon \rho \underline{g} && (A.24)
\end{aligned}
$$

$$
\begin{aligned}
\langle \nabla p \rangle &= \epsilon \nabla \langle p \rangle_f + \frac{1}{U_0} \iint_{S_{fs}} \underline{n} \{p\} \, dS && \{\text{rule } A.17\} \\
&= \epsilon \nabla p_f + \frac{1}{U_0} \iint_{S_{fs}} \underline{n} \{p\} \, dS && (A.25)
\end{aligned}
$$

$$
\begin{aligned}
\langle \mu \nabla^2 \underline{v} \rangle &= \mu \langle \nabla^2 \underline{v} \rangle && \{\text{rule } A.5\} \\
&= \mu \langle \nabla \cdot \nabla \underline{v} \rangle \\
&= \mu \nabla \cdot \langle \nabla \underline{v} \rangle + \frac{\mu}{U_0} \iint_{S_{fs}} \underline{n} \cdot \nabla \underline{v} \, dS && \{\text{rule } A.18\} \\
&= \mu \nabla \cdot \left\{ \nabla \langle \underline{v} \rangle + \frac{1}{U_0} \iint_{S_{fs}} \underline{n}\underline{v} \, dS \right\} + \frac{1}{U_0} \iint_{S_{fs}} \mu \underline{n} \cdot \nabla \underline{v} \, dS && \{\text{rule } A.14\} \\
&= \mu \nabla \cdot \{ \nabla \langle \underline{v} \rangle \} + \frac{1}{U_0} \iint_{S_{fs}} \mu \underline{n} \cdot \nabla \underline{v} \, dS && \{\text{rule } A.14\} \\
&= \mu \nabla \cdot \nabla \underline{q} + \frac{1}{U_0} \iint_{S_{fs}} \mu \underline{n} \cdot \nabla \underline{v} \, dS && \{\text{rule } A.19\} \\
&= \mu \nabla^2 \underline{q} + \frac{1}{U_0} \iint_{S_{fs}} \mu \underline{n} \cdot \nabla \underline{v} \, dS. && (A.26)
\end{aligned}
$$

Adding all the above volume averaged terms, we obtain the following volumetric phase averaged momentum transport equation,

$$
\rho \frac{\partial \underline{q}}{\partial t} + \rho \nabla \cdot (\underline{q}\underline{q} / \epsilon) - \epsilon \rho \underline{g} + \epsilon \nabla p_f - \nabla \cdot \langle \underline{\tau} \rangle + \rho \nabla \cdot \langle \{\underline{v}\}\{\underline{v}\} \rangle +
$$
$$
\frac{1}{U_0} \iint_{S_{fs}} \left(\underline{n}\{p\} - \underline{n} \cdot \underline{\tau} \right) ds = 0. \qquad (A.27)
$$

Appendix B

Dimensionless Groups

The dimensionless groups that are needed in this study are presented in this section. The velocity in the fully developed region between parallel plates, defined by Shah & London (1978) is written as

$$u(y) = -\frac{1}{2\mu}\frac{dp}{dx}\left[yH - y^2\right].$$
(B.1)

Differentiating $u(y)$ with respect to y, we obtain

$$\frac{du}{dy}\Big|_{y=H} = \frac{H}{2\mu}\frac{dp}{dx}.$$
(B.2)

The shear stress at the wall is given by,

$$\tau_w = \mu\frac{du}{dy} = \frac{H}{2}\frac{dp}{dx}.$$
(B.3)

The mean velocity is obtained from,

$$\begin{aligned}
u_m &= \frac{1}{H}\int_0^H u(y)dy \\
&= -\frac{H^2}{12\mu}\frac{dp}{dx}.
\end{aligned}$$
(B.4)

According to Shah & London (1978) the Reynolds number is defined as the ratio of flow momentum rate ("inertia force") to viscous force for a specified duct

geometry. The Reynolds number therefore can be defined as:

$$Re = \frac{\rho u_m D_H}{\mu} \tag{B.5}$$

where ρ is the fluid density, u_m is the mean velocity, μ is the fluid viscosity and D_H is the hydraulic diameter, defined as follows

$$D_H = \frac{4 \times area}{wetted \quad perimeter} = \frac{4A}{P}. \tag{B.6}$$

For parallel plates the hydraulic diameter is twice the separation of plates. In our case

$$D_H = 2H. \tag{B.7}$$

The Fanning friction factor is defined in Bird et al. (1960) as follows,

$$f = \frac{\tau_w}{\frac{1}{2}\rho u_m^2}. \tag{B.8}$$

Mass flow rate represented by w is the product of the cross-sectional area H, the density ρ and the mean velocity u_m,

$$w = H\rho u_m. \tag{B.9}$$

Substituting the mean velocity u_m from equation (B.4) into equation (B.9), we obtain,

$$w = -\frac{H^3 \rho}{12\mu}\frac{dp}{dx}. \tag{B.10}$$

Substituting the value of τ_w from equation (B.3) in equation (B.8) yields,

$$f = \frac{\frac{dp}{dx}\frac{H}{2}}{\frac{1}{2}\rho u_m^2}. \tag{B.11}$$

Inserting $\frac{dp}{dx}$ from equation (B.10) into equation (B.11), we get

$$f = -\left(\frac{H}{2}\right)\frac{12\mu w}{H^3\rho(\frac{1}{2}\rho u_m^2)}. \tag{B.12}$$

Substituting w from equation (B.9) in equation (B.12), f simplifies to,

$$f = -\frac{12\mu}{H\rho u_m}. \tag{B.13}$$

Inserting $H = \frac{D_H}{2}$ in equation (B.13) yields,

$$\begin{aligned} f &= \frac{12\mu}{\frac{D_H}{2}\rho u_m} \\ &= \frac{24\mu}{\rho u_m} \\ &= \frac{24}{Re} \end{aligned} \tag{B.14}$$

where Re is the Reynolds number. The hydrodynamic entrance length is defined in subsection 4.1.2 and its dimensionless form is expressed as

$$L_{hy}^+ = \frac{L_{hy}}{D_H Re}. \tag{B.15}$$

The axial distance in the flow direction for the hydrodynamic entrance region is defined as

$$x^+ = \frac{x}{D_H Re}. \tag{B.16}$$

The new definition of the hydrodynamic entrance length defined by Du Plessis & Collins (1992) is

$$L_c^+ = x_c^+ = \left[\frac{3.44}{f Re}\right]^2. \tag{B.17}$$

To obtain the Incremental Pressure Drop number we use equation (B.1) and (B.4). Thus follows

$$\left(\frac{u}{u_m}\right)^2 = \frac{36y^2}{H^2} - \frac{72y^3}{H^3} + \frac{36y^4}{H^4}. \tag{B.18}$$

From Shah & London (1978) the Momentum Flux Correlation Factor $K_d(x)$ is defined as

$$
\begin{aligned}
K_d(x) &= \frac{1}{A_c} \int_{A_c} \left(\frac{u}{u_m}\right)^2 dA_c \\
&= \frac{1}{H} \int_0^H \left(\frac{u}{u_m}\right)^2 dy \\
&= \frac{1}{H} \int_0^H \left(\frac{36y^2}{H^2} - \frac{72y^3}{H^3} + \frac{36y^4}{H^4}\right) dy \\
&= \frac{6}{5}.
\end{aligned}
\tag{B.19}
$$

From equation (B.18) it follows that

$$\left(\frac{u}{u_m}\right)^3 = \frac{216y^3}{H^3} - \frac{648y^4}{H^4} + \frac{648y^5}{H^5} - \frac{216y^6}{H^6}. \tag{B.20}$$

The Kinetic Energy Correlation Factor $K_e(x)$ is also defined by Shah and London (1978) as

$$
\begin{aligned}
K_e(x) &= \frac{1}{A_c} \int_{A_c} \left(\frac{u}{u_m}\right)^3 dA_c \\
&= \frac{1}{H} \int_0^H \left(\frac{u}{u_m}\right)^3 dy \\
&= \frac{1}{H} \int_0^H \left(\frac{216y^3}{H^3} - \frac{648y^4}{H^4} + \frac{648y^5}{H^5} - \frac{216y^6}{H^6}\right) dy \\
&= 1.543.
\end{aligned}
\tag{B.21}
$$

Thus the Incremental Pressure Drop Number $K(\infty)$ is as follows

$$
\begin{aligned}
K(\infty) &= \frac{2}{A_c} \int_{A_c} \left[\left(\frac{u}{u_m} \right)^3 - \left(\frac{u}{u_m} \right)^2 \right] dA_c \\
&= 2 \left[K_e(x) - K_d(x) \right] \\
&= 0.686.
\end{aligned}
\tag{B.22}
$$

Bibliography

Atkinson[6], B., Brocklebank, M. P., Card, C. C. H., & Smith, J. M. (1969). Low reynolds number developing flows. AIChE J., 15, 548–553.

Bear, J. & Bachmat, Y. (1991). Introduction to Modelling of Transport Phenomena in Porous Media. Kluwer Academic Publishers, Dordrecht.

Bear, J. & Buchlin, J. M. (1991). Modeling and Applications of Transport Phenomena in Porous Media, volume 5. Kluwer Academic Publishers, Dordrecht.

Bird, R. B., Stewart, W. E., & Lightfoot, E. N. (1960). Transport Phenomena. John Wiley and Sons, New York.

Chen[7], R. Y. (1973). Flow in the entrance region at low reynolds numbers. J. Fluids Eng., 153–158.

Churchill, S. W. & Usagi, R. (1972). A general expression for the correlation of rates of transfer and other phenomena. American Institute of Chemical Enginnering, 18(6).

Cloete, M. & Du Plessis, J. P. (2006). Hydrodynamic permeability prediction for flow through 2d arrays of rectangles. Chemical Engineering Science, 49(21), 623–632.

Darcy[1], H. P. G. (1856). Les Fontaines Publiques de la ville de Dijon. Dalmont, Paris.

Diedericks, G. (1999). Pore-Scale Modeling of Transport Phenomena in Homogeneous Porous Media. PhD thesis, Department of Applied Mathematics, University of Stellenbosch.

Du Plessis, J. P. (1992). High reynolds number flow through granular porous media. Mathematical Modeling in Water resources, 179–186.

Du Plessis, J. P. (1994). Analytical quantification of coefficients in the ergun equation for fluid friction in a packed bed. Transport in Porous Media, 16, 189–207.

Du Plessis, J. P. (2002). Modelling and industrial application of flow through two-

dimensional porous media. Master's thesis, Department of Applied Mathematics, University of Stellenbosch.

Du Plessis, J. P. & Collins, M. R. (1992). A new definition for laminar flow entrance lengths of straight ducts. N & O, 11–16.

Du Plessis, J. P. & der Westhuizen, J. V. (1993). Laminar crossflow through prismatic porous media. R & D, 9(2), 18–24.

Du Plessis, J. P. & Masliyah, J. H. (1988). Mathematical modeling of flow through consolidated isotropic porous media. Transport in Porous Media, 3, 145–161.

Du Plessis, J. P. & Masliyah, J. H. (1991). Flow through isotropic granular porous media. Transport in Porous Media, 6, 207–221.

Dullien, F. A. L. (1975). Single phase flow through porous media and pore structure. Chemical Engineering, 10(21), 1–34.

Firdaouss, M. & Du Plessis, J. P. (2004). On the prediction of darcy permeability in nonisotropic periodic two-dimensional porous media. Porous Media, 7(2), 119–131.

Fluent Inc. (2005). Introductory Fluent and Gambit Notes (FLUENT v6.2 ed.). Europe: Fluent Inc.

Forchheimer[3], P. (1937). Wasserbewegung durch boden. Zeitung Ver. Deutsch, Ing., 45.

Fortin, Y., Defo, M., Tremblay, C., & Gendron, G. (2004). A simulation tool for the optimization of lumber drying schedules. Drying Technology, 22(5), 963–983.

Hua, L., Bibeau, E., He, P., Gartshore, I., Salcudean, M., Bian, Z., & Chow, S. (2001). Modeling of airflow in wood kilns. Forest Products, 51(6), 74–81.

Kaviany, M. (1995). Principles of Heat Transfer in Porous Media (Second ed.). Springer-Verlag, New York.

Lloyd, C. A. (2003). Hydrodynamic permeability of staggered and non-staggered regular arrays of squares. Master's thesis, Department of Applied Mathematics, University of Stellenbosch.

Lloyd, C. A., Plessis, J. P. D., & Halvorsen, B. M. (2004). On closure modelling of volume averaged equations for flow through two-dimensional arrays of squares. In Rahman, M., Mendes, A., & Brebbia, C. A. (Eds.), Proceedings of the Fifth International Conference on Advances in Fluid Mechanics. Libson, Portugal.

Lundgren[8], T. S., Sparrow, E. M., & Starr, J. B. (1964). Pressure drop due to the entrance region in ducts of arbitrary cross section. J. Basic Eng., 620–626.

McComas[5], S. T. (1967). Hydrodynamic entrance lengths for ducts of arbitrary cross section. J. Basic Eng., 847–850.

Pang, S. (2004). Airflow reversals for kiln drying of softwood: Application of kiln-wide drying model and stress model. In Proceedings of the 14th International Drying Symposium (IDS 2004). Sao Paulo, Brasil.

Patankar, S. V. (1980). Numerical Heat Transfer and Fluid Flow. Taylor and Francis, USA.

Reynolds[2], O. (1883). An experimental investigation of the circumstances which determine whether the motion of water shall be direct or sinous, and of the law of resistance in parallel channels. Phil. Trans. roy. Soc., 174, 935–982.

Schlichting, H. (1968). Boundary Layer Theory (Sixth ed.). McGraw -Hill, New York.

Shah, R. K. & London, A. L. (1978). Laminar Flow Forced Convection in Ducts. Supp. 1 of Advances in Heat Transfer, London.

Slattery[4], J. C. (1967). Flow of viscoelastic fluids through porous media. American Institute of Chemical Engineering., 13(6), 1066–1071.

Smit, G. J. F., Plessis, J. P. D., & (Sr.), J. P. D. P. (2007). Modeling of airflow through a stack in a timber-drying kiln. Applied Mathematical Modelling, 31(2), 270–282.

Sun, Z. & Carrington, G. (1999). Effect of stack configuration on wood drying processes. In Proceedings of the 6th IUFRO International Wood Drying Conference, (pp. 89–98)., University of Stellenbosch, Matieland, South africa.

Ward-Smith, A. J. (1980). Internal Fluid Flow. Oxford University Press, New York.

White[8], F. M. (1994). Fluid Mechanics (Third ed.). McGraw -Hill, Inc.